On Ultrafast Time-Domain TeraHertz Spectroscopy in the Condensed Phase: Linear Spectroscopic Measurements of Hydrogen-Bond Dynamics of Astrochemical Ice Analogs and Nonlinear TeraHertz Kerr Effect Measurements of Vibrational Quantum Beats

Thesis by

Marco Alberto Allodi

In Partial Fulfillment of the Requirements

for the Degree of

Doctor of Philosophy

California Institute of Technology

Pasadena, California

2015

(Defended May 26, 2015)

To My Family

Acknowledgements

It is important for us as human beings to reflect from time to time and remember that no person succeeds in isolation. This is certainly true for me with regards to my graduate career. I did not do this work by myself and truly would not be able to report any of the discoveries contained in this thesis without the help of a great many people.

To begin, I'd like to thank the people in the Blake group who helped make this thesis possible. Geoff has been an outstanding advisor and mentor for me throughout this process, and I am thankful to have you as my advisor. I've learned a great deal of science, and I really appreciate that I was given the freedom to be independent. I think this helped my development by allowing me to take full ownership of a project, from the first mirror out of (or maybe more accurately *inside*) the laser, to being the corresponding author, wrangling a paper through the peer-review process. I appreciate your support of my work. It gave me added confidence when you thought things were moving in the right direction, and when I was frustrated or facing a set-back, I alway left your office feeling like anything was possible. In addition, you set an excellent standard of both personal and professional conduct that I hope I can at least partially emulate in my career. Your kindness and caring for your students makes me proud to be one of the *GA Blakers*.

Of course, my labmates contributed to my abilities as a scientist, to my projects, and my sanity. I'm thankful that I met such a great group of people, and I'm glad that we all wound up friends. With that said, they still deserve their own individual notes of appreciation. For simplicity of organization, I will thank everyone in chronological order of when we met.

Matt Kelley, thanks so much for teaching me about lasers and THz pulses. Without your mentorship at the start of my career, I wouldn't have had the laser building chops to execute the

projects I discuss in this thesis. I always enjoyed your company and our discussions. I hope you enjoy seeing in my thesis some of the fruits of your pioneering labor as a grad student.

Dan Holland, thanks for being willing to talk to a young student to help them figure out what was going on. I always enjoyed our conversations, and I'm glad that I learned something about imaging from all of it.

Brandon Carroll was part of the crew that joined the lab in the fall of 2011, and I'm very grateful that he joined. Thanks for all the great discussions about science and the science of beer. It's been a lot of fun working with you. I love your enthusiasm for building things, and thanks for helping me figure out what to do when something breaks.

Brett McGuire was the second member of the 2011 crew. Thanks for being my partner-in-crime on the ices experiment. I think we did a lot of good science together, and I enjoyed our various conference sojourns. Also, thanks for helping and inspiring me to be a better speaker. Talks are certainly an important part of communicating science and I'm thankful for your advice.

Ian Finneran, last but certainly not least of the 2011 crew, really helped make this thesis become what I wanted it to be. Thanks so much for joining me on the crazy nonlinear THz adventure. Your thoughts and insight were invaluable to me as we taught ourselves nonlinear spectroscopy. I always enjoyed all of our discussions and brainstorming sessions; it's been a lot of fun. I hope you can get all of our crazy ideas to work and I'm looking forward to reading your thesis.

Sergio Ioppolo joined the group as a postdoc in March of 2012. Thank you Sergio for acting as a day-to-day mentor and teaching me lots of things about what it takes to be a scientist. It's always good to remember to be patient and methodical, but you also pursued your research with an passion that was obvious to those around you, and that was important to see too. Also, thanks for letting us crash in your hotel rooms at conferences! You really enabled our group to become ice spectroscopy experts, and I'm glad I got to work with you, learn from you, and be a part of this process. Grazie mille!

Nate Crocket was the astronomer who became one of the “chemistry guys.” Thanks for being such a great resource for discussing data analysis and the chemistry of space. We’ve had a lot of fun together as well. Good luck in your new career as a data scientist.

Jacob Good was the latest free agent to sign with the Blakers. Thanks for your hard work getting ASOPS up and running and for showing me what was so great about Sharky’s. It’s been fun working with you.

I’d also like to thank the members of my PhD committee. I’ve enjoyed the scientific discussions that resulted at our committee meetings, and I hope you enjoy this thesis. Harry Gray has always been a great encourager of our science. Thanks for always taking the time to meet with me. I certainly learned a lot from our discussions, and I hope that our group will continue to work closely with yours. Tom Miller has always been helpful and friendly starting from my days as a prospective student. I’ve enjoyed working together on (summer) CPS and thanks for setting a good example of a junior faculty member for a young scientist to observe. Jack Beauchamp has been an excellent chair of this committee. Thanks for taking an extra moment time to talk to me when I passed by your office. I always learned something interesting from our discussions.

I’ve been assisted by a larger number of wonderful, and skilled people throughout Caltech. I appreciate all the hard work of our administrative staff - Agnes, Irma, Ulrika, and Margaret. Also, Mike and Steve in the machine shop and Rich the glassblower helped me make the instrumentation discussed herein. Thanks for all your help and hard work.

I would be remiss if I didn’t thank my friends during my time at Caltech. Josh, Tim and Jeff were my roommates throughout most of grad school, and Hal, Chris and Danien were there from the very beginning. I learned a lot of science from you guys. Thanks for helping me talk through a problem to get an outside perspective or just telling me about what was happening on the other side of the department. We made a lot of great memories exploring Southern California and Nevada. I’m thankful for the other people who I’ve become friends with along the way: Emma, Taylor, and Emily. Thanks for all the interesting conversations and support.

Since we are now moving in reverse-chronological order, I must thank Prof. Dr. Hans Bettermann for giving me my first experimental position and an academic home while I was a Fulbright student in Germany. It was a great year, and I learned much of the fundamentals of laser work in your laboratory that I still use to this day. I also learned some important things about Raman spectroscopy that have been key to the work discussed in this thesis. Thanks also to my labmates in the AK-Bettermann: Björn, Arno, Peter, Thomas, Shirin, Mario, and Katerina.

This thesis absolutely would not have been possible without the dedicated teaching and mentorship of the faculty of the chemistry and physics departments at Hamilton college. Thank you to Karen Brewer, Brian Collett, Gordon Jones, Robin Kinnel, and Ann Silversmith, because I certainly would not be here without your help. I owe two people from my Hamilton days particular mention. Karl Kirschner taught me the importance of taking risks in both science and life. Thank you for providing a good example of how to conduct yourself as a young scientist.

George Shields was my first scientific mentor and an outstanding teacher, and I consider myself incredibly fortunate to have worked with George for three years as an undergraduate at Hamilton College. Thank you, first and foremost, for constantly encouraging me to pursue a career in science. You taught me what scientists do and your passion for chemistry set a great example. It is impossible to underestimate the significance of a good mentor in choosing a career path. A PhD may not be for everybody, but it certainly was the right call for me. I'm thankful for your continued support and for the numerous things that you taught me. I would not be on the path I am today without your help.

I have been exceedingly fortunate to have two wonderful parents to gave their all to raise me. My dad was an outstanding supporter of my education because he had the immigrant's eye for how important education was for the success of an individual. He taught me the value of being intellectually curious and how important it was to get along with people. While I think sometimes he thought I was becoming the wrong type of doctor, I know that my work always made him proud. I would not have come this far in life without his love and support. My mom was my first teacher and she certainly deserves the most credit for turning me into an educated person. She inspired in

me a love of reading and education for which I'm ever-grateful. Thank you, mom, for your love and support, which has enabled me to approach the world with integrity.

Last, but absolutely not least, I must thank my wonderful wife, Katie. She's been a kind, patient, and understanding partner throughout graduate school. She has helped me to figure out how to navigate various challenges, as well as proofreading my papers and a large portion of this thesis!! Thank you for always being there for me. Your love and support enabled me to get through the challenging times in graduate school and helped remind me that there is much more to life than science. Thanks for locking your phase with mine. Here's to what we propagate through together!

Abstract

Much of the chemistry that affects life on planet Earth occurs in the condensed phase. The TeraHertz (THz) or far-infrared (far-IR) region of the electromagnetic spectrum (from 0.1 THz to 10 THz, 3 cm^{-1} to 300 cm^{-1}, or 3000 μm to 30 μm) has been shown to provide unique possibilities in the study of condensed-phase processes. The goal of this work is to expand the possibilities available in the THz region and undertake new investigations of fundamental interest to chemistry. Since we are fundamentally interested in condensed-phase processes, this thesis focuses on two areas where THz spectroscopy can provide new understanding: astrochemistry and solvation science.

To advance these fields, we had to develop new instrumentation that would enable the experiments necessary to answer new questions in either astrochemistry or solvation science. We first developed a new experimental setup capable of studying astrochemical ice analogs in both the TeraHertz (THz), or far-Infrared (far-IR), region (0.3 - 7.5 THz; 10 - 250 cm^{-1}) and the mid-IR (400 - 4000 cm^{-1}). The importance of astrochemical ices lies in their key role in the formation of complex organic molecules, such as amino acids and sugars in space. Thus, the instruments are capable of performing variety of spectroscopic studies that can provide especially relevant laboratory data to support astronomical observations from telescopes such as the Herschel Space Telescope, the Stratospheric Observatory for Infrared Astronomy (SOFIA), and the Atacama Large Millimeter Array (ALMA). The experimental apparatus uses a THz time-domain spectrometer, with a 1750/875 nm plasma source and a GaP detector crystal, to cover the bandwidth mentioned above with $\sim$10 GHz ($\sim$0.3 cm^{-1}) resolution.

Using the above instrumentation, experimental spectra of astrochemical ice analogs of water and carbon dioxide in pure, mixed, and layered ices were collected at different temperatures under high-

vacuum conditions with the goal of investigating the structure of the ice. We tentatively observe a new feature in both amorphous solid water and crystalline water at 33 cm^{-1} (1 THz). In addition, our studies of mixed and layered ices show how it is possible to identify the location of carbon dioxide as it segregates within the ice by observing its effect on the THz spectrum of water ice. The THz spectra of mixed and layered ices are further analyzed by fitting their spectra features to those of pure amorphous solid water and crystalline water ice to quantify the effects of temperature changes on structure. From the results of this work, it appears that THz spectroscopy is potentially well suited to study thermal transformations within the ice.

To advance the study of liquids with THz spectroscopy, we developed a new ultrafast nonlinear THz spectroscopic technique: heterodyne-detected, ultrafast THz Kerr effect (TKE) spectroscopy. We implemented a heterodyne-detection scheme into a TKE spectrometer that uses a stilbazoium-based THz emitter, 4-N,N-dimethylamino-4-N-methyl-stilbazolium 2,4,6-trimethylbenzenesulfonate (DSTMS), and high numerical aperture optics which generates THz electric field in excess of 300 kV/cm, in the sample. This allows us to report the first measurement of quantum beats at terahertz (THz) frequencies that result from vibrational coherences initiated by the nonlinear, dipolar interaction of a broadband, high-energy, (sub)picosecond THz pulse with the sample. Our instrument improves on both the frequency coverage, and sensitivity previously reported; it also ensures a backgroundless measurement of the THz Kerr effect in pure liquids. For liquid diiodomethane, we observe a quantum beat at 3.66 THz (122 cm^{-1}), in exact agreement with the fundamental transition frequency of the ν_4 vibration of the molecule. This result provides new insight into dipolar vs. Raman selection rules at terahertz frequencies.

To conclude we discuss future directions for the nonlinear THz spectroscopy in the Blake lab. We report the first results from an experiment using a plasma-based THz source for nonlinear spectroscopy that has the potential to enable nonlinear THz spectra with a sub-100 fs temporal resolution, and how the optics involved in the plasma mechanism can enable THz pulse shaping. Finally, we discuss how a single-shot THz detection scheme could improve the acquisition of THz data and how such a scheme could be implemented in the Blake lab. The instruments developed

herein will hopefully remain a part of the groups core competencies and serve as building blocks for the next generation of THz instrumentation that pushes the frontiers of both chemistry and the scientific enterprise as a whole.

Contents

List of Figures

List of Tables

Part I

Introduction

Chapter 1

Introduction

Much of the chemistry that affects life on planet Earth occurs in the condensed phase. Ubiquitous and important condensed-phase chemistry determines the outcome of everything from photosynthetic reactions in plants to laboratory reactions performed by organic chemists in search of new molecules. Indeed, research in the last few years has shown that condensed-phase processes in molecular ices likely govern the formation of complex molecules in space.[1] These molecules affect models of planet formation and pre-biotic chemistry, thus shaping our understanding of how life formed on this planet.[2] In addition, the interactions between the molecules of liquid water give rise to its unique properties and certainly affect its chemistry.[3]

Unsurprisingly, there exist a variety of spectroscopic tools that allow scientists to gain insight into the diverse set of interesting condensed-phase phenomena. These tools span the entire electromagnetic spectrum from the radio [4] up to the X-ray,[5] and each region offers unique insight. Different photon energies enable the investigation of different chemical properties; in addition, the intrinsic photon frequency and the bandwidth of the photon sources also set the timescale of interaction to be probed, or one could also say they determine the possible time resolution. As a result, the choice of spectroscopic region will depend upon the problem of interest.

The TeraHertz (THz) region of the electromagnetic spectrum provides unique possibilities in the study of condensed-phase processes. Spectroscopists define the THz region, also known as the far-IR, as the spectral region between 0.1 THz to 10 THz (3 cm^{-1} to 300 cm^{-1}, or 3000 μm to 30 μm).[6] What is especially important from a chemistry perspective is the nature of the interactions that can

be investigated in the THz region. As the older name for the THz, the far-IR, suggests, many of the features accessible in this regime correspond to resonances of vibrational character in the condensed phase. However, the THz region differs from the mid- and near-IR in that these vibrations are not predominantly intramolecular vibrations of individual chemical bonds, rather the resonances are long-range intermolecular vibrations, corresponding to the concerted motion of many adjacent molecules, or they are large-amplitude vibrational motions of whole parts of molecules. Both types of resonances are much lower in energy than the intramolecular bond vibration, and, consequently, one must use THz photons to investigate them.

Hydrogen bonding in solids provides one concrete example of intermolecular interactions at THz photon energies. The molecular ices that form on a dust grain in interstellar space can be either crystalline or amorphous solids.[7] In the case of crystalline water ice, there is a stretching motion between the crystalline bilayers, held together with hydrogen bonds, that has a resonance squarely in the middle of the THz region at $\sim$6.7 THz.[8] Since this feature is sensitive to long-range interactions in the ice, it is a good feature to observe if one is interested in changes to the large-scale structure of the ice.

In addition to the THz photon energies, the frequency of the light and bandwidth of photon sources at THz frequencies can be used to create pulses of THz photons short enough to study many dynamical problems in the condensed phase. If we consider the frequency 1 THz = $1\text{x}10^{12}$ Hz, the period of a sine wave at 1 THz would be $1/1\text{x}10^{12}$ Hz, which equals $1\text{x}10^{-12}$ s or 1 ps; the period of waves greater than 1 THz will be even shorter than 1 ps. Thus, the superposition of several octaves worth of frequencies in the THz region of the spectrum will create wave packets that are $\leq$ 1 ps in duration. Consequently, this offers sufficient time resolution to gain insight into molecular motions, such as intermolecular vibrations or librations in liquids.

The time resolution of THz pulses combined with the equivalent photon energies allow us to access a unique class of chemical problems in the THz region, namely the dynamics of liquids. We tend to think of liquids as a collection of molecules that interact with each other via Coulombic interactions. Given the weakness of these interactions relative to the strength of chemical bonds,

the standard description of liquids describes independent molecules, each with its own degrees of freedom. However, the strength of those interactions between liquid molecules on a (sub)ps timescale can determine the dynamics of other molecules in the liquid, and the model of "truly independent" molecules may not hold. For example, the hydrogen bonding properties of water modify the physical situation significantly. Water can form an extensive hydrogen-bonded network, where hydrogen bonds form and break on a fs to ps timescale. As such, a simple model of isolated molecules with harmonic or slightly anharmonic molecular vibrations describes liquid water poorly. Indeed, recent results suggest that the anharmonicity of the molecular vibrations is large enough that dipole selection rules for the harmonic oscillator may not be appropriate for these modes.[9; 10]. Since these are also hydrogen-bonded interactions, the THz region is the appropriate energy scale to study these interactions, and when coupled with the possible timing resolution, there are clearly many important questions that can be answered using THz science.

Many exciting possibilities remain for THz science to transform our understanding of the natural world because the technology allowing scientists to explore this region of the electromagnetic spectrum remains in its infancy. This is clearly not because of a lack of interesting problems. On the contrary, it results from the difficulties of generating and detecting THz photons. If we consider the THz region relative to the radio and microwave, THz frequencies are blindingly fast. Thus, it is challenging for the conventional electronics that work at longer wavelengths to generate high-power THz sources. On the other hand, coming down in frequency from the visible region of the spectrum, with frequencies roughly three orders of magnitude faster than the THz, developing THz photonic technology presents its own unique challenges. To create a solid-state device that emits THz photons requires such a narrow bandgap that the materials have to be cooled to liquid nitrogen temperatures to prevent thermal excitation from governing the device. As such, the most successful approaches to working with THz photons involve some type of down-conversion or wave-mixing process, but the efficiencies of these processes can be a few percent at best.

However, in the last 20 years, several significant advances have allowed THz science to grow exponentially, with thousands of people around the world using THz technology to advance science.

Given the various exciting possibilities provided by THz photons, scientists in many fields make creative use of THz spectroscopy to answer the compelling questions in fields as diverse as solid-state physics, electrical engineering, or remote sensing. However, *as a chemist, I chose to focus on two fields where THz spectroscopy is poised to make a significant impact:* ***astrochemistry and solvation science.***

Astrochemistry can be defined generally as studying molecules in space. Two important questions can be asked. First, how do we identify different molecules in space? Then we can ask how they form, and, by extension, if larger molecules can form from smaller ones. Identifying molecules in space requires laboratory experiments to measure the spectra of individual molecules, and then these spectra can be compared with astronomical observations to identify a given molecule. Understanding the formation of different molecules in space presents a more challenging problem, and a successful approach uses data from both lab experiments, and astronomical observations combined with data from astrochemical modelers, who take our current understanding of molecules in space and attempt to predict how more complex molecules can form.

In addition to being an interesting problem in its own right, understanding complex molecule formation in space has implications for life on Earth. The building blocks of life, such as simple amino acids and sugars, may have been delivered to Earth after production in space. Encouragingly, the simplest amino acid, glycine, was detected in the coma of a comet by the STARDUST mission, [11] yet recent work has shown that glycine cannot form in the gas phase in space.[12] As such, it must form on the icy surface of a dust grain. Dust comprises about 1%, by mass, of material in the Interstellar Medium (ISM), or the space between stars. When dust particles are cool enough, molecules can condense onto the surface to form an icy mantle, coating the grain. The molecules on the surface can react with other molecules as they condense, with the grain acting as a third body to take away energy that results from an exothermic chemical reaction. Given the importance of this mechanism, a more detailed picture of ice spectroscopy in the laboratory becomes necessary to understand the formation of complex molecules in the ISM.[13; 14] In this thesis, I measured the linear THz spectroscopy of laboratory molecular ices, and discuss how, by interpreting the THz

spectra, we can begin to understand how the structure of the ice can influence its reactivity and dynamics.

In liquids, the solvent can significantly alter the reactivity and dynamics of molecules. Analogous to our spectra of molecular ices, the THz region of the spectrum offers distinctly new opportunities to better understand solvation. In contrast with the astrochemical work, studying solvation requires us to take advantage of the sub-ps time resolution of pulsed THz spectroscopy, and also employ nonlinear THz measurements. An important question we can pose involves understanding whether or not solvents have a transient structure that changes on ultrafast timescales.

THz spectroscopic studies are necessary to expanding our knowledge of the room temperature dynamics of molecular liquids given the photon energy relative to k_BT. At 298 K, k_BT = 207 cm^{-1}; thus, most modes in the THz window of the spectrum are populated by thermal radiation. Consequently, these soft solvent modes directly determine the molecular dynamics of liquids at room temperature. In comparison, the OH stretch centered at $\sim$3500 cm^{-1} is only a spectator mode that reports indirectly on the molecular dynamics happening at THz frequencies. As a result, THz spectroscopic tools offer the most *direct* insight into room-temperature dynamics of liquids.

Nonlinear THz spectroscopy may offer several diverse avenues to understand both the nature and structure of modes in the THz frequency region. Given the importance of THz-frequency modes for the room-temperature dynamics of molecular systems, nonlinear THz techniques can provide information about various dynamical processes that cannot be accessed with a linear measurement. However, much work remains before nonlinear THz spectroscopy becomes a mature field that can provide detailed chemical information about a system under study. To really gain insight into the dynamics of the soft, THz-active modes of a liquid, we would like to be able to perturb these modes in a way analogous to 2D IR spectroscopy. This would allow us to generate a 2D THz spectrum of a material under study. This thesis makes progress on this problem by providing the first measurement of vibrational coherences in a molecular liquid initiated with THz pulses. The ability to create and detect coherences is a prerequisite for the further development of nonlinear THz spectroscopy into a 2D spectroscopic technique. This is an exciting prospect because measurements

of different dynamical properties of a system via some form of 2D THz spectroscopy will add greatly to our knowledge of these soft modes that participate in the molecular dynamics and thus advance chemistry as a science.

This thesis is composed of five parts. Following this chapter, part II will discuss the instrumentation developed to investigate the scientific questions posed above. It will also discuss the specifics of data analysis needed to understand both our linear and nonlinear THz spectra. Part III focuses on linear THz measurements of astrochemical ice analogs, and finally part IV discusses our developments in understanding the dynamics of liquids using nonlinear THz Kerr effect spectroscopy, and the first measurement of vibrational coherences as quantum beats initiated by the nonlinear interaction of a THz pulse with a molecular system. I conclude with a discussion of future directions for these projects in part V. For the interested reader, please note that both part III and part IV will contain a more detailed introduction relevant to the specific science discussed therein.

Part II

Instrumentation and Data Analysis Procedures

This section of the thesis describes the instrumentation I developed to perform THz time-domain spectroscopy with a Ti:Sapphire based ultrafast regenerative amplifier laser system. Chapter 2 discusses the THz TDS system used to measure the linear spectra of astrochemical ice analogs, while Chapter 3 focuses on the instrumentation for nonlinear THz and THz Kerr effect experiments. Finally, Chapter 4 will discuss in detail the procedures to properly analyze THz time-domain data.

Chapter 2

A time-domain THz spectrometer for linear spectroscopy of astrochemical ice analogs

The majority of this chapter is reproduced either from "The structure and dynamics of carbon dioxide and water containing ices investigated via THz and mid-IR spectroscopy," by M.A. Allodi, S. Ioppolo, M.J. Kelley, B.A. McGuire, and G.A. Blake, Physical Chemistry Chemical Physics 2014, 16, 3442-3455. — Reproduced by permission of the PCCP Owner Societies; or from "THz and mid-IR spectroscopy of interstellar ice analogs: methyl and carboxylic acid groups" by S. Ioppolo, M.A. Allodi, B.A. McGuire, and G.A., Blake Faraday Discussions 2014, 168, 461. — Reproduced by permission of the Royal Society of Chemistry

The new experimental setup used for spectroscopy of astrochemical ice analogs consists of a high vacuum chamber, a commercially available FTIR spectrometer to cover the mid-IR, and a THz time-domain spectrometer (TDS), constructed in-house, to cover the THz, or far-IR, region. The complete instrument can be seen in Figure 2.1. We will discuss each component in detail in the sections below.

2.1 Vacuum chamber and IR spectrometer

Studying astrochemically-relevant ice analogues requires high vacuum and low temperatures. To achieve these conditions, we employ a high vacuum chamber (Janis R. C.) that encloses the cold finger of a closed-cycle He cryostat (CTI Cryogenics) capable of cooling a 1", high-resistivity, intrinsic Si substrate (University Wafers) to ∼8 K. A heating element, and thermocouple connected to the cryostat allows for precise control of the substrate temperature between ∼8 K and 300 K. As seen in Figure 2.2, the vacuum chamber is pumped through a 1.5" diameter, flexible, stainless steel pipe connected to a turbomolecular pump (Turbo V 250 Varian inc.). The configuration allows for the facile vertical translation of the main vacuum chamber when necessary to align the spectrometers. A liquid nitrogen reservoir above the TMP can be filled for cryo-pumping. The room temperature base pressure in the vacuum chamber reaches ∼5 x 10^{-6} Torr, yet when the cryostat is operating, the pressure in the vacuum chamber reaches as low as ∼10^{-8} Torr.

Samples are prepared for deposition in a stainless-steel dosing line as seen at the bottom of Figure 2.2. The line implements a Pirani gauge (Lesker KJL275800) in the range of 10^{-4} to 1000 Torr, and an active capacitance transmitter (MKS Baratron) in the range between 0.01 to 1100 Torr. The latter allows for mass independent monitoring of the gas sample pressure in the line. An all-metal leak valve (Lesker) separates the chamber from the portion of the dosing line where samples enter or are mixed. A 1/8" diameter stainless steel pipe connects the leak valve to the vacuum chamber. The end of the pipe is capped with a metal mesh with a 38 μm hole size (McMaster-Carr 85385T117) to ensure a uniform ice deposition, and the end is positioned ∼1" away from the substrate.

To deposit a pure ice, vapor fills the evacuated dosing line to a fixed pressure. Then, the leak valve leading into the chamber is opened to allow for a slow deposition of ice onto the Si substrate. The leak valve is closed once the ice on the substrate reaches the desired thickness. To create a layered sample, the dosing line is evacuated and filled with another molecule to a fixed pressure and then deposited via the leak valve.

Sample mixtures are prepared by first filling the dosing line with a sample of one molecule and then closing the valve separating the gas mixture reservoir from the rest of the dosing line. The remaining molecules of the first sample are evacuated using a mechanical pump and the dosing line is refilled with the second molecule. After filling the dosing line with the second molecule, the valve closing the gas mixture reservoir is opened and the two gasses mix in the full volume of the dosing line. The mixture can then be deposited onto the substrate in the sample chamber by opening the leak valve. For the experiments discussed below, water vapor was prepared in the dosing line from a sample of deionized liquid H_2O, which was degassed by several freeze-pump-thaw cycles. Gaseous CO_2 was used as received from Air Liquide (99.99%).

Our spectrometer operates in two distinct regions of the electromagnetic spectrum. Therefore, two different sources of radiation are used, each entering the chamber along separate paths but at 45° angles to the substrate surface to allow for both beams to be incident on the same sample, as seen in Figure 2.1. High-resistivity, 3.5 mm thick, 2" diameter, intrinsic Si wafers (University Wafers) act as both windows along the THz path, and one of the two windows along the IR path. A 2" diameter Si wafer (Edmunds #68-532) serves as the second IR window.

Mid-IR spectra with a resolution of 1 cm^{-1} are collected with a Nicolet 6700 FTIR spectrometer using OMNIC software (version 7.4.127, Thermo Scientific). Running in external sample mode, light leaves the spectrometer through a 2" diameter KBr window and enters a box purged with N_2. A pair of spherical mirrors collimates the light out of the spectrometer, and then an off-axis parabolic mirror (OAPM, Edmund Optics) #6 (f = 4") focuses the mid-IR beam onto the sample with a spot size that is ∼3/4" in diameter. The beam is collected by OAPM #7 (f = 4"), and finally tightly focused by OAPM #8 (f = 2") onto the MCT detector. OAPMs collect the light transmitted by the

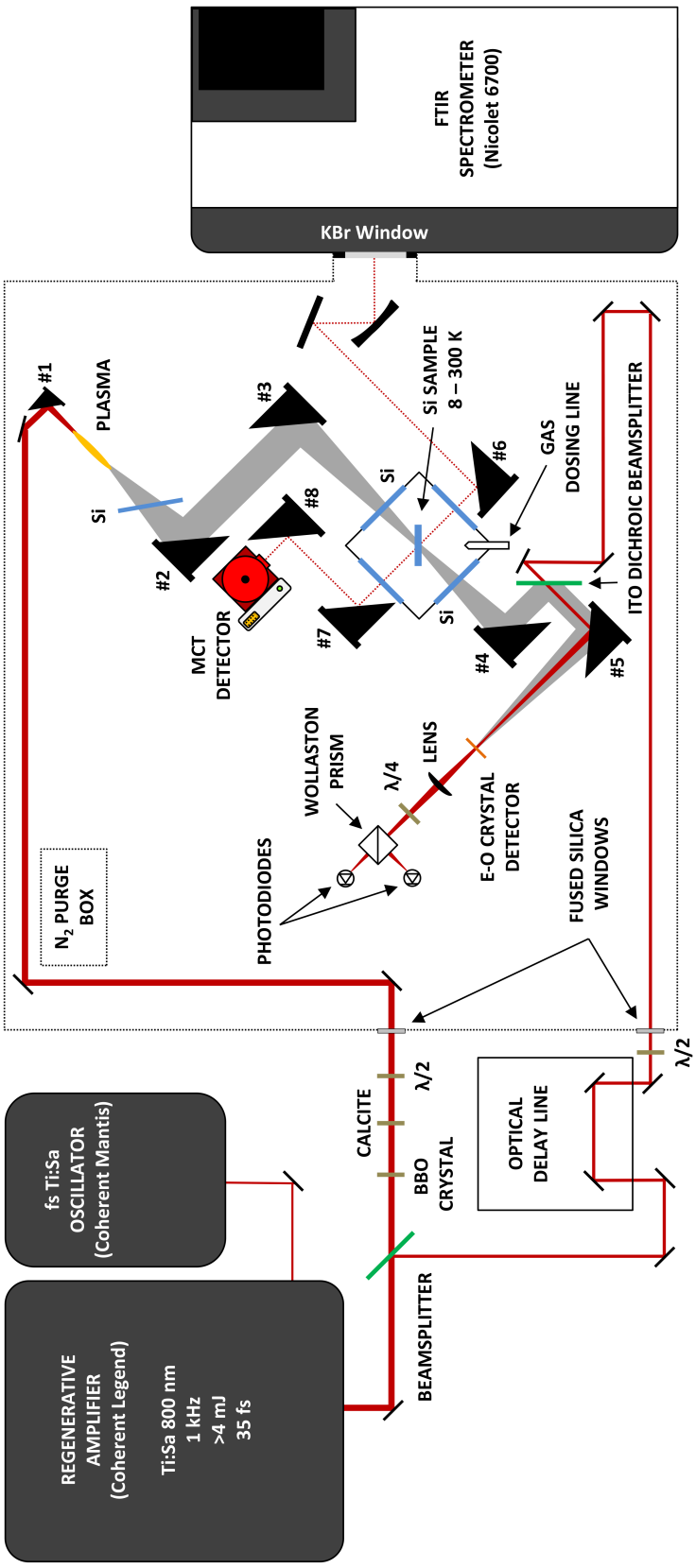

Figure 2.1: The layout of the Caltech astrochemical ice analog experimental setup, including the home-built time domain THz spectrometer. Not to scale. Taken from "The structure and dynamics of carbon dioxide and water containing ices investigated via THz and mid-IR spectroscopy," by M.A. Allodi, S. Ioppolo, M.J. Kelley, B.A. McGuire, and G.A. Blake, Physical Chemistry Chemical Physics 2014, 16, 3442-3455.

sample and steer the beam onto a mercury cadmium telluride (MCT) detector (Thermo Scientific 840-070300). All of the mid-IR spectra of ice samples shown below are averages of 512 co-added scans.

2.2 THz spectrometer

2.2.1 First THz source — 800 nm plasma

As seen in Figure 2.1, the first generation of the Caltech THz TDS relies upon an ultrafast laser system to generate and detect THz pulses. All of the data reported in the paper by Allodi et al. 2014[8] was collected using this THz TDS implementation. A Ti:Sapphire oscillator (Coherent Mantis) delivers sub 100 fs duration seed pulses containing 80 nm of bandwidth centered around 800 nm, to a chirped pulse regenerative amplifier (Coherent Legend Elite USP) at an 80 MHz repetition rate. The amplifier produces 4 mJ, 37 fs transform-limited pulses centered around 800 nm at a 1 kHz repetition rate. A 99% reflective dielectric mirror acts as a 99:1 beam splitter to divide the amplifier's output into a THz generation beam, and a THz detection beam.

The 99% split of the laser's output provides the spectrometer's THz light via a two-color plasma. The mirrors used to steer the generation beam before the beta-barium borate (BBO) are low dispersion, dielectric, high-reflecting mirrors (Newport 10B20UF.20). To make this plasma, a BBO crystal (Eksma Optics), cut for Type 1 second harmonic generation (SHG) at 800 nm, frequency doubles some of the 800 nm light to 400 nm. The 400 and 800 nm beams for generation enter the purge box full of N_2(g) via a dual-band AR coated 1" thick fused silica window (Eksma). A birefringent calcite plate (Eksma Optics) then corrects for the normal group velocity dispersion between 800 and 400 nm. Both colors pass through a zero-order dual-wavelength wave plate (Eksma Optics #465-4211) to align the polarizations of the 800 and 400 nm light. Finally, a gold coated, 1" diameter, 8" focal length (f) OAPM (Edmunds) labeled #1 in Fig 2.1 focuses both colors of light co-linearly, thus increasing the power per unit area of the light until it surpasses the breakdown point for N_2(g) molecules, thus producing a plasma.

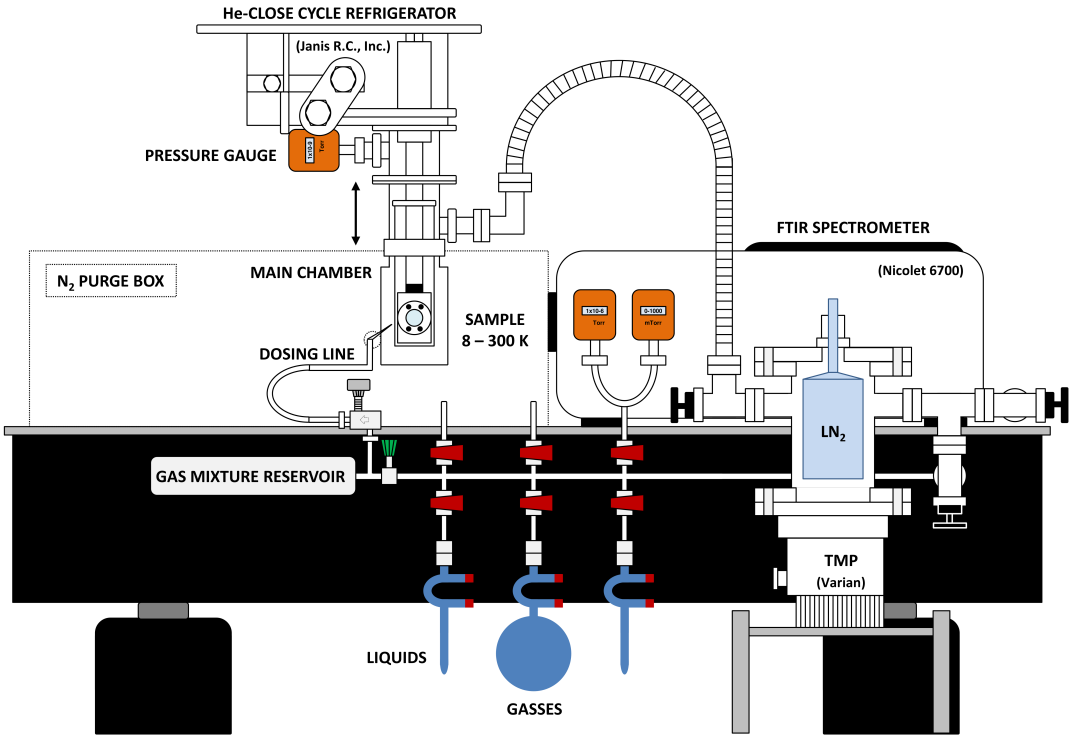

Figure 2.2: A side view of the experimental setup. The THz spectrometer is not shown here for purposes of clarity. Not to scale. Taken from "The structure and dynamics of carbon dioxide and water containing ices investigated via THz and mid-IR spectroscopy," by M.A. Allodi, S. Ioppolo, M.J. Kelley, B.A. McGuire, and G.A. Blake, Physical Chemistry Chemical Physics 2014, 16, 3442-3455.

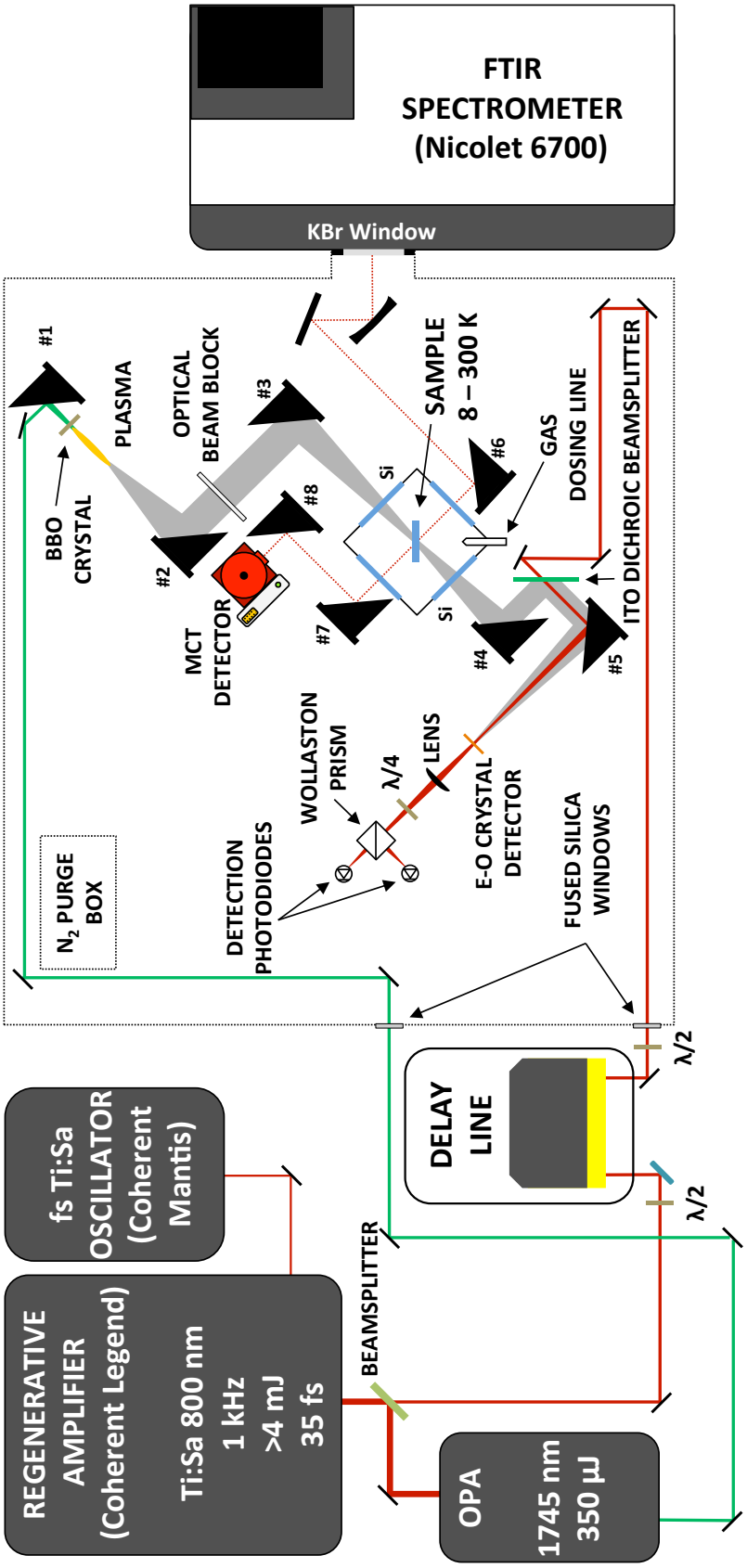

Figure 2.3: Schematic of the Caltech astronomical ice analog experimental setup, modified to show the inclusion of the OPA used for the 1745 nm plasma. Not to scale.

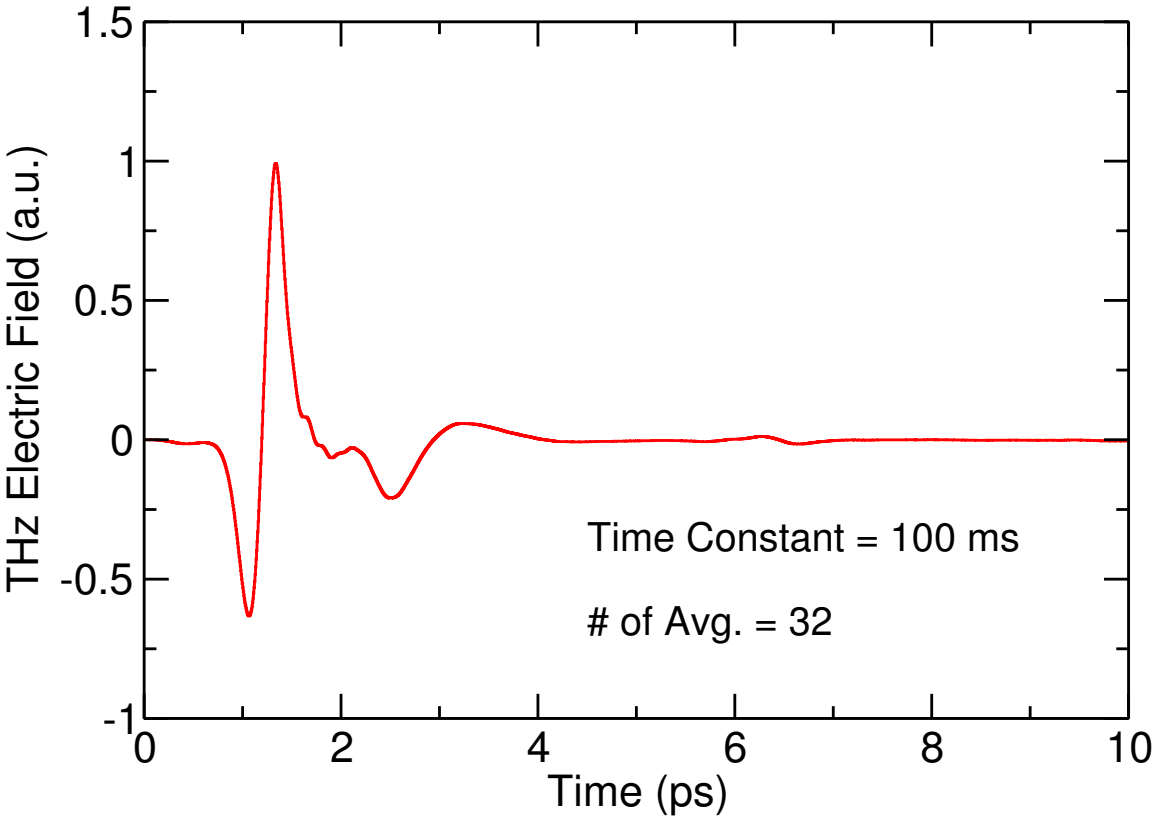

Figure 2.4: A THz trace of the blank substrate collected by the TD THz spectrometer. Taken from "The structure and dynamics of carbon dioxide and water containing ices investigated via THz and mid-IR spectroscopy," by M.A. Allodi, S. Ioppolo, M.J. Kelley, B.A. McGuire, and G.A. Blake, Physical Chemistry Chemical Physics 2014, 16, 3442-3455.

The combined 800 and 400 nm light fields can be thought of as symmetry-broken laser fields. The laser field can be written as:

$$E_L(t) = E_1\cos(\omega t + \phi) + E_2\cos[2(\omega t + \phi) + \theta], \tag{2.1}$$

where E_1 and E_2 are the amplitudes of the fundamental, and second harmonic respectively, and θ is the relative phase between the two harmonic fields. Once the intensity of the laser field is $> 10^{15}$ W cm^{-2} tunneling ionization of N_2 becomes possible, and for values of $\theta = \pi/2$, the symmetry-broken field produces an electron drift velocity, which produces a broad-bandwidth, intense THz pulse, with the same polarization as the optical light fields.[15; 16; 17; 18] OAPMs #2-4 are used to steer the THz beam, and focus the THz pulse down onto the ice sample in the vacuum chamber are 2" diameter protected gold mirrors with f = 6" (Edmunds Optics). To ensure a tight focus at the crystal, OAPM #5 has a 2" focal length. An optical chopper placed before the BBO crystal modulates the THz generation beam at 500 Hz for lock-in detection.

2.2.2 Second THz source — 1745 nm plasma

A diagram of the improved spectrometer for astrochemical ice analog spectroscopy can be seen in Figure 2.3. In the second implementation of a THz source for time-domain spectroscopy, the output of the ultrafast regenerative amplifier seeds an optical parametric amplifier (OPA) (Light Conversion inc.) capable of generating <40 fs pulses in the near-IR. Taking the idler output of the OPA at 1745 nm, and focusing that beam through a beta-barium borate (BBO) crystal creates a two-color plasma needed for THz pulse generation. This plasma generates THz pulses in a similar manner to the two-color plasma created with an 800 nm pulse and its second harmonic; however, the THz generation mechanism in plasma is more efficient at longer wavelengths.[19]

The issues associated with getting more THz pulse energy out of an 800/400 nm based plasma mainly result from saturation effects. Once enough laser power is used such that the material generating the plasma is completely ionized, other nonlinear processes can lead to quenching and

defocusing of the plasma. However, Clerici et al. have demonstrated that this limitation can be overcome by using longer wavelength photons to create the plasma.[19] In their models, they showed that the magnitude of the photocurrent in the plasma that emits the THz radiation scales with the wavelength (λ). They subsequently predicted that the THz energy radiated should scale as roughly λ^2. It turned out that the actual scaling for the experimental implementation is $\lambda^{4.6}$. This significantly improves the conversion efficiency from near-IR photons to THz photons. With a 800/400 nm plasma the conversion efficiency was limited to one part in 10^{-4} – 10^{-5}, but the efficiency from longer wavelength plasmas is now one part in $>10^{-3}$.

In the implementation in the Blake lab, previously, pulses with roughly 3.5 mJ of energy at 800 nm created a plasma to generate THz pulses. Now, pulses with roughly 300 μJ of energy at 1745 nm generate a plasma that produces THz pulses with a power comparable to the previous plasma at 800 nm. The wavelength of 1745 nm was chosen because it provided the largest peak THz electric fields for the current optical alignment of the spectrometer. As a technical note here, we achieved the best THz conversion efficiency with our BBO ∼1-1.5 cm from the plasma as discussed in Clerici et al. We also only had BBO cut for SHG at 800 nm. Thus, to achieve optimal phase matching, we angled the crystal to improve phase matching and thus THz pulse energy.

Finally, the OPA provides extra practical value to the lab. Parametric downconversion generates both a signal and an idler beam of comparable powers. As a result, we can use the same laser system to drive two experiments that have greater THz pulse energies as opposed to just one, or drive one experiment with two coherent THz sources. In addition, the availability of near-IR photons enables us to use organic crystal emitters (discussed in detail below) that have been shown to produce THz electric field strengths in excess of 10 MV/cm.[20] This will be a key technology that will enable the nonlinear THz experiments discussed later in this thesis.

2.2.3 Detection of THz pulses

2.2.3.1 Implementation of standard electo-optic sampling detection

We employ free-space, electro-optic sampling to detect the THz light transmitted through the ice sample. [21; 22; 23] Mirrors (Thorlabs PF10-03-P01) are used to route the remaining 1% of the 800 nm light from the original 4 mJ pulse down an opto-mechanical delay line (Newport ISL 150 with ESP300 controller) to change the relative delay between the THz generation and detection beams. Two beam samplers (Newport 10B20-01NC.2) are used in place of two mirrors along the detection path to attenuate the beam power, so as not to saturate the photodiodes. The detection beam then passes through a half-wave plate (Newport 10RP02-46), which can be rotated to ensure that the linear polarization of the detection beam and of THz beam are matched at the detector crystal for maximum signal. The 800 nm detection beam enters the purgebox via 800 nm AR coated 1" thick fused silica window (Eksma). An indium tin oxide (ITO) coated glass then serves to recombine the detection beam with the THz beam by reflecting the THz light and transmitting the 800 nm detection light so that the two beams co-axially propagate. An OAPM focuses the recombined beams onto a GaP (110) detector crystal (Incrys, 10 mm x 10 mm x 0.4 mm). The electric field of the THz light interacts with the crystal to produce a DC-bias, as the THz field is effectively DC when compared to optical frequencies. When 800 nm light co-propagates with THz light in the crystal, the THz electric field rotates the polarization of the 800 nm light via the Pockels effect. The magnitude of this change in polarization is proportional to the magnitude of the THz electric *field* applied. After passing through the detector crystal, a lens refocuses the 800 nm beam to ensure that the photodiodes detect all the light. It then propagates through a quarter-wave plate (Newport 10RP04-46) to create a circularly polarized beam that is split into orthogonal polarizations by a Wollaston Prism (Thorlabs WP20). The signal is measured as a difference signal generated by a pair of balanced photodiodes (Thorlabs PDA36A). When no THz light is incident on the GaP crystal, the photodiodes read the same voltage, but when THz light is present, the photodiodes are no longer balanced, and the resulting difference signal is proportional to the THz electric field.

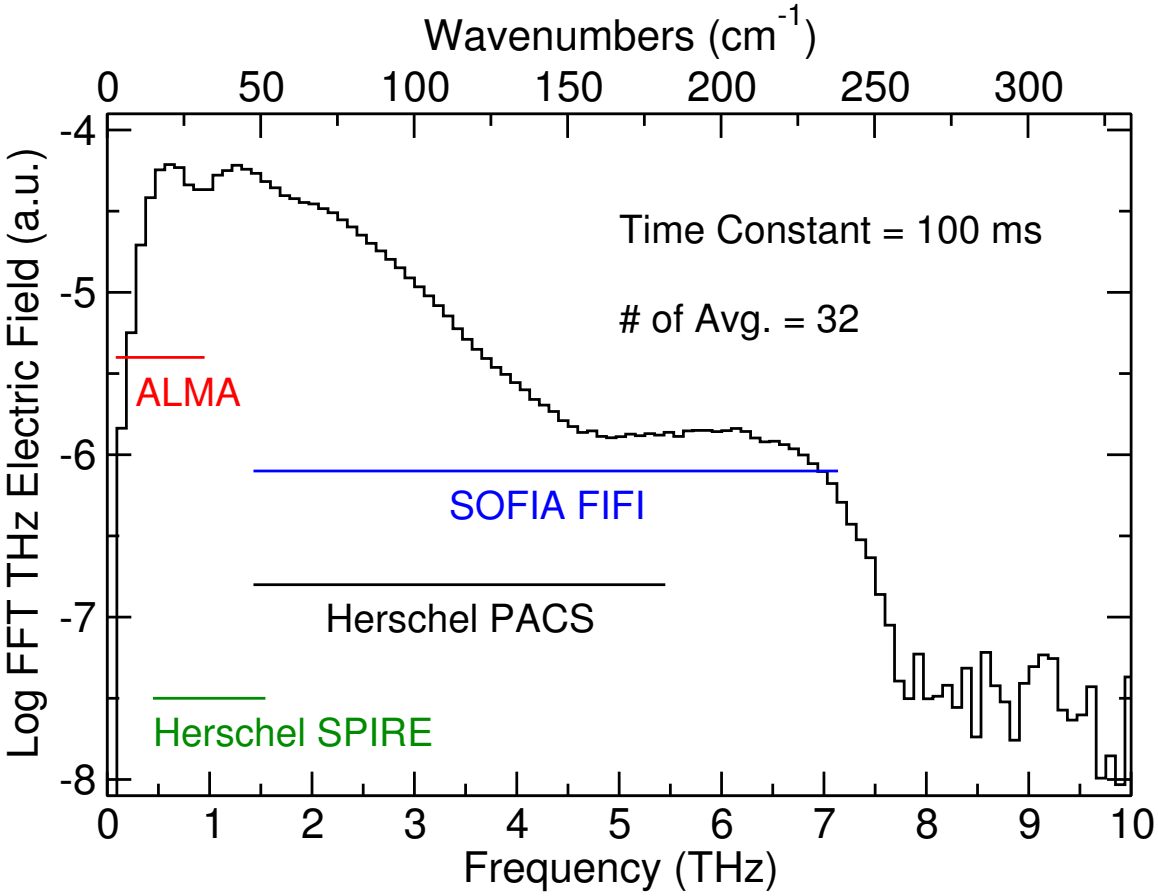

Figure 2.5: The bandwidth of the THz spectrometer. The ordinate provides information on the relative strength of the THz electric field within the THz pulse at different frequencies. The horizontal lines indicate the spectral coverage of observational facilities in the THz region. Taken from "The structure and dynamics of carbon dioxide and water containing ices investigated via THz and mid-IR spectroscopy," by M.A. Allodi, S. Ioppolo, M.J. Kelley, B.A. McGuire, and G.A. Blake, Physical Chemistry Chemical Physics 2014, 16, 3442-3455.

To measure the entire THz waveform in the time domain, the delay line moves to increase the detection path length so that the detection pulse interacts with the THz field at a different point in time. A digital lock-in amplifier (Stanford Research Systems SR830) records the spectrum as a function of delay. An example time domain trace collected with no sample on the substrate can be seen in Figure 2.4. The spectrum is an average of 32 co-added scans, with a 100 ms time constant on the lock-in amplifier. The analog output from the lock-in amplifier is digitized by a datacard (National Instruments USB-6361). Further details about the data collection can be found below in Chapter 3.

Using a plasma source and electro-optic (EO) sampling with a GaP detector crystal, the Caltech TD THz spectrometer detects a pulsed THz electric field with frequency content from 0.3 THz to 7.5 THz. The bandwidth can be seen in Figure 2.5, which is a numerical fast-Fourier transform (FFT) of the data in Figure 2.4, and the Figure also shows the overlap of our spectrometer with the capabilities of some of the aforementioned sub-millimeter and far-IR telescopes. In addition, Figure 2.5 shows the SNR in the frequency domain. By comparing the magnitude of signal on the ordinate to the noise level, which corresponds to the structure beyond 7.5 THz, one can roughly see how the SNR breaks down over the bandwidth of the spectrometer. In the 0.5 to 1.5 THz region, we report a SNR of 1800:1. From 1.5 to 4.5 THz, the SNR decreases by a factor of roughly 3 per 100 GHz starting at 1800:1 until it reaches 30:1, and the SNR remains flat at that value from 4.5 to 6.5 THz. The SNR then falls off again from 6.5 to 7.5 THz, where the signal meets the noise level.

The length of the scan in the time domain limits the resolution of the data in the frequency domain. While in theory only the length of the delay line limits the frequency-domain resolution, etalons produced in the EO detector crystal, and other optics through which the THz light passes, can add structure to the data. Small amounts of drift in the frequency position of the etalons over the course of an experimental run can be caused by environmental fluctuations and can change the etalon positions in the sample relative to the background scan. The etalons will then not divide out during background subtraction because of the time required to collect a spectrum. While there exist ways to push etalon peaks further away from the main THz pulse or remove them entirely, alternatively, one can scan a smaller window in the time domain to avoid these recurrences of the THz pulse. In this work, we co-added 32 spectra in the time domain to create an average which we subsequently used to calculate a FFT using boxcar apodization and zero-padding the length to the next power of 2. The spectra were collected over a 10 ps window in the time domain, chosen to avoid etalon features, which corresponds to a frequency domain resolution of 94 GHz (3 cm^{-1}). The sample spectra were then divided by a reference scan of the bare Si substrate to provide the absorption spectra shown in the following figures.

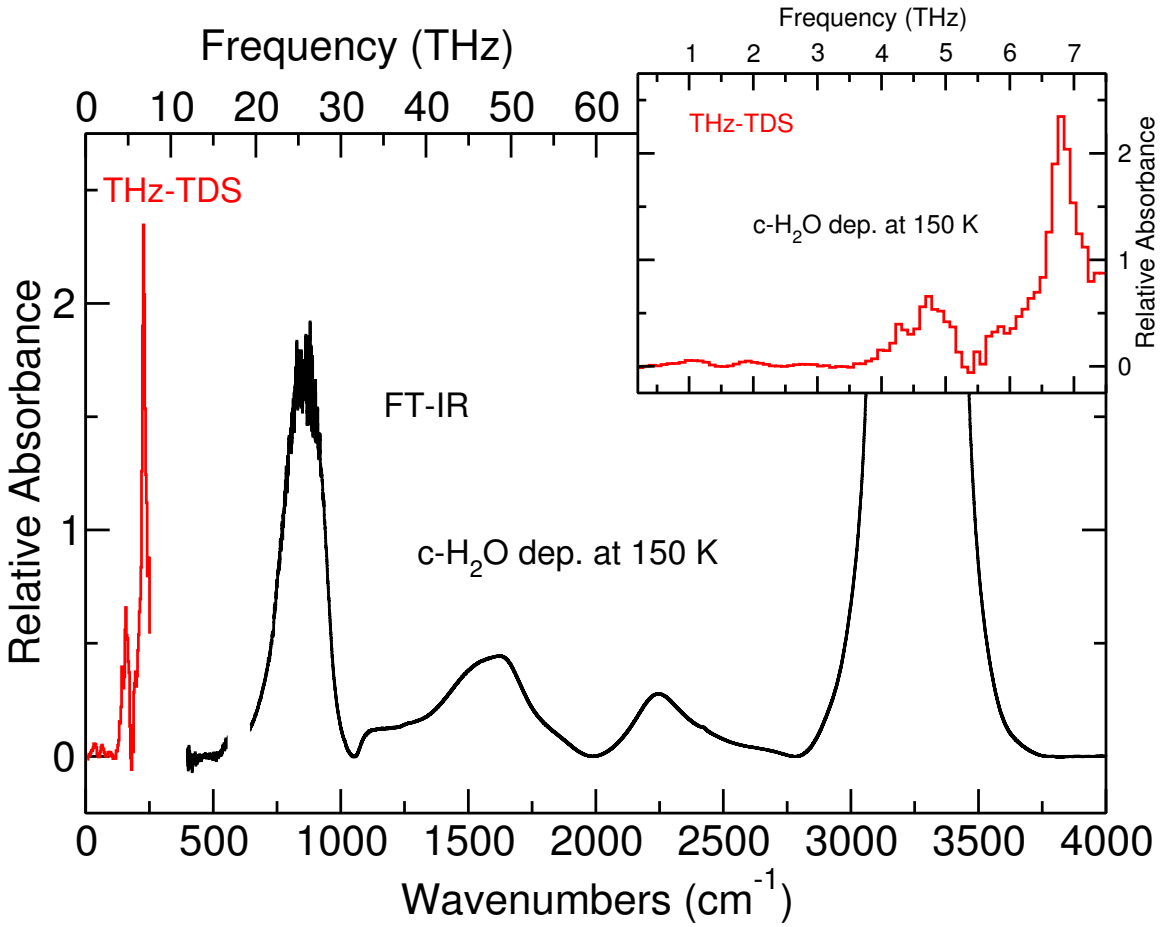

Figure 2.6: The spectrum of crystalline H_2O ice deposited at 150 K and collected at 150 K. This spectrum demonstrates the complete spectral window covered by the spectrometer. The inset shows a zoom of the region collected with the THz-TDS. Taken from "The structure and dynamics of carbon dioxide and water containing ices investigated via THz and mid-IR spectroscopy," by M.A. Allodi, S. Ioppolo, M.J. Kelley, B.A. McGuire, and G.A. Blake, Physical Chemistry Chemical Physics 2014, 16, 3442-3455.

The spectral coverage of the combined THz and FTIR capabilities can be seen in Figure 2.6. The spectrometer coverage extends from 10 - 4000 cm^{-1} with a gap from 250 - 400 cm^{-1} and a small gap between 580 - 630 cm^{-1} because the signal falls below the noise in those ranges. Using this broad spectral coverage, we are able to draw conclusions about the ices from both the THz and mid-IR regions.

2.2.3.2 THz detection enhancement

While we are able to achieve a sufficient signal-to-noise ratio to measure THz active modes in astrochemical ices, improving the sensitivity of the THz detection scheme would allow for the detection of weaker features in the ices or allow us to study more things by achieving a similar signal-to-noise ratio in less time. In addition, the implementation of this instrumentation is key to the detection of nonlinear THz signals as discussed in Chapter 3.

To improve the sensitivity of the linear THz measurement, we implemented an optical design developed recently in the literature.[24; 25] This detection scheme can be thought of as an analogous technique to the optical heterodyne detection used by every group the performs ultrafast optical Kerr effect spectroscopy. What this lets us do for linear spectroscopy is significantly lower the noise floor of our measurement. This is accomplished by the use of a polarizer and the Wollaston prism. This combination can be thought of as a pair of crossed polarizers. The first polarizer can be set to ensure that when there is no THz light on the detector crystal; all of the light is in the s-polarization. The Wollaston prism splits the beam into p- and s-polarizations that are measured on different photodiodes, and this results in a minimum p-signal in the absence of THz light. Then, THz light on the detector crystal induces a transient birefringence in the crystal. This birefringence rotates the polarization of the 800 nm light used in detection.

The measurement of the transient birefringence underlies all electro-optic sampling measurements of THz pulses. With the detection-enhancement scheme in place, the measured signal appears only as an increase in the measured signal on the p-polarization photodiode. The second photodiode acts only to improve the rejection of common-mode noise. In the previous setup it was necessary to look at the changes in both photodiodes to extract the THz signal. Thus, we can think of the detection scheme in the previous setup as measuring a small change in THz signal on top of a large background. The detection enhancement allows for the measurement of the THz signal more directly by minimizing the signal on the p-polarization photodiode in the absence of THz photons. As a result, the detection electronics can be optimized for the size of the small signal and not the signal plus background.

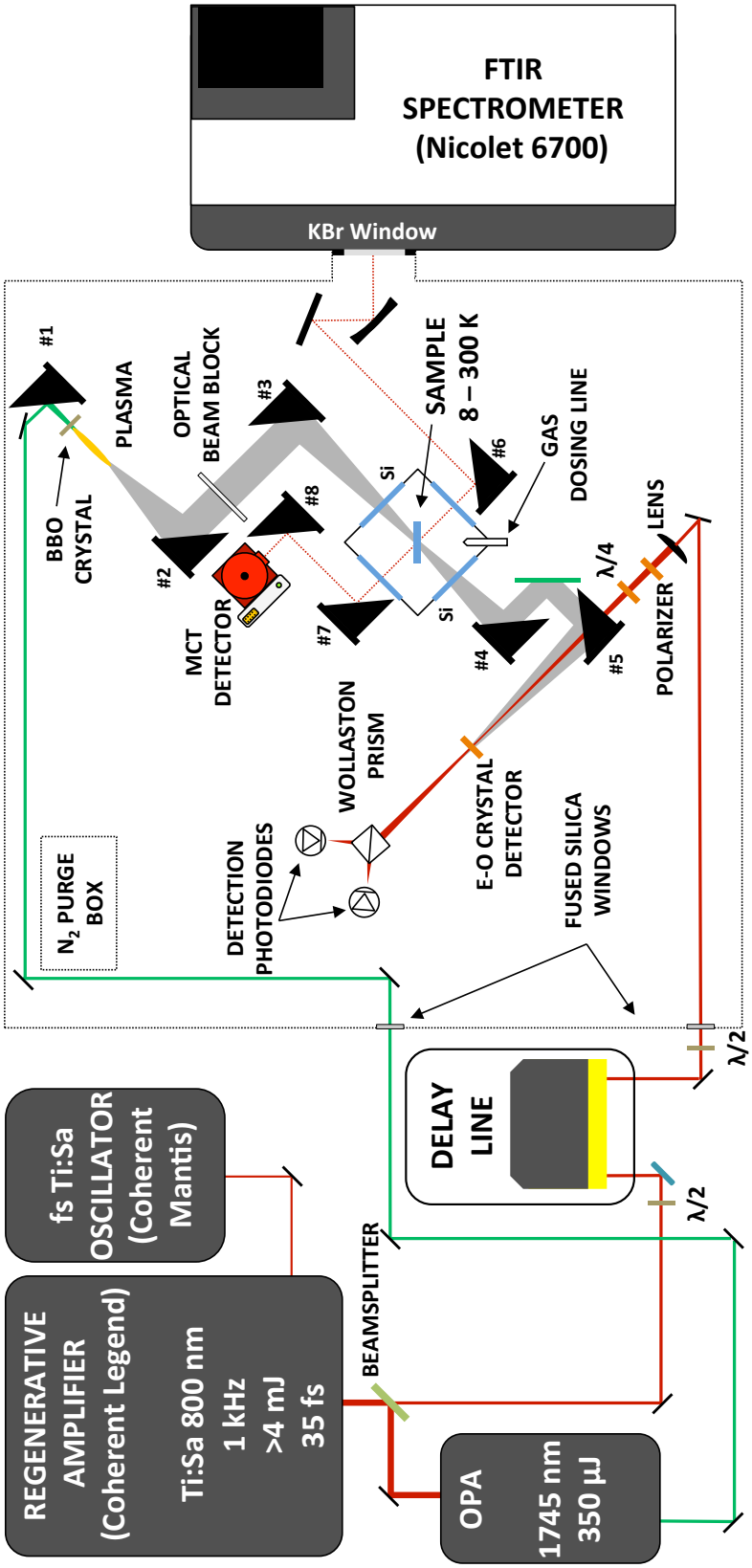

Figure 2.7: Schematic of the Caltech astronomical ice analog experimental setup in current operation. This includes a plasma generated with 1745 nm light and detection enhancement. Not to scale.

Chapter 3

Instrumentation for nonlinear TeraHertz experiments

Portions of this chapter are reproduced from "Vibrational Quantum Beats in Pure Molecular Liquids Measured with Ultrafast THz Kerr Effect Spectroscopy," by M.A. Allodi, I.A. Finneran, and G.A. Blake; Physical Review Letters, submitted.

Developing a nonlinear THz spectrometer presents its own specific challenges relative to the linear THz spectrometer described above. For signals as small as the nonlinear TKE signals, the instrumentation developed must have a large dynamic range, capable of detecting both the weak nonlinear signals as well as the large linear signals. Consequently, the choice of detection electronics is key. Second, for a nonlinear TKE measurement to work, we must be capable of generating a THz electric field in the sample that is in excess of 100 kV/cm. As such, the choice of an emitter and focusing optics will significantly affect the experiment. Finally, using an optical-heterodyne technique increases the signal-to-noise ratio and provides phase-sensitive detection. These points will be discussed at length below.

3.1 Improving data collection

When one compares the strength of any nonlinear signal compared to that of a linear signal, the need for improved experimental sensitivity becomes obvious. Fundamentally, the light-matter interaction can be written in the most general way as a wave equation with a source term:

$$\nabla^2 \vec{E}(t) - \frac{n^2}{c^2}\frac{\partial^2 \vec{E}(t)}{\partial t^2} = \frac{1}{\epsilon_0 c^2}\frac{\partial^2 \vec{P}(t)}{\partial t^2}, \tag{3.1}$$

where P is the material polarization. The polarization can be perturbatively expanded as

$$P(k,\omega) = \chi^{(1)}E(k,\omega) + \chi^{(2)}E(k_i,\omega_i)E(k_j,\omega_j) + \chi^{(3)}E(k_i,\omega_i)E(k_j,\omega_j)E(k_l,\omega_l) + \cdots, \tag{3.2}$$

where k_m and ω_m are the wavevector and the frequency of the mth component of the pulse respectively, and $\chi^{(n)}$ is the nth order optical susceptibility for the medium. Terms that are linear in E correspond to linear spectroscopy that can be described by Beer's law. Higher-order terms require multiple interactions with the electric field and are scaled by the optical susceptibility at that order. For example, if we consider a system in the condensed phase with a nonlinearity that

is electronic in nature, the second terms will begin to contribute to the expansion given in Eq. 3.2 when the applied electric field approaches the same order of magnitude of the atomic electric field, roughly $E_a = me^3/(4\pi\epsilon_o)^3\hbar^4 = 5\,\mathrm{x}\,10^{11}$ V/m. Thus $\chi^{(2)} \sim \chi^{(1)}/E_a$, yielding a value of $\chi^{(2)}$ of approximately $1\,\mathrm{x}\,10^{-12}$ m/V.[26] Given the weakness of the nonlinear signal, every effort must be taken to maximize the signal-to-noise ratio collected in a single laser shot if we wish to have instrumentation robust enough to study a variety of different chemical systems.

Our first fix to the spectrometer was to improve the timing axis of the data collected. The previous implementation of the THz spectrometer relied upon the internal clock in the computer to start acquiring data from the lock-in amplifier after sending a command to the delay line to begin moving. This led to appreciable jitter in the start time of scans, which is undesirable for several reasons. First, to acquire scans faster, the delay line must move faster. However, the jitter produced by the computer is constant whether the scan is fast or slow and thus the jitter as a fraction of total scan time is larger for a fast scan. The practical effect of the jitter is to cause the peak of the THz signal in the time domain to change position. Since it is preferable to average in the time domain, this jitter will lead to larger errors for a faster scan. As the peak shifts around in time, the measured bandwidth will decrease, resulting in an inaccurate measurement of the true time-domain waveform.

We accomplished this by directly counting encoder steps as the delay line was moving. The high-accuracy delay stage (Newport ISL 150) used is controlled by an ESP300 controller. Unfortunately, the ESP300 is not capable of providing a triggering pulse when it starts moving the delay stage. We note here that for the XPS controller available from Newport, the solution described next is not necessary because the XPS controller is capable of sending an external trigger signal. Since the ESP300 cannot trigger directly, we accessed the encoder information by measuring the encoder signal as it passes through the cable that connects the delay line to the controller.

The ESP300 controller produces reproducible motion of the delay stage by counting encoder pulses relative to its home position. Each rising edge of the encoder signal corresponds to a 400 nm step of the delay stage. The encoder pulses are generated using an LED, an optical mask, and small detector. As the stage moves along, the LED and detector move past the optical mask that has

identically-spaced openings that transmit the light from the LED, and this on vs. off signal is sent to the controller. The cable that connects the delay line and the encoder has a 24 pin connector on either side. The encoder signal is sent through the wire on pin 6. To access that signal, we send the cable from the delay line to a break-out box. Inside the box, we split the signal on pin 6. One wire is run to an output that is sent straight into the data card (National Instruments USB-6361). The second signal is sent along with the signals on all other pins into a cable that runs into the ESP300. By measuring the encoder pulses on the data card, the jitter in the previous measurement is obvious. The data card starts collecting before the delay line starts running, and each trace has a different number of data points at the start of the scan before the encoder signal shows the delay line moving. We are thus able to correct for the jitter by forcing all THz time-domain traces to start at the same encoder value.

The use of the data card to fix the timing jitter also addressed our issues relating to the rate at which we digitized the data coming from the spectrometer. This issue stems from our use of an SRS 830 digital lock-in amplifier. There are several options for getting data off this lock-in. A small dataset can be stored in internal memory and then transferred via GPIB or serial after acquisition. This option significantly decreases the duty cycle of data collection because the buffer must be read-out after each sweep of the delay line, thus making fast scanning impossible. Second, digitized data can be live-streamed over the GPIB connection, but the fastest the data are pushed over GPIB is 512 Hz. With this as a speed limit, syncing the rate of data collection to our 1 kHz laser is impossible. However, the lock-in also offers analog output ports that are continuously updated. By running a cable from this port into our data card, we can then digitize that signal with our data card. The data card is connected to a computer over USB 2.0, which yields millisecond data transfer times for files of this size. We thus achieve rapid scan acquisition and a sync of the measured signal to the position on the delay line.

3.2 High-power THz sources and optical design

Clearly, intense THz pulses would be needed to generate nonlinear spectra at these frequencies since larger THz electric fields lead to larger polarizations and thus larger signals. While THz pulses are now widely used by groups around the world, the table-top sources commonly employed, such as photo-conductive antennas or optical rectification (OR) in crystals, produce modest-field-strength pulses that generally span the 0.1-50 kV/cm range. Recently, THz pulse sources have been developed that herald the availability of field strengths in excess of 1-10 MV/cm at the foci of THz lenses or mirrors and pulse energies of > 1 μJ – stilbazoium-based THz emitters such as 4-N,N-dimethylamino-4-N-methyl-stilbazolium 2,4,6-trimethylbenzenesulfonate (DSTMS), and plasma filamentation. DSTMS and other crystals pumped near 1400 nm have proven to be highly capable, with focused field strengths approaching 50 MV/cm[27] and bandwidths of 2-6 THz. Conversion efficiencies can exceed Manely-Rowe limits since the process is not tied to direct photon conversion.

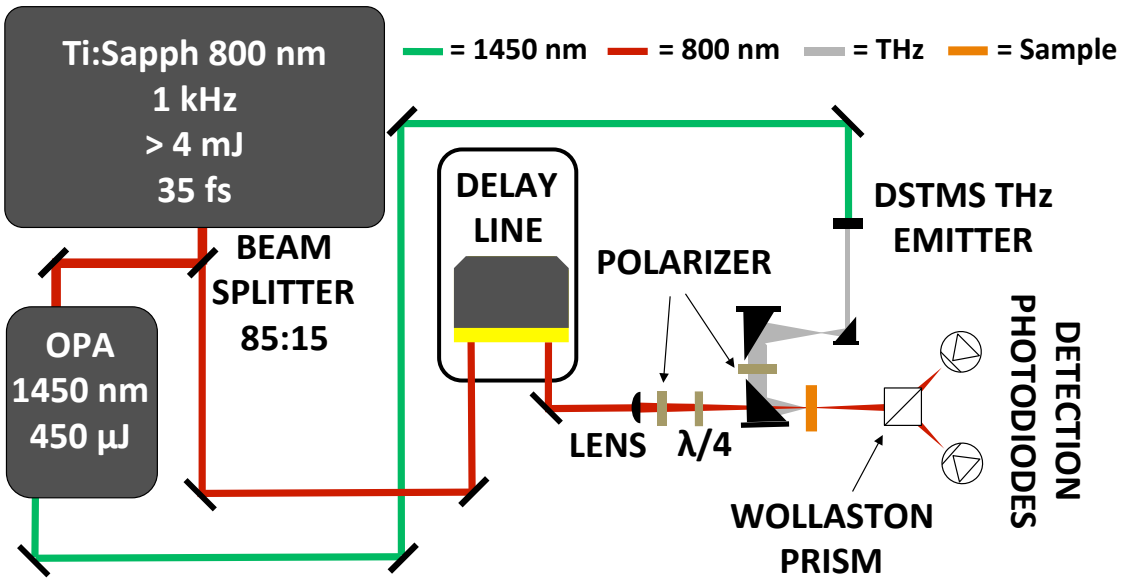

Figure 3.1: The experimental setup for TKE spectroscopy. Reproduced from Allodi et al. "Vibrational Quantum Beats in Pure Liquids Measured with Ultrafast TeraHertz Kerr Effect Spectroscopy" *Physical Review Letters, submitted.*

The experimental apparatus is shown in Fig. 3.1. Much of the instrumentation has been discussed in greater detail in the previous chapters in this section. This section serves to outline the changes

necessary to generate nonlinear THz spectra. The output of a Ti:Sapphire ultrafast laser amplifier running at a 1 kHz repetition rate (Coherent inc., Legend Elite), ∼4 mJ, 35 fs pulses centered at 800 nm, is split such that 85% of the power seeds an optical parametric amplifier (Light Conversion inc., TOPAS), and with the remainder going to an 800 nm probe beam. Approximately 400 mW of 1450 nm light passes through a DSTMS crystal (Rainbow Photonics) set on a 3 mm diameter aperture, producing ∼120 nJ THz pulses for the THz source of the TKE measurements. The remaining 1450 nm light is blocked by a piece of blackened TOPAS polymer, acting as a low-pass filter. The pseudo-collimated THz light from the DSTMS is imaged through a Gaussian-beam telescope, composed of two off-axis parabolic mirrors (OAPMs), to magnify the beam waist by a factor of 7.5. It should be noted here that previous attempts at building a TKE spectrometer in our lab did not include a Gaussian-beam telescope to increase the waist of the beam being focused. Since the TKE signal scales with beamwaist squared, magnifying the beam by a factor of 7.5 increases the magnitude of the TKE signal by a factor of 56. As a result, we were unable to measure HD-TKE signals until we included the Gaussian-beam telescope to magnify the beam; *the large numerical aperture is key to measuring nonlinear THz signals.* The collimated THz beam is passed through as wire-grid polarizer set at 45° relative to the polarization of the 800 nm probe beam, and then focused onto the sample using a 2" focal length OAPM. The THz beam is generated and detected in an environment purged with nitrogen gas.

The 800 nm light that was split off before the OPA is sent down an opto-mechanical delay line fitted with a retroreflector for precise control of the arrival time of the probe relative to the THz pulse at the sample. A combination of attenuating beam splitter and iris are used to reduce the power of the 800 nm beam to ∼2 mW. It passes through a $\lambda/2$ plate to control the polarization of the beam relative to the THz polarization. The beam then passes through an 8" focal length achromatic doublet lens (Thorlabs), a 10^5:1 polarizer (Throlabs LPVIS050-MP2), and a $\lambda/4$ plate needed for a heterodyne detection scheme. The focusing beam passes through a small hole drilled in the back of the 2" OAPM that focuses the THz beam and hits the sample. The 45° alignment of the polarizations of the THz and 800 nm beams ensures that we probe the transient birefringence

generated by the THz Kerr effect. The THz field strength at the sample focus is ∼300 kV/cm. The sample sits in a 1 mm path length z-cut quartz cuvette. After passing through the sample, the orthogonal polarizations of the beam are split by a Wollaston prism and detected on a pair of photodiodes. The polarizer combined with the Wollaston prism allow for the implementation of the heterodyne-detection scheme. The 10^5:1 polarizer before the sample can be adjusted such that almost all the light is in the s-polarization. The small fraction of light that is p-polarized acts as a 90° out-of-phase local oscillator that will be heterodyned with the molecular Kerr effect signal on the photodiode. This scheme ensures that only the backgroundless birefringence signal is measured.[28; 29] An iris in front of the photodiode is used to attenuate the s-polarized beam so that it is of a comparable magnitude to the p-polarized.[24; 25] The 1450 nm beam is modulated with an optical chopper at 500 Hz and photodiode signals are sent to a digital lock-in amplifier where the raw photodiode are amplified and subtracted. The analog output of the lock-in is sent to a data card (National Instruments USB-6361), where the TKE signal is digitized and recorded.

Similar THz fields with extraordinary bandwidths are now possible via the technique of plasma filamentation discussed above. Indeed, THz field strengths in excess of 4 MV/cm have been reported using a similar experimental plasma setup to the one discussed in Section 2.2.2.[19] Clearly, the THz field strengths generated with a plasma pulse can more than meet the threshold needed for nonlinear THz work. A plasma pulse generated with this setup in our laboratory can be seen in Figure 3.2. The advantage over DSTMS then becomes the broad bandwidth that a plasma pulse provides. As Figure 3.2 clearly shows, the full-width at half-maximum (FWHM) of the plasma THz pulse is roughly 215 fs. This is likely not a fully accurate representation of our THz pulse since we are limited by the detection bandwidth of GaP, and air-biased-coherent-detection setups [30] have measured the frequency content of these plasmas out past 20 THz.[19] This frequency coverage will enable nonlinear THz measurements over the entire THz window and will be also the key to sub-100 fs time resolution in nonlinear THz spectroscopy.

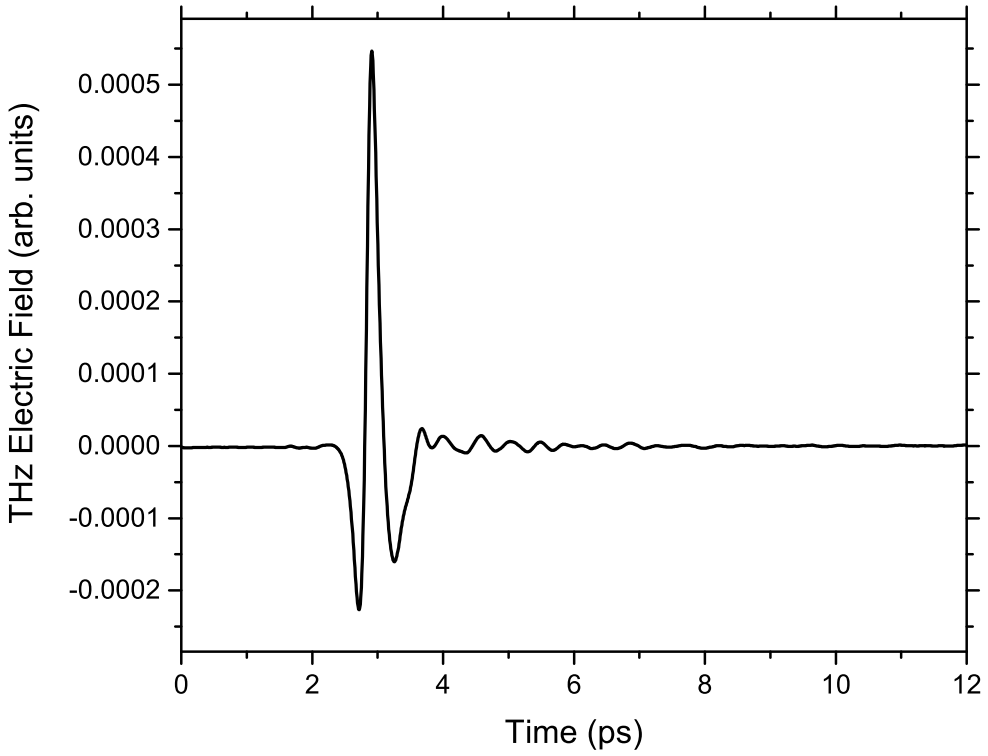

Figure 3.2: A THz time-domain trace trace of a THz pulse generated with a 1.75 μm plasma source and detected in GaP.

3.3 Heterodyne detection

The implementation of a heterodyne detection for TKE spectroscopy represents a significant advance in instrumentation. To understand why, we consider the heterodyne-detected signal $S_{het}(t)$,

$$S_{het}(t) = \int_{-\infty}^{\infty} dt\, E^{*}_{LO}(t) E^{(3)}_{Sig}(t), \tag{3.3}$$

where $E^{*}_{LO}(t)$ is the heterodyning 800 nm field, and $E^{(3)}_{Sig}(t)$ is the third-order molecular signal of interest.

The value of heterodyne detection becomes obvious when we consider the homodyne-detected signal

$$S_{homo}(t) = \int_{-\infty}^{\infty} dt\, E^{(3)*}_{Sig}(t) E^{(3)}_{Sig}(t). \tag{3.4}$$

When using a local oscillator to heterodyne with the molecular signal, the magnitude of the local-oscillator electric field can be increased to facilitate the measurement of a signal. In contrast, a homodyne measurement is limited to the strength of the signal field itself. As such, weak homodyne signals can fall below the detection threshold for a given experimental setup, but weak signals can be compensated for with the strength of the local-oscillator electric field.

In addition, the heterodyne-detected signal $S_{het}(t)$ scales linearly in both local-oscillator electric field as well as in molecular signal electric field. This allows for the detection of the phase of the emitted signal field. Having the phase of the signal field allows one to extract more information about the molecular response that would otherwise be possible. The significance of this will become clear in Chapter IV.

Chapter 4

Data analysis procedures

Portions of this chapter are reproduced from "THz and mid-IR spectroscopy of interstellar ice analogs: methyl and carboxylic acid groups" by S. Ioppolo, M.A. Allodi, B.A. McGuire, and G.A. Blake; Faraday Discussions 2014, 168, 461. — Reproduced by permission of The Royal Society of Chemistry

4.1 Analysis of Linear THz Data

Absorption spectra of the samples studied in the frequency domain are found by taking a fast Fourier transform (FFT) of the time domain data and dividing by a reference scan of the bare Si substrate. The resolution of the spectra collected is approximately equal to the inverse of the length of scan in the time domain. For these experiments, this yields a ∼90 GHz resolution in the frequency domain. With the optically contacted GaP crystal described in the section above, it is possible to increase the resolution of these spectra on our instrument to ∼10 GHz by scanning a larger window in the time domain. However, this time window was chosen so as to quickly collect high signal-to-noise spectra of many different ices. The following data analysis procedure allows us to extract the maximum information from the collected data.

Apodization is a necessary element of the data analysis to prevent spectral leakage. When Fourier transforming a time-domain signal collected in a window of finite duration, a boxcar function becomes convolved with the true time domain signal, resulting in each line in the frequency domain being convolved with a sinc function.[31] Spectral leakage arises because a sinc function will add many sidelobes to the main peak so distinguishing between separate peaks becomes more difficult. Choosing a different apodization function from the boxcar will suppress the sidelobes and prevent spectral leakage that would arise from the sidelobes of one feature overlapping with the peak of another nearby feature. However, there is a balance to be struck between suppressing the sidelobes, but not distorting the lineshape drastically. In addition, asymmetric apodization functions must be used given the asymmetric nature of the THz signal in the collection window.[32] All the data in this paper are processed using an asymmetric Hann window peaked at the maximum of the THz signal. The Hann window[33] provides a good balance between sidelobe suppression and lineshape concerns. The asymmetric Hann window used to apodize linear THz data can be seen in Figure 4.1.

After apodization, zeros were added to the apodized data to both interpolate between points in the frequency domain and ensure that the length of the data set equals a power of two. Zero padding in the time domain before taking an FFT is mathematically identical to interpolation in the frequency domain.[34] Interpolation can help to identify the center of a feature with high accuracy.

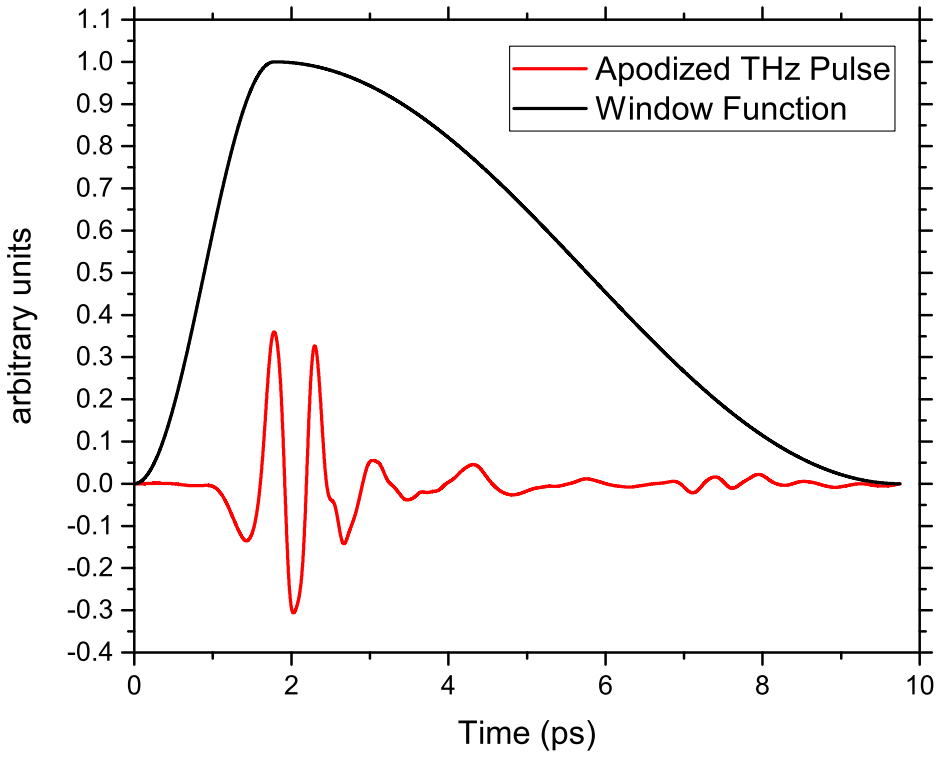

Figure 4.1: The asymmetric Hann window used to apodize linear THz data for spectroscopy. An example apodized THz pulse is plotted for comparison.

This can be especially useful for high signal-to-noise data since increasing the signal-to-noise ratio increases the accuracy of the measurement of peak centers. In addition to interpolation, zero padding to create a data set of length 2^N, where N is a positive integer, maximizes the speed of the FFT calculation.

4.2 Analysis of nonlinear THz data

The heterodye-detected TKE signals can be analyzed in two complementary ways. First, the time-domain data can be modeled based on theories about what contributes to the signal at different times. This can provide some means to connect physical observables with a microscopic picture. Second, the Fourier transform of the time-domain data can be calculated to find a nonlinear THz

spectrum. Being able to plot a nonlinear spectrum is an important step towards the ultimate goal of generating a 2D THz spectrum.

4.2.1 Time-domain analysis

The measured HD-TKE signal can be broken up into distinct contributions. First, a purely electronic response that leads to the peak of the signal. At the peak, the nuclear response then comes to dominate the electronic response. This region contains no information about the molecular dynamics. From 0 to ∼2 ps after the peak, intermolecular interactions dominate the signal. Finally, after 2 ps or so, the reorientational motion of individual molecules returning to an isotropic distribution of orientations dominates the signal. Different functional models are needed to fit the different regions.

This can be clearly seen in the data from carbon disulfide plotted in Figure 4.2. The fast electronic response can be seen from -1 to 0 ps. It can only be modeled poorly by an exponential and is often thought of as a delta-function like response. The slope of the line changes for 0 to 2 ps and is not explicitly linear. Sometimes it is possible to fit a line to the natural log data in this region. This part of the Kerr effect response is much discussed in the literature and remains poorly understood but the general consensus says that the response in this region is dominated by intermolecular modes. It is worth noting that more information can likely be gained from intermolecular modes by Fourier transforming the data as discussed below.

The data from 2 to 10 ps in Figure 4.2 is clearly linear on the natural log plot and thus can be fit with a decaying exponential. The slope of this line corresponds to the time constant for exponential decay. This time constant has proven useful in many situations. When a strong electric field is applied to a liquid, the dipoles of the molecule will orient themselves with the applied electric field. This non-equilibrium distribution then relaxes back to an isotropic configuration. As a measurement of the timescale of this relaxation, this number offers direct insight into the dynamics of molecular liquids.

We developed a robust way to fit the long-timescale data collected on the molecules in this study. It is straightforward to fit an exponential using commercially available software such as OriginPro

2015. The only issue in fitting an accurate value for the exponential decay in our data arose from the fact that we had a negative DC offset in the data. As a result, we needed to zero the data before fitting. This was accomplished by ensuring that we collected data before the THz pulse so that we could measure the DC offset by calculating an average of the points before the rising edge of the electronic response. This offset was added to the data and fitting an accurate exponential became simple.

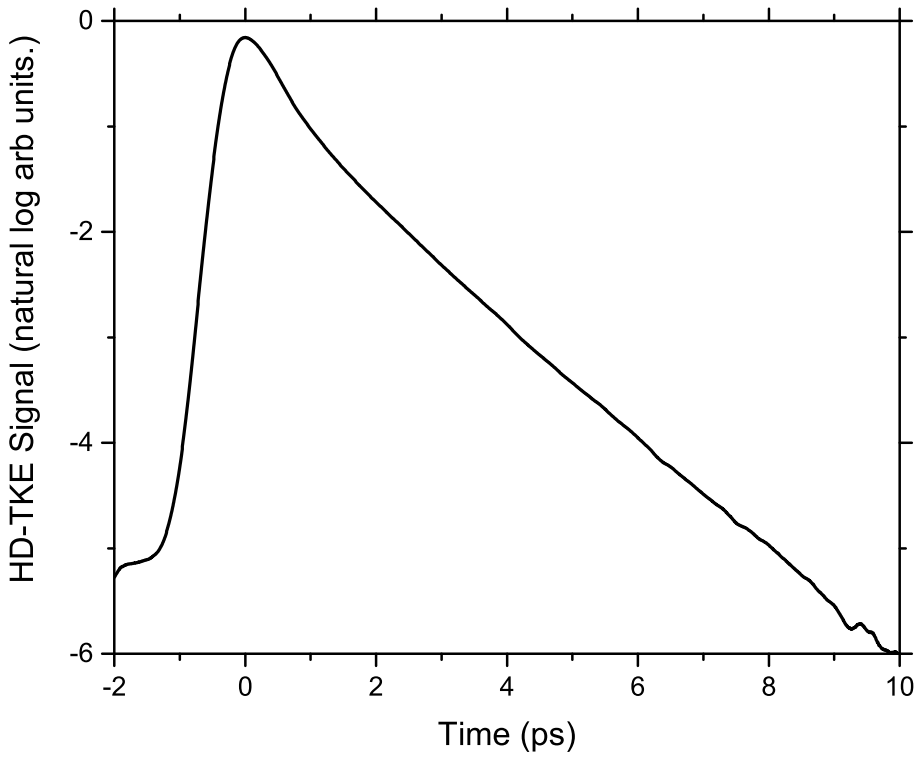

Figure 4.2: Heterodyne-Detected THz Kerr Effect data for carbon disulfide. The ordinate is plotted on a natural log (base e) scale.

4.2.2 Fourier analysis

Nothing matches the firepower that the Fourier transform brings to the analysis of time-domain data. Frequency domain spectra generated by a Fourier transform provide detailed information about the signals being analyzed and present that information in a visually appealing way. The

value of apodization to prevent spectral leakage is discussed at length above. While we felt that it improved the linear THz spectra collected with our spectrometer, apodization made the collection of observation of any features in the HD-TKE possible. This difficulty arises from one of the classic issues associated with from Fourier transforming experimental data: the signal to be transformed starts at a maximum. Without a windowing function, having the maximum value at the start of the FFT will lead to large spectral leakage. Apodizing solves this problem, but care should be taken to try to align the maximum value of the windowing function with the peak of the data. In the case of the HD-TKE data, we note that our THz pulse is about 1 ps in duration, so we set the maximum value of our windowing function to be 1 ps after the start of the scan. This can be seen in Figure 4.3.

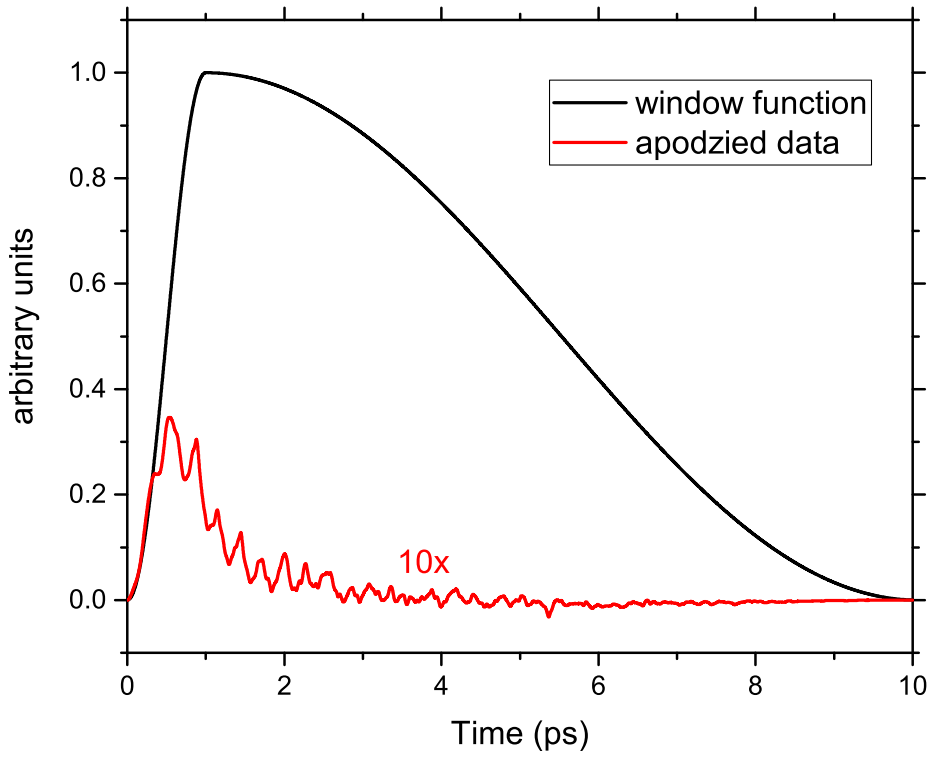

Figure 4.3: The asymmetric Hann window used to apodize nonlinear THz data for HD-TKE measurements. Apodized HD-TKE data from diiodomethane are plotted for comparison. They are also scaled by a factor of 10 for ease of viewing.

Part III

Astrochemical Ices

Chapter 5

Water and carbon dioxide containing astronomical ice analogs

The bulk of this chapter is reproduced from "The structure and dynamics of carbon dioxide and water containing ices investigated via THz and mid-IR spectroscopy," by M.A. Allodi, S. Ioppolo, M.J. Kelley, B.A. McGuire, and G.A. Blake; Physical Chemistry Chemical Physics 2014, 16, 3442-3455. — Reproduced by permission of the PCCP Owner Societies

5.1 Introduction to astrochemical ice analogs

Dust grains play a central role in the chemistry of the interstellar medium (ISM). Hydrogen atoms only react efficiently to form molecular hydrogen with a dust grain acting as a third body to stabilize the new molecular species.[35; 36; 37; 38] In low-mass star-forming regions, analogous to the cloud that formed our own solar system, there exist cores with low enough local temperatures, and high enough density for gas to condense onto dust grains. Simple, gas-phase atoms and molecules accrete onto a dust grain to form an icy outer mantle, and new reaction pathways become available. [39; 40; 1]

The diversity of chemistry possible on the ice surface greatly exceeds the possibilities in the gas phase. In an ice, energetic processing, by UV photons or cosmic rays, excites or breaks chemical bonds, leading to chemical reactions of species within the ice.[41; 42; 43; 44; 45; 46] Thermal processing can occur if different molecules present in the ice initially do not have enough energy to react, and then later gain sufficient energy to overcome a reaction barrier.[47; 48; 49] In addition, atoms and light molecules freeze out onto the grains and diffuse rapidly over the ice surface, inducing chemical reactions.[50; 14; 13; 51; 52; 53; 54; 55] The ice facilitates the interaction between different species and also serves as a third body to stabilize a new molecule if it forms.

Consequently, these solid phase reaction mechanisms can potentially lead to the formation of more complex molecules such as sugars and amino acids. Given that recent work has ruled out a gas phase mechanism in glycine formation,[12] and yet glycine has been detected in comets sampled by the STARDUST mission [11], solid-phase reaction mechanisms on ice grains may provide the main pathway for the formation of complex organic molecules (COMs) in the ISM.[56] In addition, molecular ices on dust grains likely play a fundamental role in the chemistry of planetary ices, which have been observed on different bodies within our solar system.[57; 58]

The role that the *structure* of the ice mantle plays in chemical reactions on icy grain surfaces remains an incompletely explored question in understanding the effect of dust grains on the chemistry of the ISM. Given the icy dust grains' ability to facilitate the interaction between different species within the ice as discussed above, it would be useful to understand, specifically, how the ice structure

can impact diffusion barriers within the ice. Since COMs form as smaller molecules diffuse through an ice, accurate models of diffusion barriers will improve COM formation models.[56; 59]

Mid-infrared (mid-IR) spectroscopy (450 - 4000 cm^{-1}) has been fundamental in improving our understanding of ice and dust in the ISM.[60; 61; 62] As a result, the most abundant simple molecules have been detected in the solid phase via mid-IR astronomical observations.[63] To begin investigating structural effects in ices, many laboratory investigations have been carried out on ice mixtures composed of H_2O and CO_2, the principal focus of this work. Early studies by Bernstein et al. reported how the intermolecular interactions can break the symmetry of different molecules and thus cause significant changes in the IR spectra, including the presence of peaks not observed in a pure CO_2 ice.[64] Galvez et al. and Maté et al. characterized extensively co-deposited and sequentially-deposited H_2O and CO_2 ice.[65; 66; 67] Their work detected structural differences between mixed ices and identified the differences between CO_2 molecules that formed a crystalline layer on top of H_2O, and the CO_2 molecules that diffused into the H_2O sample using Fourier-transform IR (FTIR) spectroscopy and temperature-programmed desorption (TPD) experiments. Öberg et al. investigated segregation within mixed CO_2 and H_2O ice and found that molecules will form segregated groups as long as it remains more favorable to interact with like molecules as opposed to different species.[68] In addition, they also showed that, in contrast with what was previously thought, ice dynamics was thickness dependent. Clearly, IR spectroscopy offers valuable insight into the structure of the ice. However, transitions at IR frequencies correspond to intramolecular vibrational modes of the molecules in the ice, and, thus, IR spectroscopy only detects local changes in structure.

In contrast, TeraHertz (THz), or far-IR, spectroscopy, covering the region from 0.1 to 10 THz (3 - 330 cm^{-1}), directly probes lower frequency vibrations that correspond to low energy intra- and, especially, intermolecular modes. By virtue of probing intermolecular modes, THz spectroscopy is particularly sensitive to the long range interactions between molecules.[69] Since any change to the structure of the ice would affect these long range interactions, THz spectroscopy allows for direct measurements of large-scale structural change. While there has been previous spectroscopic work

done in this region,[70; 71; 72; 73; 74] none of the previous experiments focused on understanding the structure of mixed and layered ices.

There has been some theoretical work focused on mixed and layered H_2O and CO_2 ices.[75; 76] Both works focus on the suitability of the mid- and far-IR for studying structural changes in astrophysically-relevant ices. Lee et al. find a wealth of spectroscopic features in the THz region and conclude that the features of H_2O ice dominate the spectrum in this region. In addition, they find ice layers at different distances from an H_2O-CO_2 interface can have different spectral features which are particularly well pronounced at THz wavelengths.[76] Their results encourage work in the THz region to investigate these effects experimentally. As observational facilities such as *Herschel*,[77] SOFIA,[78] and ALMA[79] continue to produce high-quality sub-millimeter and THz data, complementary laboratory data can provide important structural information about the ice and, indeed, give the scientific community the tools needed to interpret observational spectra and understand ice chemistry in the ISM and exoplanetary systems.

In the present study, we employ THz and mid-IR spectroscopy to characterize astrochemical ice analogs of H_2O and CO_2. We first describe our state-of-the-art setup, which includes a detailed discussion of the time-domain (TD) THz spectrometer built in our lab. To investigate the ice structure, we prepared ices of pure H_2O or CO_2. We then prepared ices composed of distinct molecular layers, as well as mixtures that were co-deposited, and acquired THz and mid-IR spectra after ice deposition and at different temperatures. Our results provide insight into how different layers of ice interact with each other, and how the segregation of more volatile molecules within an ice can affect the its short- and long-range structure, thus demonstrating the importance of THz spectroscopy in astrochemical ice studies. These laboratory investigations have potential implications for future astronomical work.

We present the results in three subsections. THz and mid-IR results for pure ices of H_2O and CO_2 are discussed first. Identifying the features and structure of pure ices allows us to understand how such features change when molecules are mixed or layered. Second, results from experiments of H_2O:CO_2 mixed ices that are co-deposited (CD) are discussed. Finally, data collected from

layered ice samples are presented. The layered experiments performed are Crystalline Sequential (CS) Deposition, Amorphous Sequential (AS) Deposition, and Inverse Sequential (IS) Deposition, where we have used the nomenclature established in the literature.[65] Table 5.1 summarizes the experiments discussed below.

All ices deposited in this study fall into the "thick" regime ($>$ 100 monolayers) and are approximately 0.5-5 μm thick for H_2O ice. To estimate the ice thickness, we first obtained the column densities for H_2O and CO_2 from the integrated intensity of their IR bands using a modified Lambert-Beer Equation. We selected the O-H bending mode for H_2O (1660 cm^{-1}) and the O-C-O bending mode for CO_2 (660 cm^{-1}), and used the relevant absorption band strength as reported in Gerakines et al. 1995.[80] The ice thickness is subsequently estimated by dividing the column density of each species by a conversion factor that is proportional to the density of the species in the ice. The density of H_2O used is 0.9 g cm^{-3}, [81] and the density of CO_2 used is 1.5 g cm^{-3}.[82] To help ensure consistent thickness, we used the height of the OH librational band between 700 - 900 cm^{-1} to asses when to stop deposition of water. The following figures show that the relative thickness of the different ices is comparable. These experiments and others in the cryostat[83] have shown that the ice is stable for at least 24 hrs as long as the temperature is kept below the sublimation temperature of a given ice. Moreover, the residual gasses in the vacuum chamber consist mainly of H_2O, accreting at a rate of 1 x 10^{12} molecules cm^{-2} s^{-1} (0.001 μm hr^{-1}) when the substrate is kept at 10 K. Thus, relative to the ice thickness used in our study, the background water deposition can be considered negligible over the course of the experiment.

It must be noted here that in all of the following THz spectra, there is noise at 3.2 THz that is only the width of one frequency bin. This noise spike appears to be some form of laser noise that we were unable to filter out while conducting these experiments. As such, the point corresponding to this noise feature is not plotted in most of the following spectra.

To quantify the changes in the structure of mixed ices relative to the structure of pure ices samples, a spectral fitting procedure was used. The procedure makes use of a singular value decomposition to compare how the THz spectra of the mixtures differ from those of the pure ices. A set

Table 5.1: List of experiments performed in this work.

Experiment	Method	Ratio	R_{dep} (μm/min)		Thickness (μm)		T_{dep} (K)		Thermal History (K)	
Pure ice										
H_2O	dep	–	0.08		0.3, 2.6, 5.3		150		150	
H_2O	dep	–	0.08		0.4, 1.6, 3.2		10		10, 150	
H_2O	dep	–	0.06		4.8		150		150, 75, 10, 75, 150	
H_2O	dep	–	0.12		2.8		10		10, 75, 150, 75, 10, 150	
CO_2	dep	–	0.13		0.1, 0.3, 0.6, 1.4		75		75, 60, 75, 60, 75, 60, 75, 60	
CO_2	dep	–	0.13		0.2		60		60, 10, 75	
Mixed ice										
H_2O:CO_2	co-dep	1:5	0.22		2.1		60		60, 175, 75, 10, 150	
H_2O:CO_2	co-dep	1:10	0.8		2.3		60		60, 10, 60, 100, 60, 125, 60, 150, 60, 175, 60	
Layered ice			H_2O	CO_2	H_2O	CO_2	H_2O	CO_2	H_2O	H_2O and CO_2
H_2O and CO_2 on top	CS	–	0.4	0.2	2	0.3	60	75	60, 175, 75, 10, 150	75, 60, 10
H_2O and CO_2 on top	AS	–	0.7	0.6	2	0.3	60	60	60	60, 10, 60, 100, 60, 150, 175, 150
			CO_2	H_2O	CO_2	H_2O	CO_2	H_2O	CO_2	CO_2 and H_2O
CO_2 and H_2O on top	IS	–	0.8	0.9	0.2	2	60	60	60	60, 10, 60, 100, 60, 150

Deposition of single species (dep), co-deposition (co-dep), and sequential deposition (CS, AS, and IS) are performed under different laboratory conditions; R_{dep} is the deposition rate of a selected molecule expressed in μm/min; Thickness is expressed in μm; T_{dep} is the substrate temperature during deposition; Thermal History is the temperatures that the ice have been sequentially exposed to. The heating ramp rate is 20 K/min, in all cases.

of four pure H_2O ice spectra forms the basis of components used to create a fit (Figure 5.1). The spectrum of ASW was collected at 10 K from an ice that was deposited at 10 K. For the spectra of crystalline H_2O, a pure H_2O ice was deposited at 150 K and then cooled to 75 K and 10 K, with spectra collected at each of these temperatures. The coefficients resulting from the singular value decomposition reflect the weight of a given spectrum in the fit. The fits can be seen plotted in the figures that follow of mixed and layered ices.

To normalize the fit coefficients for experiment-to-experiment differences in the ices, the coefficients for a given component are multiplied by the integrated area of the mid-IR H_2O bending mode at $\sim$1600 cm^{-1} in the pure ice spectrum for that component. The integrated area of the bending mode of the ice mixture being fit defines the value for 100% area. The coefficients of the fit components are reported as a percentage of the total area of the H_2O bending mode of a given ice mixture being analyzed.

The degree to which the sum of the normalized coefficient percentages approaches 100% indicates the ability of the four component basis to reproduce the spectra of the mixtures being analyzed. In cases where the structure of the mixed or layered ice is not expected to differ from the pure ices structure, such as in the CS deposition, the sum of the fit coefficient percentages is close to 100%. In some cases, however, the sum of the fit coefficient percentages does not approach 100%. This does not signify that the fit procedure works poorly, since the fit still qualitatively reproduces the spectral data; instead, it shows that the structure of that ice differs somehow from the structure of the pure ice components. When the fit components of a given ice sum to a percentage much less than 100%, that ice cannot be described by a basis consisting only of pure H_2O ice components. Thus, a poor fit actually provides useful information about what the structure of the ice does not look like. In a few specific cases, such as in the CD 60 K/125 K and the CD 60 K/175 K, the procedure was incapable of qualitatively fitting the data accurately and thus shows that the structure of the ice being fit differs significantly from the structure of a pure ice. However, since the fit was unsuccessful, there is no value in trying to quantify the difference from the structure of a pure ice, and so fit percentages

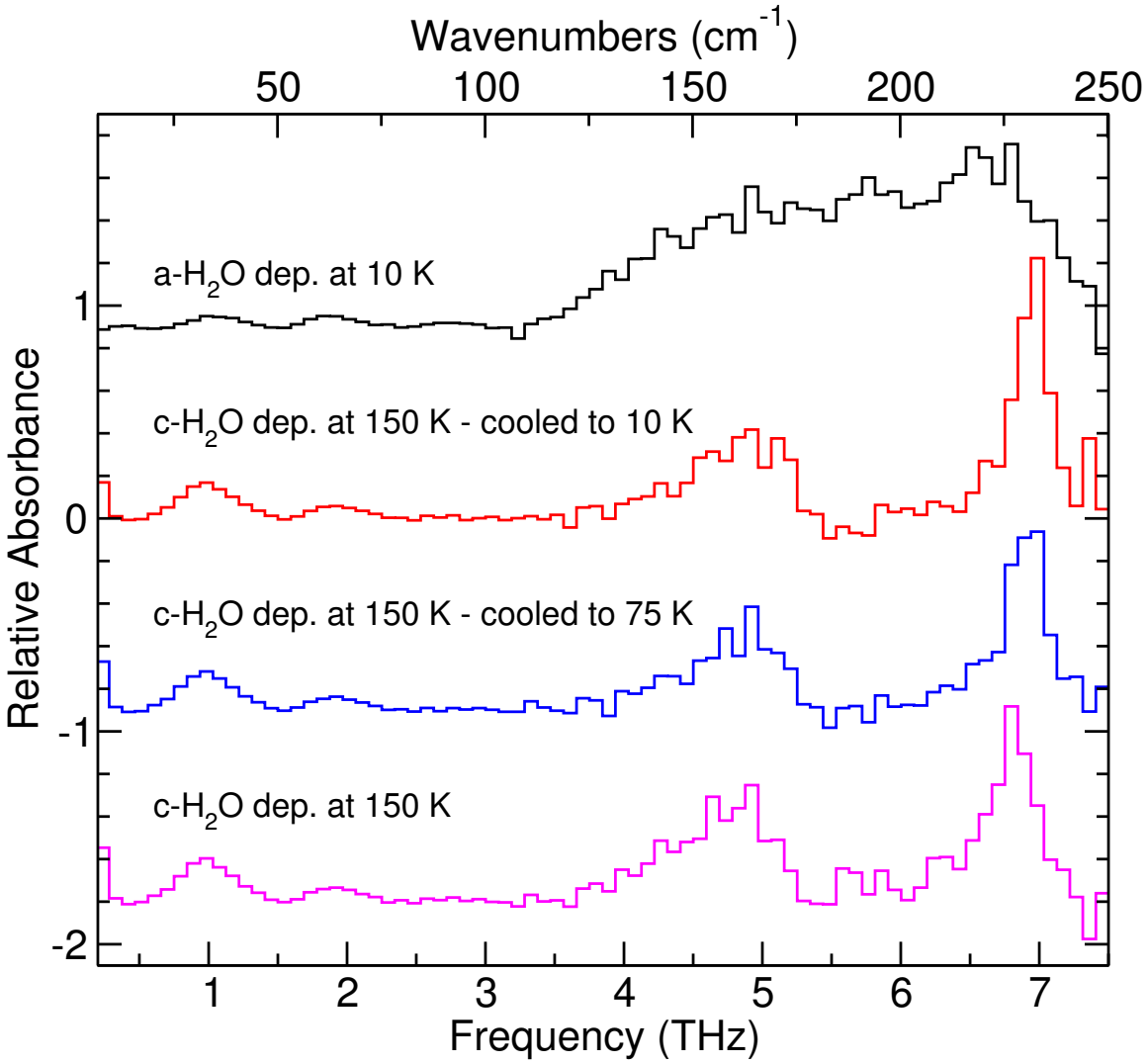

Figure 5.1: Component spectra used to create the fits to the THz data. The top spectrum corresponds to the THz spectra of amorphous H_2O ice, while the bottom three spectra correspond to crystalline H_2O ice. Taken from "The structure and dynamics of carbon dioxide and water containing ices investigated via THz and mid-IR spectroscopy," by M.A. Allodi, S. Ioppolo, M.J. Kelley, B.A. McGuire, and G.A. Blake, Physical Chemistry Chemical Physics 2014, 16, 3442-3455.

Table 5.2: The peak positions of pure H_2O ice absorption features in the THz region in frequency (THz) and wavenumber.

H_2O			
Amorphous		Crystalline	
THz	cm^{-1}	THz	cm^{-1}
1.0	33	1.0	33
1.9	63	1.9[a]	63
5.5	181	4.2[e]	139
		4.7[b]	155
		5.7[c]	188
		6.8[d]	224

The transitions of H_2O ice can be assigned as follows: [(a)]O-O-O bend [(b)]Proton disordered vibration. [(c)]Out of phase vibration of molecules within a bilayer. [(d)]Hydrogen bond stretch between bilayers.[(e)]The feature at 4.2 THz is blended with the feature at 4.7 THz.

are not reported for these data. The specific fits are discussed in more detail in the context of the specific experiments below.

5.2 Pure ices

Pure H_2O has been deposited in two different forms: amorphous solid water (ASW) and crystalline H_2O.[84] Cooling the substrate down below 100 K before deposition ensures deposition of porous ASW, which lacks a well-defined long-range crystal structure. Crystalline H_2O can be formed in two ways. If the substrate is kept above 140 K, crystalline H_2O ice will form upon deposition. Another way to form crystalline H_2O is to deposit ASW at temperatures less than 100 K, which is then annealed. Above 140 K, ASW undergoes a non-equilibrium transition to the more thermodynamically stable, crystalline H_2O form.

Figure 5.1 highlights the THz spectroscopic differences between ice structures formed at different deposition temperatures. Both crystalline and amorphous H_2O have an absorption feature at 1.9 THz. ASW resulting from deposition at 10 K has one broad absorption feature starting at approximately 3.1 THz and extending out past 7.5 THz. In the corresponding region for crystalline H_2O, deposited at 150 K, distinct peaks with the following assignments[69; 85] are seen: 6.8 THz (hydrogen-bonded bilayer stretch), 5.7 THz (out-of-phase vibration within the bilayer), 4.7 THz (proton disordered motion), 4.2 THz, and 1.9 THz (corresponding to an O-O-O bend), which are

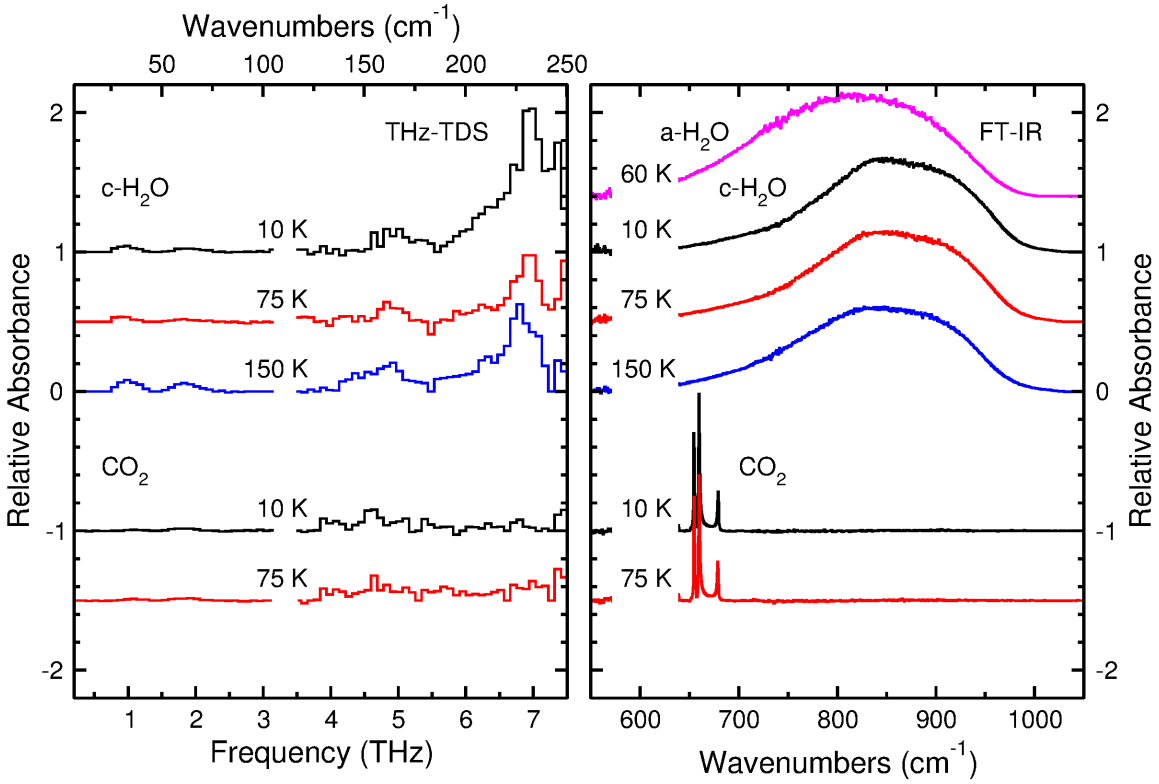

Figure 5.2: THz spectra (left panel) and mid-IR spectra (right panel) of pure crystalline H_2O and pure CO_2 at different temperatures. Both molecules were deposited at 60 K and then the ices were annealed. The H_2O was annealed at 175 K, while the CO_2 was annealed at 75 K. Taken from "The structure and dynamics of carbon dioxide and water containing ices investigated via THz and mid-IR spectroscopy," by M.A. Allodi, S. Ioppolo, M.J. Kelley, B.A. McGuire, and G.A. Blake, Physical Chemistry Chemical Physics 2014, 16, 3442-3455.

in good agreement with theory and previous experiments.[86; 87; 72; 88] The peak positions of the THz features for the pure ices studied are summarized in Table 5.2.

In addition to the features described above, a feature appears in these spectra at 1 THz that has not been previously observed in far-IR experiments, and so we tentatively report a new feature at 1 THz. This feature has likely not been seen in previous work because a TD THz spectrometer, like the one used in this study, has a higher signal-to-noise around this band than a comparable far-IR FTIR study. Over the 0.1 to 3 THz region, a plasma emitter produces more photons than the incoherent source in an FTIR, and so features which would have been below the noise level of the previous work can be detected with our TD THz spectrometer. As such, previous experiments did not extend below 50 cm^{-1} and were thus unable to see this feature.

The results of the other method of preparing crystalline H_2O are shown in Figure 5.2. In contrast with Figure 5.1, where crystalline water ice was prepared by deposition at 150 K, the crystalline H_2O ice presented in Figure 5.2 was deposited as ASW at 60 K, then annealed to 175 K and subsequently cooled. In these experiments, H_2O transitions from compact amorphous to crystalline ice start at $\sim$ 140 K, in good agreement with the literature. Annealing the ice to 175 K should ensure that the amorphous to crystalline transition is fully completed.[89] There will be some mass lost from the ice when annealing at such high temperatures. However, because of the thickness of the ice, such loss is negligible. Under these vacuum conditions, H_2O molecules start to desorb from the ice at $\sim$170 K.

The H_2O spectra in both Figures 5.1 and 5.2 illustrate the spectral changes as a function of temperature. As the cryostat cools the ice sample, the THz feature that peaks at 6.8 THz becomes sharper and more intense at 10 K relative to the same feature at 150 K because cooling the sample will reduce the thermal population of hot-band states of the vibration. The same is true for the shoulder at 5.7 THz. These changes in shape may be useful for determining the temperature of an ice detected in space from its THz spectrum.

Figure 5.2 shows the absorption spectrum for pure CO_2 ice. Although Moore and Hudson reported that CO_2 should have one narrow feature at 3.3 THz,[72] we observe no unambiguous features in our spectra. This is likely caused by a combination of sensitivity and, especially, resolution, owing to the proximity of this feature to the noise spike at 3.2 THz in our experiments. Molecules of CO_2 begin to desorb at $\sim$90 K from the ice, and an ice of pure CO_2 will be fully desorbed at 100 K under these experimental conditions. In the following sections we will show that the desorption temperature of CO_2 varies with respect to the ice composition.

In conjunction with the THz spectra, the right panel of Figure 5.2 also shows the mid-IR spectra collected with the FTIR spectrometer from the same samples. This portion of the spectrum shows the librational mode of water ice and is a useful region of the spectrum to consider because resonances corresponding to the bending mode of CO_2 also appear in this same spectral window. A spectrum of ASW is presented first for comparison, and one can easily see the differences in shape between the amorphous and crystalline ice. The ASW peak is more symmetric than that of crystalline H_2O, and

this asymmetry becomes more pronounced as the crystalline ice cools from 150 to 10 K. These FTIR spectra are also useful because CO_2 shows clear resonances distinct from those of H_2O ice. There are four peaks which appear in the spectrum of CO_2. The two main peaks centered around 660 cm^{-1} are the main features of the CO_2 bending mode for *S*-polarized light. The peak at 680 cm^{-1} is the signature of the CO_2 bending mode for *P*-polarized light. Given that the angle of incidence of the IR beam is 45° and that there is no polarizer along the beam path, the FTIR spectra in this work will show contributions from both polarizations of light. The final peak centered around 640 cm^{-1} is much weaker, and it corresponds to the $^{13}CO_2$ bending mode. Analysis of FTIR data for CO_2 allows for an effective determination of whether a mixed ice sample still contains small amounts of CO_2, since the THz spectra of this molecule do not provide distinct and strong absorption features.

5.3 Co-deposition of mixed ices

The importance of CO_2 in this study stems from how its presence affects the structure of H_2O ice. In the ISM such a mixture could arise from the formation of CO_2 within a polar ice.[90] Consequently, it is interesting to know if and how the presence of CO_2 would affect the structure of the ice in which it exists.

5.3.1 Directly annealed mixture

Figure 5.3 presents the data from two different experiments. In the top three spectra of the figure, a H_2O:CO_2 mixture was prepared in the dosing line and deposited onto the substrate kept at 60 K. Immediately following deposition, the ice was annealed to 175 K at a rate of 20 K per minute and held at that temperature for several minutes. While held at that temperature, monitoring with the FTIR spectrometer showed that some mass is lost from the deposited sample, mostly from CO_2 desorption. The sample was then cooled and spectra collected at 75 K and 10 K, and then finally warmed to 150 K, where spectra were acquired. The peaks of the H_2O bending mode and the CO_2 bending mode at 1600 and 600 cm^{-1}, respectively, are integrated and, using the relevant absorption band strengths,[80] we determine that we have a mixture with a H_2O:CO_2 ratio of ∼5:1.

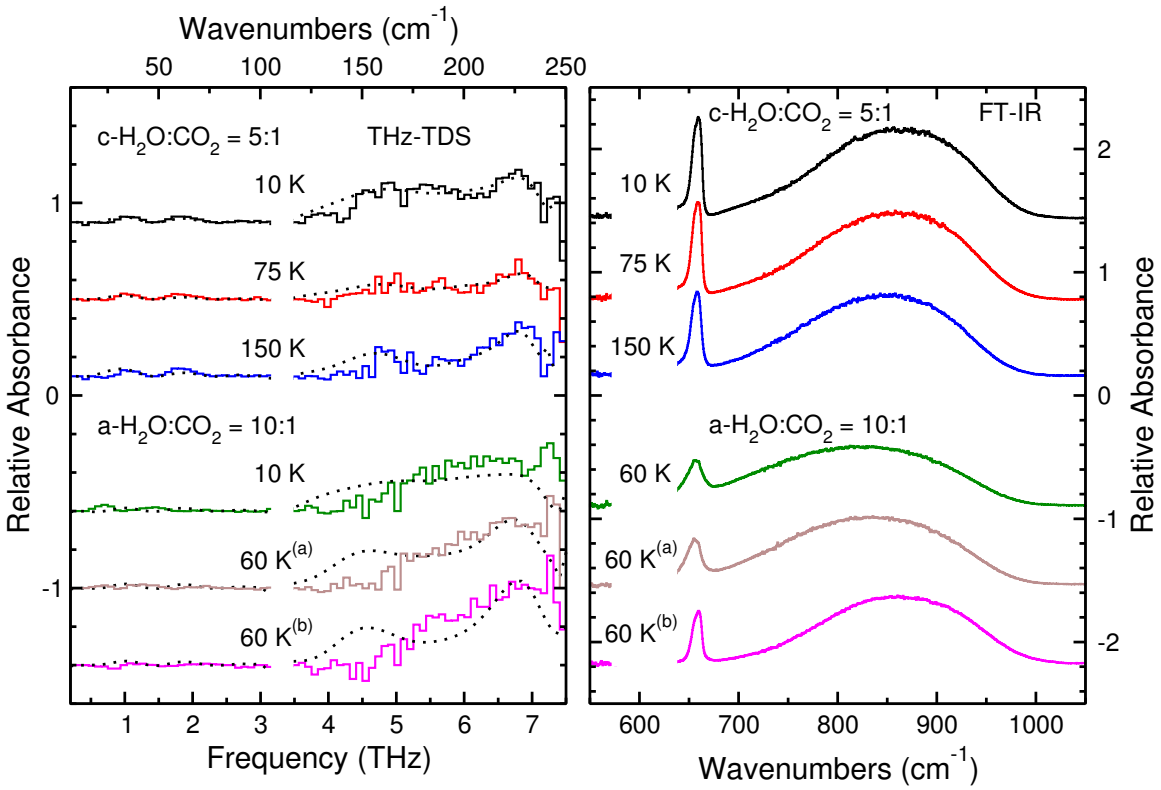

Figure 5.3: THz spectra (left panel) and mid-IR spectra (right panel) of mixed H_2O and CO_2 ice co-deposited. The spectra are labeled with the temperature at which they were collected. The dashed lines in the plot correspond to the fits calculated for the data from the spectra of the pure species, which are plotted with a polynomial spline fit for clarity. The components of the fits are summarized in Table 5.3. The superscripts denote the temperature to which the ices were annealed: $^{(a)}$annealed to 125 K, $^{(b)}$annealed to 175 K. Taken from "The structure and dynamics of carbon dioxide and water containing ices investigated via THz and mid-IR spectroscopy," by M.A. Allodi, S. Ioppolo, M.J. Kelley, B.A. McGuire, and G.A. Blake, Physical Chemistry Chemical Physics 2014, 16, 3442-3455.

Annealing at such a high temperature should force the water to become completely crystalline,[89] and one can see that the spectra of the mixture exhibit THz features that are quite similar to crystalline H_2O at 10 K and 75 K but differing in intensity and structure. Compared with the spectrum of pure crystalline H_2O ice at 75 K, the 6.8 THz, 5.7 THz, and 4.7 THz features are not as intense in the spectrum of this ice. Even at 10 K, where the pure ice features are sharpest and most intense, the 6.8 THz feature in Figure 5.3 does not appear to change compared to the spectrum at 75 K.

The changes in these transitions results from the presence of CO_2 in the ice. One can see in the right panel of Figure 5.3 the resonance corresponding to the CO_2 bending vibrational mode. The shape of this peak is qualitatively different from that of pure CO_2, since now only one peak with a Lorentzian lineshape is observed as opposed to the three peaks observed previously. Figure 5.3 shows that, even though the ice was annealed to a temperature above the CO_2 sublimation temperature, not all of the CO_2 molecules leave the ice. This effect has been previously observed by temperature-programmed desorption (TPD) experiments using a quadrupole mass spectrometer (QMS).[91] As a result of the co-deposition of the two molecules, some CO_2 molecules remain trapped by the molecules deposited on top of them. We thus observe the "interior" CO_2 as discussed previously in the literature.[65; 66; 67] Clearly, after annealing, the trapped CO_2 molecules affect the ability of the H_2O molecules to reorient themselves to form long-range order within the solid ice and properly crystallize, but the observed structure does differ from that of pure ASW.

By comparing the mid-IR data given in the top three spectra in Figure 5.3 with the top three spectra in Figure 5.2 (right panel), it is possible to conclude that the H_2O lacks a fully crystalline structure. However, from the THz spectra alone the lack of crystalline H_2O features is also clear. In addition, given that features in the THz region involve the longer range coordinated motion of many molecules, the THz data also provide insight into the location of the CO_2 molecules within the ice by observing which spectral features are disrupted.

To quantitatively characterize the structure of the ice, we fitted the THz spectral profile of the features shown in Figure 5.3 as discussed in Section 3.1. The fits to these spectra, plotted in Figure

Table 5.3: The components of pure crystalline H_2O and ASW ice features that compose the fits to the experimental data.

	Fit Component (percentage)				
Experiments	ASW 10K	c-H_2O 10 K	c-H_2O 75 K	c-H_2O 150 K	Total(%)[a]
CD[b] 10 K	59	18			77
CD[b] 75 K	21		17		38
CD[b] 150 K	20			47	67
CD[c] 10 K	69				69
CD[c] 60 K/125 K[d]					_[e]
CD[c] 60 K/175 K					_[e]
CS 10 K		99			99
CS 60 K		99			99
AS 10 K	95				95
AS 60 K	87				87
AS 60 K/ 100 K	73			12	85
AS 150 K	66			21	87
AS 150 K/175 K	61			22	83
IS 10 K	33				33
IS 60 K	60				60
IS 60 K/100 K	52			8	60

[a] The percentage does not always equal 100% because the structure of the ice cannot always be described by the components of pure H_2O used. [b] These are the data for the CD experiments which were directly annealed. [c] These are the data for the CD experiments which were cooled first and then stepwise annealed. [d] In this table 60 K/100 K is defined as a spectrum collected at 60 K for an ice that was first annealed to 100 K. This convention holds for all lines in the experiments column where two temperature values are listed. [e]No percentages are reported in this case since the fitting procedure produced a poor fit to the actual spectra. As such, a quantitative analysis is not meaningful.

5.3, agrees well qualitatively with the spectra of the mixed ice. The fits show that the pure H_2O bands at 4.7 and 5.7 THz are blueshifted in the spectra of the mixtures while the 6.8 THz feature is always fit well by using a spectrum of pure H_2O ice acquired at the same temperature as the mixed ice. In all of these cases, a fit component corresponding to ASW was needed to improve the fit. The specific fit components for each spectrum are summarized in Table 5.3. Since the percentages listed in the table do not approach 100%, they provide another piece of evidence showing that the structure of these ices differs from the structure of pure crystalline water ice.

5.3.2 Cooled before annealed mixture

The bottom set of spectra in Figure 5.3 correspond to a mixed ice prepared similarly to the ice in the top three spectra. A H_2O:CO_2 gaseous mixture, was prepared in the dosing line and deposited onto the substrate held at 60 K. Similar to the previous section, after deposition, the mid-IR H_2O and CO_2 bending modes were used to derive the column densities and determine that after deposition the ice mixture has a H_2O:CO_2 ratio of ∼10:1. In this set of experiments, the ice was first cooled to 10 K and a spectrum was collected. Then the ice was warmed back up to the deposition temperature

of 60 K. The spectra at 10 K and 60 K agree qualitatively with the shape of the spectrum of pure, ASW in Figure 5.1; however, the relative absorbance of this mixed ice does not appear as strong as that of the pure H_2O. We can see from the mid-IR data in Figure 5.3 that both CO_2 and H_2O are present in this ice. It is worth noting that the shape of the mid-IR CO_2 bending mode in these unannealed spectra differs qualitatively from the shape of the bending mode in the annealed spectra at the top of the figure. The peak in the unannealed spectrum appears to have a flat top as opposed to a smooth curve and is redshifted relative to the annealed spectrum. Also, the H_2O librational mode appears broader in the unannealed spectra than in the annealed spectra.

This ice was then annealed. First, the ice was annealed to 100 K and cooled down to 60 K. Both the THz and FTIR spectra show no appreciable change compared to the unannealed spectra at 60 K. The ice was then subsequently annealed to 125 K, 150 K, and 175 K, with a cool down cycle returning the ice to 60 K each time after annealing. There is no significant change to the ice after annealing *until* the ice is annealed up to 175 K. However, the THz spectrum of the ice after annealing to 175 K does not match the spectrum taken of the ice that was directly annealed. As discussed above, the THz spectra of the ices that were directly annealed after deposition show features of crystalline H_2O. However, the spectra of the ice that was cooled before being annealed show features that correspond more to the structure of ASW.

A comparison between the bottom set of spectra in Figure 5.3 and the spectral fits as discussed above shows that the presence of CO_2 in the ice causes a blue shift of the broad band of amorphous water ice at 10 K. Moreover, although the last spectrum annealed to 175 K shows a weak band around 6.8 THz because of crystalline H_2O, the 4.7 and 5.7 THz bands are blue shifted and/or weak. In this case, and for all spectra annealed above 100 K, the fit cannot reproduce the data satisfactorily. This shows that the structure of this ice is significantly different from the spectra of the pure ices used in the fits.

5.3.3 Discussion of both ices

THz spectroscopy probes the intermolecular vibrations of an ice as opposed to the just intramolecular vibrations which dominate the mid-IR. Different intermolecular interactions will, of course, affect the band profiles in a mid-IR spectrum. However, the features in the THz region that require the coordinated motion of many molecules will necessarily directly sense disruptions in the material structure and can disappear entirely from the THz spectrum if those interactions are removed.

The mid-IR FTIR data provide a strong basis for interpreting our THz spectra. None of the data in Figure 5.3 (right panel) show the characteristic asymmetric feature of crystalline H_2O in the H_2O librational band (see Fig. 5.2), thus strengthening the interpretation that CO_2 disrupts the crystallization process of the H_2O ice. In addition, as previously mentioned, one can observe a difference in the features between the directly annealed spectra and the stepwise annealed spectra. With this information in hand, one can learn more about the structure of the ice from the THz spectra.

In particular, the THz region has the potential to indicate the *degree of crystallization*, and the *history* of transformations that an ice has undergone. Generally speaking, spectroscopy is not sensitive to the history of transformations an ice has undergone. However, if the different ices were to start at the same unstable equilibrium point and then undergo different, irreversible non-equilibrium transitions, the different histories would result in different spectra. For the ice that was annealed directly after deposition, we note that it does appear, from the THz spectra, to have some crystalline H_2O structure. In this case, the THz spectra provide some insight into the degree of crystallinity. The ice was annealed to 175 K, where one would have expected the crystallization process to be completed (see Fig. 5.2). The fact that its features are attenuated somewhat relative to the spectrum of pure crystalline H_2O deposited at 60 K and annealed to 175 K likely results from the presence of segregated CO_2 within the ice. Since it is known that segregation occurs quickly in thick ices,[68] this ice most likely contains large regions of crystalline H_2O, but the pockets of segregated CO_2 prevent a fully uniform crystalline solid from forming, and thus the peak strengths and shapes differ from that of pure crystalline H_2O.

In the other experiment, by cooling the ice immediately after deposition, the ice was taken below the temperature at which segregation can occur. While there was likely some segregation took place during the deposition process at 60 K, by cooling first and stopping segregation, the CO_2 is left more well mixed with H_2O. Then, by restarting the annealing process in steps, the CO_2 molecules were forced to segregate more locally into smaller domains. In contrast, when the first ice was annealed directly after deposition at 60 K, the segregation rate increased when the temperature was raised. This likely encouraged the formation of large domains of segregated CO_2, and large regions composed entirely of H_2O molecules. Consequently, the features of crystalline H_2O are more pronounced in the directly annealed spectra when compared with the ice that was cooled immediately after deposition. This mechanism can potentially explain the differences observed in the THz spectra between the two sets of experiments.

The results from the quantitative fits discussed above provide further evidence to support the differences in the structure of the ices in the two different experiments. The spectra of the ice that was directly annealed can be fit quite well using these components as seen in Figure 5.3. In contrast, the best fit of the stepwise annealed data still show a peak at 4.5 THz, meaning that when using the fit components corresponding to pure H_2O ice, the fit to the data is unsatisfactory. Consequently, the poor nature of the fit shows that the structure of the stepwise annealed ice differs significantly from the directly annealed ice which can be fit in this multicomponent fashion.

It would also be valuable to know the location of the segregated CO_2 in the structure of the H_2O ice. The 6.8 THz feature in crystalline H_2O corresponds to the stretching of hydrogen-bonded bilayers of H_2O molecules.[69] Since this feature is weak in the THz spectra of the ice that was cooled after deposition, the CO_2 molecules must interfere with the hydrogen bonding between bilayers of crystalline H_2O ice. Most likely, the CO_2 molecules segregate together between bilayers and disrupt the H-bond stretching that give rise to the feature at 6.8 THz. As discussed by Maté et al.,[66] "interior" CO_2 must be located within some type of channels or pores within the ice. However, these authors were unable to determine specifically the location of "interior" CO_2 within their H_2O ice. By using THz spectroscopy and the known assignment of these attenuated features in the

crystalline H_2O ice, our results provide new insight into the specific location of the segregated CO_2 within the H_2O ice. The disruption of the feature at 6.8 THz shows that the CO_2 molecules segregate between the bilayers of the crystalline H_2O ice structure.

We would be remiss if we did not discuss the previous work done in the far-IR on ice mixtures. Moore and Hudson in 1994 also co-deposited a mixture of H_2O and CO_2 and observed a disruption of the crystalline water features after annealing a co-deposited mixture.[72] Our results, however, are an expansion on the previous work in two ways. First, we performed two different CD experiments, one which was directly annealed, and one which was stepwise annealed, and observed different results. Second, given recent theoretical advances in understanding crystalline H_2O structure,[69] and an improved knowledge of segregation dynamics,[68] we can infer the position of the CO_2 within the ice and provide new insight into the structure of ice mixtures by determining what types of pores and channels exist for the CO_2 to occupy.

It must be noted that the ratio of H_2O:CO_2 is different in the two ices discussed above, resulting from the experimental realities of deposition. In an attempt to achieve the same ratio in both ices, the mixing ratio in the dosing line was adjusted to try to account for the mass loss (predominantly of CO_2) when the ice was annealed directly to 175 K. However, the two ratios used were different by too large an amount, which led to the different mixtures observed in the ice. This results in a difference in the ice mixtures of less than a factor of two. Even considering these differences between the ices, the results of our study remain relevant. One might expect that a higher concentration of CO_2 in H_2O would disrupt the crystallization to a greater degree than having a lower concentration of CO_2. However, our results indicate that crystallization of water occurs more readily in the directly annealed mixture that also has a slightly higher concentration of CO_2 with respect to the stepwise annealed mixture. As such, we can conclude that segregation of CO_2 still trapped in a H_2O ice is influenced by the annealing procedure.

5.4 Layered ices

Layered ices present another interesting system where THz spectroscopy may provide some added insight into the long-range molecular structure.

5.4.1 CS Deposition

We prepared a base layer of crystalline H_2O ice approximately 2.0 μm thick by depositing H_2O at 60 K and then annealing the ice to 175 K. The ice was then cooled to 75 K, and a layer of CO_2 approximately 0.3 μm thick was deposited on top of the water. The results of this layered ice can be seen in the top two spectra in Figure 5.4. As these spectra clearly show, the features of crystalline H_2O are still present and undistorted by the CO_2 capping layer. Once the ice sample was heated above 110 K, the CO_2 completely desorbed.

The data from the CS deposition were also fit with the spectral components from pure water ices as discussed above and the fits are plotted along with the data in Figure 5.4. In this case, the fits can reproduce qualitatively and quantitatively all the observed features at the selected temperatures, thus confirming that the CO_2 is not affecting the structure of the crystalline H_2O ice. The 6.8 THz feature is, however, stronger in these CS data than in the fits. This difference is most likely because of the different experimental procedures used to prepared crystalline water ice.

5.4.2 AS Deposition

We then repeated the experiment, but instead of crystalline H_2O, we deposited approximately 2.0 μm of ASW at 60 K and then approximately 0.3 μm of CO_2 on top without changing the temperature. The THz spectra of this ice at 10 K and 60 K show the typical, broad feature from 4 THz to 7.5 THz of pure, amorphous H_2O. As the ice warms, however, the spectra of the layered sample deviate from the sample of the pure ice. In the blue trace in Figure 5.4, we see the spectrum of this ice sample at 60 K after annealing to 100 K. It appears that the broad amorphous band begins to change into the distinct bands of crystalline water, but that the process is not complete. However, when warmed to 150 K, the crystalline H_2O ice features become more apparent. Finally, when the ice is

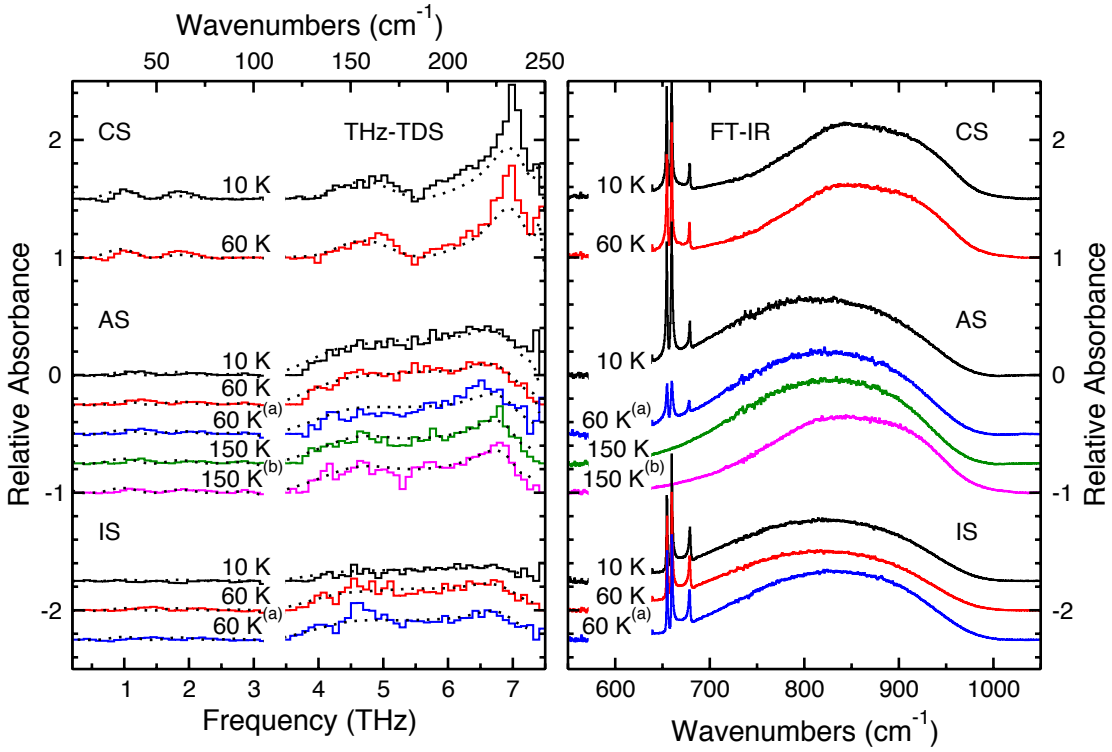

Figure 5.4: THz spectra (left panel) and mid-IR spectra (right panel) of layered ice samples. The spectra collected from the crystalline sequential (CS) deposition are shown in the top two traces, and those from the amorphous sequential (AS) deposition are shown in the middle traces. The spectra collected from the inverse sequential (IS) deposition are shown in the bottom three traces. All spectra are labeled according to the temperature at which they were collected and the conditions under which they were annealed. The dashed lines in the plot correspond to the fits calculated for the data from the spectra of the pure species, which are plotted with a polynomial spline fit for clarity. The superscripts denote thermal processing as follows: $^{(a)}$annealed to 100 K. $^{(b)}$annealed to 175 K. Taken from "The structure and dynamics of carbon dioxide and water containing ices investigated via THz and mid-IR spectroscopy," by M.A. Allodi, S. Ioppolo, M.J. Kelley, B.A. McGuire, and G.A. Blake, Physical Chemistry Chemical Physics 2014, 16, 3442-3455.

annealed to 175 K and then cooled back down to 150 K, the ice features correspond very well to a well crystallized H_2O ice which has been annealed. This can indeed be seen in both the THz spectra and in the mid-IR data presented in Figure 5.4. In addition, spectra in the THz and mid-IR taken at 150 K show that the CO_2 that was sitting on top of the H_2O layer has completely left the ice.

There are, however, differences between the spectra of the CS deposition, seen in the top two spectra of Figure 5.4, and the spectra of the AS deposition seen in the middle five spectra in Figure 5.4. The CS deposition has a THz spectrum that appears qualitatively identical to the annealed pure ices in Figure 5.2, while this is not the case for the AS experiments. The crystalline H_2O features present in the AS spectra after annealing to 175 K are not as sharp or strong as the features present in both the pure annealed H_2O ice or the ice in the CS deposition. From our quantitative fits of the data, we observe that up to 60 K the spectra can be fit with just an ASW component, while above 60 K, a crystalline H_2O at 150 K component must also be included to accurately fit the data. The percentage of the crystalline H_2O component of the fit increases with increasing temperature as shown in Table 5.3; however, since the total percentage does not approach 100% the structure of these ices, even after annealing, is somehow different from that of a pure crystalline H_2O ice. Also, CO_2 is still present in the ice at 100 K indicating that some CO_2 diffused into the water layers underneath.

5.4.3 IS Deposition

We then performed another experiment, where approximately 0.2 μm of the more volatile CO_2 was deposited directly onto the Si substrate at 60 K, and then approximately 2.0 μm of H_2O was deposited as the top layer. These data can be seen in the bottom spectra of Figure 5.4. Immediately after deposition, the sample was cooled to 10 K and spectra collected. Above 100 K, the ice was no longer stable because once enough CO_2 begins to sublime from the ice, the H_2O ice will no longer be in contact with the substrate and the ice will collapse. As such, these experiments will be limited to the temperature range from 10 K to 100 K.

As seen in Figure 5.4 (right panel), both CO_2 and H_2O are present in the ice, and by looking at the shape of the CO_2 bending mode peaks, we can tell that the ice layers remain mostly separate. The bending mode features show the three sharp peaks seen in pure CO_2 as opposed to the one broadened feature seen in the well mixed ices discussed above. One would expect, then, to simply see THz features corresponding to amorphous H_2O; however, the THz spectrum is quite flat and nearly featureless. There does appear to be a subtle bump corresponding to the 4 THz - 7.5 THz amorphous H_2O ice absorption, but it is not especially intense. The CO_2 molecules clearly disrupt the THz active motions in what should be an amorphous H_2O even though amorphous H_2O is clearly present from the FTIR data.

The layered ice was then warmed to 60 K, and the THz features corresponding to ASW become more pronounced. While there is little change in the spectrum collected with the FTIR, it becomes possible to tell from the THz data that there is ASW present in the sample. The ice was then annealed to 100 K and cooled back to 60 K. The spectrum after annealing now has a slightly different shape, but is qualitatively similar to the previous spectrum taken at 60 K. While the mid-IR spectra do show some differences in this case, the differences are not as pronounced as in the THz region.

These spectra can be fit just with an ASW at 10 K component, except for the last spectrum annealed to 100 K, where a crystalline H_2O component at 150 K was included to improve the fit. In this case, we note that the proton-disordered vibrational band at 4.5 THz is present in the data and cannot be fit with the components hereby selected because the 6.8 THz band is completely suppressed by the presence of the CO_2 diffusing into the water top layers. A wider sample of spectral fitting components and a higher spectra resolution may explain the band at 4.5 THz.

5.4.4 Discussion of all three layered ices

Our results for the CS deposition agree well with literature results,[65] as we observe that all of the CO_2 molecules desorb after heating the sample above 110 K. We notice that the crystalline H_2O spectra are in excellent agreement with the spectra of pure H_2O presented in Figure 5.2.

When comparing the AS and CS experiments, the THz spectra provide more information about the structure of the ice when used in conjunction with the mid-IR data. The mid-IR spectra in Figure 5.4 show that the water in the AS experiments crystallizes after annealing to 175 K and has significant similarities with the CS spectrum taken at 60 K. However, the THz spectra of these two ices are quite different. As such, the THz spectra provide more information regarding the structure of the ices than just the mid-IR spectra do alone.

The AS deposition shows results that are different from the results obtained in the CS experiments, but that are similar to the results obtained from the different CD experiments reported above. These spectra are qualitatively similar to those in the CD experiment that was annealed directly after deposition, seen in the top half of Figure 5.3. Both the spectra in Figure 5.3 and Figure 5.4 show the 6.8, 5.7, and 4.7 THz features of crystalline water ice that are attenuated and distorted relative to these features in pure crystalline H_2O ice, and this can be seen in our fits. Clearly, the CO_2 was able to diffuse into the structure of the ASW layer underneath and was trapped in the pores or channels of the ASW[66]. The presence of these CO_2 domains within the ASW prevented the crystallization process for proceeding as it would in the pure H_2O ice. We can thus infer that, while there are large enough domains of water to crystallize, the presence of CO_2 prevents these domains from joining to form a well ordered macroscopic crystal. Instead, crystallization is apparent in both the mid-IR and THz spectra, but the THz features are sensitive to the degree of crystallization of the ice and indicate that the ice differs in structure from that of a pure H_2O sample.

The deposition in the IS experiment again points to the importance of THz spectroscopy in the study of the molecular structure of the ice. The fact that the feature corresponding to ASW is missing from these spectra is unsurprising from the results present in the literature. Maté et al. suggest that as H_2O deposits, CO_2 molecules are immediately incorporated into the structure of the ASW formed.[66] This disruption of the structure of ASW would explain the flatness of the spectrum at 10 K. Once the sample is heated to 60 K, segregation begins to occur, and as Figure 5.4 clearly shows, CO_2 is still present in the ice after annealing to 100 K. Consequently, a broad feature corresponding to that of ASW appears in both of the spectra taken at 60 K (before and

after annealing to 100 K). Since the mid-IR spectra sense only the local environment in which the molecules interact, the THz spectra provide the opportunity to draw stronger conclusions.

5.5 Conclusions from THz ice spectroscopy

We present a new setup consisting of two spectrometers capable of studying astrochemical ice analogs from the THz, or far-IR, region (0.3 - 7.5 THz; 10 - 250 cm^{-1}) up through the mid-IR (400 - 4000 cm^{-1}) with a THz spectral resolution of 3 cm^{-1} and a mid-IR spectral resolution of 1 cm^{-1}. This combination of spectral regions is powerful because we are sensitive to intramolecular modes in the mid-IR and intermolecular modes in the THz. Also, we can compare our mid-IR spectrum to the large body of literature already available in this spectral region. In addition, the new setup described in this work is capable of making a significant contribution to the body of experimental laboratory data that is needed to interpret astronomical observations from *Herschel*, SOFIA, and ALMA. Below, we enumerate our conclusions:

1. Our THz spectra of pure H_2O ice agree well with previous literature studies, and we tentatively report a new feature in both crystalline H_2O and amorphous solid water at 1 THz. This feature may be especially useful for astronomical observations given the current coverage of observational facilities.

2. For experiments where we co-deposited H_2O and CO_2, we observed different structural changes within the H_2O ice based on the rate of segregation. From the differences in the THz spectra, we observe that CO_2 can segregate to disrupt the hydrogen bonding between bi-layers of crystalline H_2O ice and thus infer the location of the segregated CO_2.

3. In the experiments of sequentially deposited ices, we distinctly observed the impact of CO_2 molecules on the structure of the H_2O ice. Although we were unable to observe any features corresponding to pure CO_2 ice, its effect on the THz spectrum was clear: CO_2 disrupted the interactions between H_2O molecules so that the resonances of H_2O ice were attenuated, distorted, and/or shifted.

4. Given the differences in the THz spectra of the CO_2 and H_2O containing ices, THz spectroscopy has the potential to indicate the degree of crystallinity of an ice and the history of thermal transformations within the ice, provided that the history consists of non-equilibrium transitions away from a point of unstable equilibrium.

5. Our work demonstrates the importance of THz spectroscopy in the study of astrochemical ices because features in the THz region are sensitive to long range structural change. In addition, the temperature dependence of the shape of a feature in the THz spectrum of a molecule may provide a useful tool for determining the local temperature of an ice detected in space.

Part IV

Ultrafast Nonlinear TeraHertz Spectroscopy

Chapter 6

Vibrational Quantum Beats in Pure Molecular Liquids Measured with Ultrafast THz Kerr Effect Spectroscopy

Portions of this chapter are reproduced from "Vibrational Quantum Beats in Pure Molecular Liquids Measured with Ultrafast THz Kerr Effect Spectroscopy," by M.A. Allodi, I.A. Finneran, and G.A. Blake; Physical Review Letters, submitted.

6.1 Introduction to nonlinear THz spectroscopy

Since the development of Nuclear Magnetic Resonance (NMR) spectroscopy, and pulsed laser spectroscopy, pump-probe experiments have been able to provide a novel degree of precision in time-resolved measurements. Pump-probe experiments provide the opportunity to see how a linear spectrum evolves as a function of pump-probe delay time, and they contained new information not accessible in a linear spectrum.[92] By employing these techniques, chemists gained new insight into the dynamics and kinetics of chemical reactions and molecular systems. Several new discoveries resulted from the use of pump-probe spectroscopy, including the discovery of the transition state.[93] Pump-probe experiments can also be considered the first non-linear spectroscopic measurement since the measured signal is dependent upon the interaction of two laser pulses and their electric fields with the sample.

The utility of pump-probe experiments illuminates the path toward higher orders of nonlinear spectroscopy that can extract even more information from a system than a pump-probe experiment. The simplest such experiment is correlation spectroscopy (COSY), [4] which can show correlations between resonances, nuclear spins in NMR, or vibrational modes in the IR, allowing for the facile interpretation of the connections between resonances observed in the linear spectrum. A COSY spectrum requires two pulses that are separated in time. In any 2D experiment, there are two frequency axes, a pump axis and a probe axis, as opposed to just one frequency axis in linear spectroscopy or pump-probe experiments. Varying the timing between the two pulses provides a time axis which can be Fourier transformed to produce the second frequency axis for the 2D spectrum, and the connections between modes can be easily seen on the 2D plot. Understanding these connections is fundamental to interpreting inter- or intramolecular energy flow as well as elucidating the time-resolved molecular structure, since couplings between modes can be used to deduce structure. [94]

This insight has revolutionized many fields, protein biochemistry being one example. When NMR spectroscopy is used to investigate the structure of a protein, a linear spectrum does not provide enough detailed information. For a molecule approaching the size of even a small protein, many

spectral features will have the same chemical shift, and a definitive molecular interpretation of the spectrum becomes impossible.[95] However, a 2D spectrum, such as a COSY, will provide coupling information, allowing different sections of the protein to be identified, and the structure analyzed. [4]

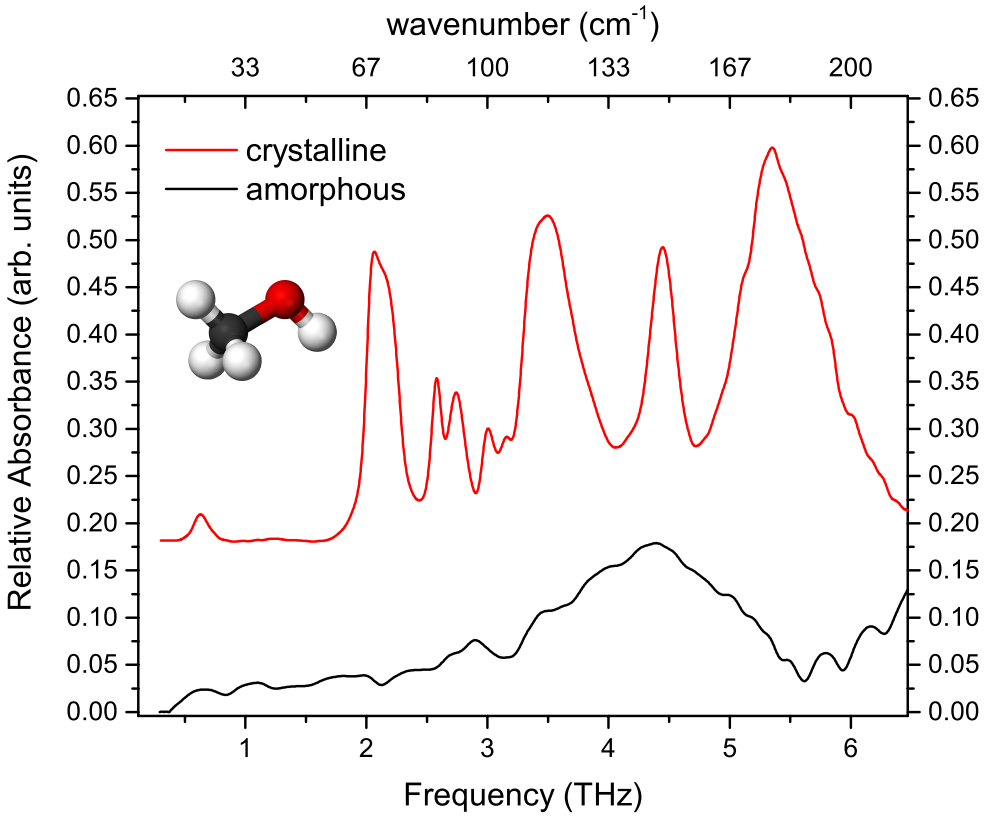

Figure 6.1: THz spectra of crystalline and amorphous methanol collected with the astrochemical ice analog THz TDS apparatus described above.

A good example of how multi-dimensional THz spectroscopy will help the field of THz science mature as a tool for chemical physics can be seen in some of our work on astrochemical ice analogs. The importance of nonlinear techniques to help interpret a linear spectrum becomes clear when one considers the complex features of the spectrum of methanol ice seen in Figure 6.1. How can we begin to interpret and assign the features in these spectra? We see that one band in the amorphous ice becomes several distinct bands in the crystalline ice. Investigating the connections between these features would facilitate their assignment, especially since the theoretical calculation of the dynamics

of complex molecular solids remains a challenging field of research with limited computational tools available to the non-specialist user. In addition, we can address important dynamical questions such as whether the features seen in Figure 6.1 are homogenously or heterogenously broadened on a picosecond timescale.

The answer to this question has important implications for the dynamics of these solids. If these modes are heterogenously broadened, then the features we see are composed of many distinct features. These distinct features can be thought of as one resonance that sits in different local environments. The effect of the different environments creates a set of resonances with slightly different frequencies, thus broadening the measured band. Homogeneously broadened features, then, are in a uniform local environment, such that if the linewidth is broadened in any way from the natural linewidth, it will be broadened uniformly so. If we compare the two methanol spectra in Fig. 6.1, the extremely broad feature in the amorphous methanol spectrum is likely composed of the various bands that appear as distinct features in the crystalline spectrum. Then, the amorphous feature would be heterogenously broadened. It would be even more interesting if the bands in the crystalline spectrum appeared heterogenously broadened. This would be direct evidence for distinct microcrystalline domains in the solid provided by a nonlinear THz measurement.

Outside of astrochemistry, the TeraHertz (THz) region of the electromagnetic spectrum offer spectroscopic insight into a variety of condensed-matter systems ranging from charge transport in semiconductor materials[96; 97] to the biophysics of vision.[98] Of particular interest to chemical physics, the THz-active modes correspond to soft modes of a liquid that participate directly in the molecular dynamics. Given their low energy relative to k_BT, the soft THz modes of a liquid are easily populated by thermal radiation and may be key to understanding the properties of liquids such as water.[99] However, THz spectra of molecular species contain many bands, and many of those are not easy to interpret given the dearth of theoretical and computational studies on modes in this region. However, the THz analogy of a COSY spectrum will offer opportunities to understand the connected nature of some of these modes. This will guide spectral interpretation and provide good opportunities for comparison with calculations or theory.

In addition, the THz region of the spectrum is the first window (as you increase frequency from the radio) where it is possible to generate pulses with enough bandwidth to investigate picosecond dynamics. In contrast, FT-NMR spectroscopy is limited to pulses that are microseconds long. THz pulses contain multiple octaves of frequency content centered around ∼1 THz, thus allowing chemists to investigate the dynamics of these soft THz modes with (sub)picosecond temporal resolution. Since these modes participate directly in the molecular dynamics of the system, THz spectroscopy presents the possibility of directly following, or controlling, the molecular dynamics of a system on a (sub)ps timescale.

To gain new insight into the relationship between molecular dynamics and molecular interactions, the class of nonlinear ultrafast spectroscopic measurements that scale as the applied electric field cubed, generally known as $\chi^{(3)}$ nonlinear spectroscopies, can interrogate how systems respond to different perturbations on the femtosecond to picosecond timescale thus providing detailed dynamical and structural information about a sample. In the visible and the infrared, 2D spectroscopies can perform experiments that show the correlation between modes in a spectrum, and allow for dynamics experiments by varying the timing between different pulses. All $\chi^{(3)}$ 2D experiments require the interaction of three pulses with the sample and can observe changes in dynamical variables as a function of time. The most common technique is a photon echo, or spin echo in NMR. [29] In the echo experiment, two pulses prepare a state, which dephases and propagates forward for some waiting time, and then a final pulse causes the sample to rephase. The emitted signal is strongest at some time after the rephasing pulse, which gives rise to the name echo. While a COSY spectrum can be acquired with two pulses, the addition of the third pulse allows for the waiting time, which can be used to investigate processes such as spectral diffusion or chemical exchange. Little is known about these dynamical processes in the THz regime and photon echo experiments can open entire new fields in chemical physics. Working in the visible or IR, the emitted photon-echo signal can be directly read out by silicon photodetectors. For isotropic systems such as amorphous glasses or molecular liquids, $\chi^{(3)}$ terms are the first nonlinear terms that contribute to the perturbative expansion of the polarization.[29] The variety of existing $\chi^{(3)}$ nonlinear spectroscopies spans the

electromagnetic spectrum, and investigators generally choose the region of the spectrum based on the dynamics of the process they wish to study, e.g., intramolecular vibrational modes with 2D IR vs. nuclear spins with 2D NMR.[4]

The THz analog of 2D-vis/IR has been developed by the Elsaesser lab, and they have demonstrated the power of the technique to perform THz photon echo and other non-linear THz experiments. [100; 101; 102] However, there remain challenges to employing this technique broadly to study molecular systems. First, the THz field strengths are lower than those used in the visible or infrared. This is due to the inefficiency of generating THz pulses. The previous experiments had to specifically choose systems that had strong light-matter coupling.[102] Second, given the broadband nature of the THz pulses produced, the generated power is spread out over more frequencies than in the IR or visible. This makes it harder to move population around, thus weakening the nonlinear signal. Finally, THz detection schemes employ electro-optic sampling, which is the standard technique for detecting ultrafast THz fields.[22; 23] However, it is a nonlinear measurement since the THz fields are read out via the second-order Pockels effect in some medium, usually an electro-optic crystal such as ZnTe or GaP. Since the third-order 2D THz signal must then be measured via a second-order process, the final signal is inherently weaker than third order.

The family of $\chi^{(3)}$ spectroscopies is not limited to photon echoes. The Kerr effect is a nonlinear process that results in a change in the refractive index of a material. The change in refractive index is proportional to the square of the applied field and can be measured by passing another field through the material, making the resulting process third order in field.[26] This technique has been widely employed in ultrafast spectroscopy and is known as Optically-heterodyne-detected optical Kerr effect (OHD-OKE) spectroscopy. It has been especially productive in measuring the ultrafast dynamics of liquids, as it is the most sensitive technique available to ultrafast spectroscopists.[103] However, it is inherently limited to the study of Raman active modes.[104; 105; 29]

One $\chi^{(3)}$ spectroscopy with the potential to explore new dynamics is ultrafast TeraHertz Kerr Effect (TKE) spectroscopy.[106] Fundamentally, it requires two ultrafast pulses: one high-energy THz pulse capable of generating electric fields greater than 100 kV/cm, and an optical detection

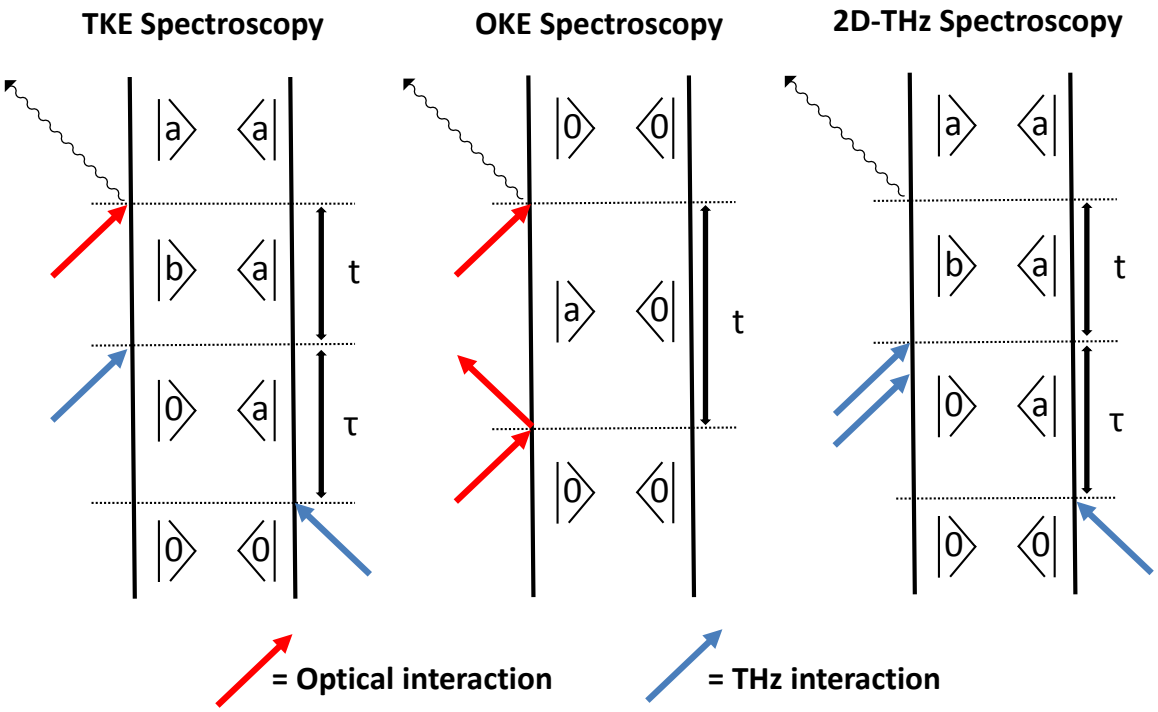

Figure 6.2: Feynman diagrams of the three $\chi^{(3)}$ spectroscopies discussed in the text. The labels a and b refer to arbitrary labels of vibrational quanta.

pulse. The high THz field strengths allow for a nonlinear THz interaction to produce an anisotropy that the optical pulse measures. As a $\chi^{(3)}$ nonlinear process requiring two THz field interactions, TKE spectroscopy was the first technique to measure a signal that is nonlinear in THz field on a molecular system. A comparison of the pulse sequences used in the OKE, TKE, and 2D THz can be seen in Figure 6.2.

The pioneering work by Hoffmann et al.[106] resulted in TKE measurements that were detected in an optical homodyne fashion. Consequently, their measurements were limited to measuring weakly absorbing samples. To achieve the sensitivity necessary to study complex liquids, such as proteins in solution, state-of-the-art OKE spectrometers employ an optical heterodyne-detection (HD) scheme, where the polarization of the optical detection pulse is tuned to create an effective local oscillator instead of a homodyne detection setup. The heterodyne detection increases the detection sensitivity since the measurement scales both with the magnitude of the local oscillator and the magnitude of the molecular signal,[94] thus ensuring that the measured signal scales linearly with the molecular

signal. HD-OKE instruments are sensitive enough to observe vibrational quantum beats in the time domain that can be Fourier transformed to produce the low-frequency depolarized Raman spectrum of the liquid.[29]

In addition, the previously demonstrated TKE work made use of $LiNbO_3$ as their source of high-field-strength THz pulses. This technique is capable of generating THz electric fields in excess of 1 MV/cm, but the bandwidth of the pulses produced is limited to ∼3 THz (100 cm^{-1}) of bandwidth. While the window from 0-3 THz is most accessible with THz time-domain spectroscopy, as shown both in the literature and in our work on astrochemical ice, many important vibrational modes of molecular systems (e.g. hydrogen bond stretches) exist in the 3 to 10 THz (100 to 330 cm^{-1}) range. Thus, the ideal $\chi^{(3)}$ nonlinear THz spectroscopy will cover the entire 0.1 to 10 THz window. In addition, this bandwidth will enable single-cycle THz pulses short enough to achieve sub-100 fs time resolution for nonlinear THz spectroscopy.

In this chapter, we report the development of a heterodyne-detected THz Kerr Effect spectrometer capable of measuring vibrational quantum beats in molecular systems. The heterodyne detection significantly improves the signal-to-noise ratio relative to the previous implementation.[106] This allows us to measure the HD-TKE response of polar molecules that have dipolar vibrational resonances in the THz region of the spectrum such as tetrahydrofuran (THF). In addition the heterodyne-detection allowed us to measure long-lived vibrational coherences in diiodomethane initiated by the interaction of the liquid with a THz pulse. We clearly observe vibrational quantum beats in the time-domain data that are subsequently Fourier transformed to yield a spectrum. Consequently, we report the first dipolar nonlinear-THz spectra of molecules and discuss how this opens the door to other nonlinear THz spectroscopies capable of measuring the ultrafast dynamics of molecular systems in the condensed phase.

6.2 Results and Discussion

The instrumentation needed to measure nonlinear THz spectra has been described in detail in Chapter 3. In brief, approximately 450 mW of 1450 nm light from an ultrafast optical parametric

amplifier (OPA) passes through a DSTMS crystal (Rainbow Photonics) set on a 3 mm diameter aperture to produce ∼160 nJ THz pulses. After magnifying the beam waist by a factor of 7.5, the THz beam passes through a wire-grid polarizer set at 45° relative to the polarization of the 800 nm probe beam and is then focused onto the sample to generate a THz electric field in excess of 300 kV/cm.

To measure the magnitude of the THz electric field used in these experiments we first had to measure the THz power of the individual pulses. We used a Gentec-EO inc. QS3-IL broadband pyroelectric detector mounted in a QS-I-TEST box. We measured a THz power of 164 μW, which, when divided by the 1 kHz repetition rate of our laser, yields 164 nJ THz pulses.

Since we are interested in the magnitude of the THz electric field at the sample, we must know the spot size of the THz beam at that point. This can be calculated using Gaussian beam optics. The THz beam is emitted by the DSTMS crystal fixed on a mount with a 3 mm diameter aperture. This gives us a starting beam waist of 1.5 mm. The beam is then magnified through a reflective Gaussian beam telescope with optics chosen to yield a magnifying power of 7.5. Thus, before being focused onto the sample, the THz beam has a beamwaist of 11.25 mm. The optic which focuses onto our sample has a two inch effective focal length. As such we can calculate the beam waist at the focus of the optic (ω_f), and thus at the sample, using the following equation:

$$\omega_f = \frac{\lambda f}{\pi \omega_\circ}, \tag{6.1}$$

where f is the focal length, λ the wavelength, and $\omega_\circ$ the input beam waist. Since larger wavelengths will lead to larger spot sizes, we can calculate an upper bound by choosing λ =1.5 THz, which is also the frequency with the peak power in our pulse. This gives us a value of ω_f =286 μm. We then perform a Poynting vector analysis where we integrate over this spot size. To get the final value for THz electric field, we use the shape of the THz electric field measured in GaP(110) and THz pulse energy measured with the Gentec detector. This yields a value of 335 kV/cm at the peak of the THz pulse.

Roughly 2 mW of 800 nm light from the 1 kHz, 35 fs Ti:Sapphire regenerative amplifier (Coherent Legend) that seeds the OPA is sent down a delay line fitted with a retroreflector for precise control of the arrival time of the probe at the sample. The beam passes through a hole in the back of the THz-focusing mirror, and hits the sample in a z-cut quartz cuvette of 1 mm path length.

The 10^5:1 polarizer, $\lambda/4$ plate, and a Wollaston prism placed after the sample that serves to split the orthogonal polarizations of the probe beam are critical to the heterodyne-detection scheme. By adjusting the 800 nm polarizer such that almost all the light is in the s-polarization, the small fraction of light that is p-polarized acts as a 90° out-of-phase local oscillator that is heterodyned with the molecular Kerr effect signal on a pair of photodiodes. This scheme ensures that only the backgroundless birefringence signal is measured [28; 29]. An iris in front of the photodiode is used to attenuate the s-polarized beam so that it is of a comparable magnitude to the p-polarized beam [24; 25].

The 1450 nm beam is modulated with an optical chopper at 500 Hz and photodiode signals are sent to a digital lock-in amplifier where they are subtracted, and the TKE signal is measured. More details regarding the instrumentation and optics can be found in our earlier work on linear THz spectroscopy and references therein [8; 107].

The heterodyne-detected signal measured here can be written as

$$S(t) = \int_{-\infty}^{\infty} dt\; E^{*}_{LO}(t) E^{(3)}_{Sig}(t), \tag{6.2}$$

where $E^{*}_{LO}(t)$ is the electric field of the local oscillator pulse created using the polarizer. The third-order electric field measured, $E^{(3)}_{Sig}(t)$, is directly proportional to the third-order molecular polarization after a phase shift:

$$P^{(3)}(t) = E^{pr}_{j}(t-\tau) \int_{0}^{\infty} d\tau'\, R^{(3)}_{ijkl}(\tau') E^{THz^{*}}_{k}(t-\tau') E^{THz}_{l}(t-\tau'), \tag{6.3}$$

where $R^{(3)}_{ijkl}(\tau)$ is the 3^{rd}-order response function of the liquid, τ is the time between the THz and 800 nm pulses, and $E^{pr}(t-\tau)$ is the probe pulse electric field [94; 29]. The response function,

$R^{(3)}_{ijkl}(\tau)$, can be separated into electronic and nuclear components. Since the THz field is non-resonant with any electronic transitions, only the nuclear components of the response function contain any information about the molecular dynamics. Given that $R^{(3)}_{ijkl}(\tau)$ is directly related to the emitted polarization, we can thus relate our measured signal, $S(t)$, to the molecular dynamics initiated with the THz pulse.

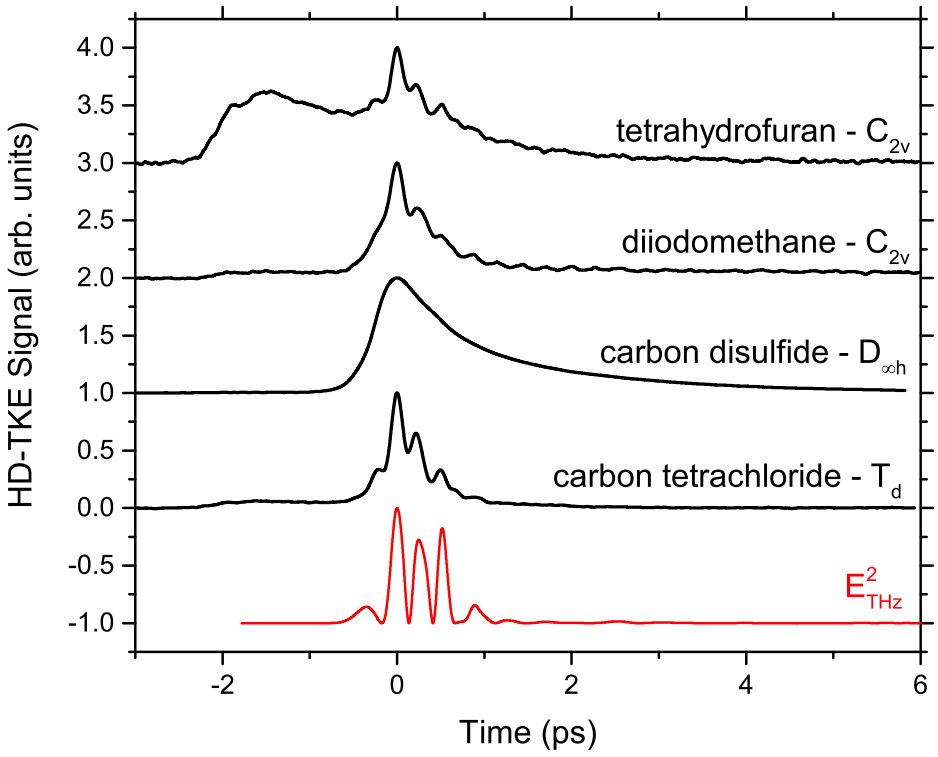

Figure 6.3: The heterodyne-detected THz Kerr effect signals of the molecules in this study. Vibrational quantum beats are clearly visible in diiodomethane. All molecules are labeled with their point group. The bottom trace is the square of the THz electric field applied in these measurements. Note that all data are normalized and offset for clarity. Reproduced from Allodi et al. "Vibrational Quantum Beats in Pure Liquids Measured with Ultrafast TeraHertz Kerr Effect Spectroscopy" *Physical Review Letters, submitted.*

The HD-TKE signals of the molecules investigated here, along with the trace of the THz electric field squared (E^2_{THz}) measured via electro-optic sampling in a GaP(110) crystal [108; 23], are presented in Figure 6.3. The recovery of an HD-TKE signal in tetrahydrofuran (THF) demonstrates the significant sensitivity improvements that result from heterodyne detection. Hoffmann et al. were

unable to record a signal from THF with five times the path length and posited that strong THz absorbers may not be suitable for TKE measurements [106]. Our data show a clear TKE response from THF. The pre-pulse from -2 $\rightarrow$ 0 ps is the TKE signature of the quartz sample cuvette. It is present in all of the data in Fig. 6.3, and provides a reference for the relative molecular responses.

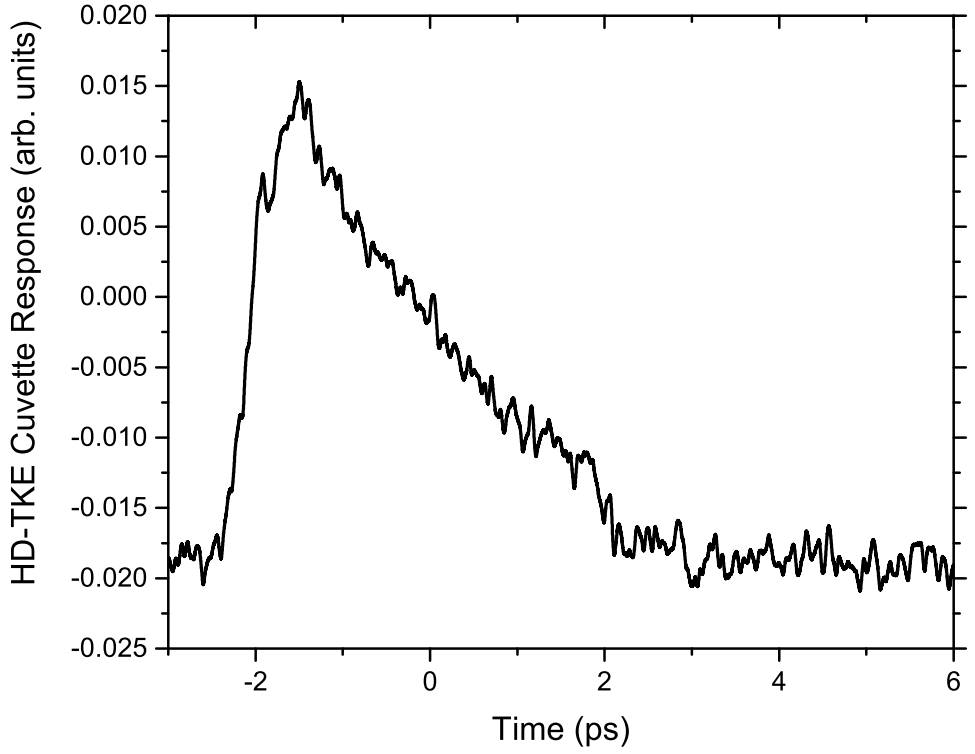

Figure 6.4: The measured HD-TKE response of the empty sample cuvette. The time axis is set for time zero as defined by the peak response of the molecular signals.

The measured HD-TKE response of the empty cuvette can be seen in Fig. 6.4. The response appears as a pre-pusle $\sim$2 ps before the molecular response because of the differences in refractive index of quartz between THz and optical frequencies. It is also weak compared to systems such as diiodomethane and carbon disulfide; however, it is quite similar in size to the magnitude of the tetrahydrofuran signal. The cuvette signal lasts for just over 4 ps. As a result the molecular signal of THF does contain some non-trivial contribution from the cuvette. However, the cuvette signal is so weak relative to the other molecular systems studied that it does not affect the results.

Indeed, the cuvette response can be subtracted from the THF data to yield the trace shown in Fig. 6.5. The subtraction procedure requires boxcaring the cuvette data so that it becomes less noisy that the molecular data to be processed. Then simply set the peak of the cuvette response to the peak of the pre-pulse in the molecular data and subtract the cuvette response from the molecular data. This general procedure will allow for the removal of the cuvette response from weak signals such as water, or other strongly absorbing samples where the magnitude of the cuvette response approaches the magnitude of the molecular signal.

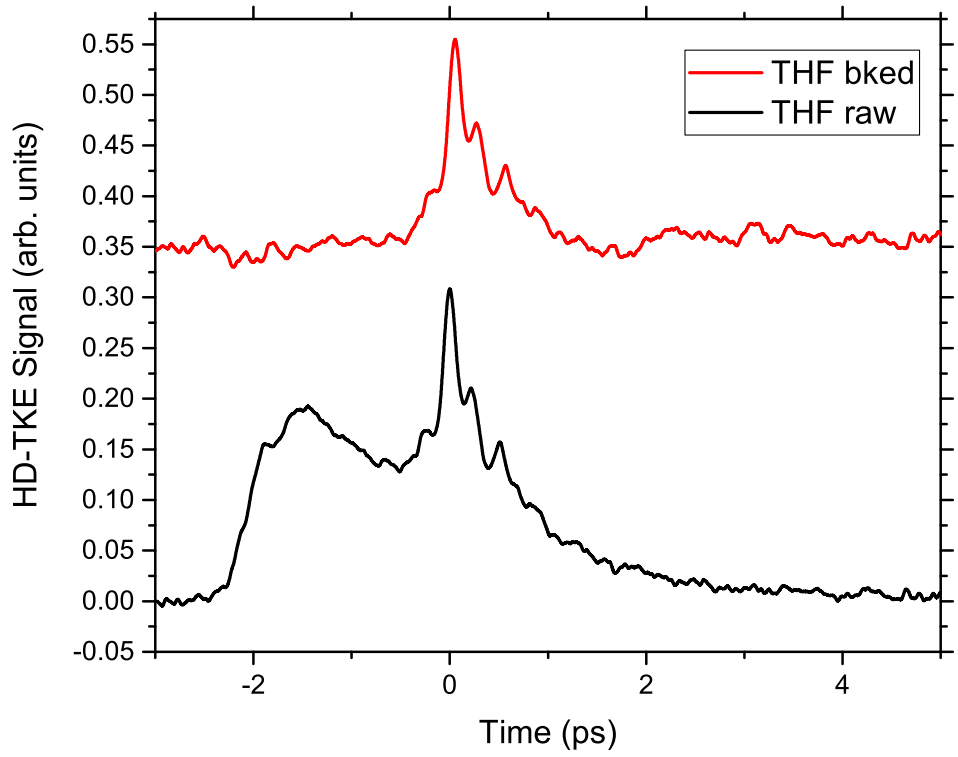

Figure 6.5: The HD-TKE THF trace corrected for the response of the empty sample cuvette. The uncorrected THF data are plotted in black.

The measured HD-TKE response has a delta-function-like signal centered around zero time that corresponds to the electronic response of the molecules and contains no information about the nuclear dynamics [109]. This can be clearly seen in the signal measured in carbon tetrachloride (CCl_4). Given that CCl_4 is part of the T_d point group, it has a roughly spherically-symmetric

electron distribution, and we expect no significant reorientational response [110]. It can thus be thought of as an instrument-response function for the electronic contribution to the signal. The multi-cycle nature of E^2_{THz} results in the staggered nature of the measured CCl_4 response.

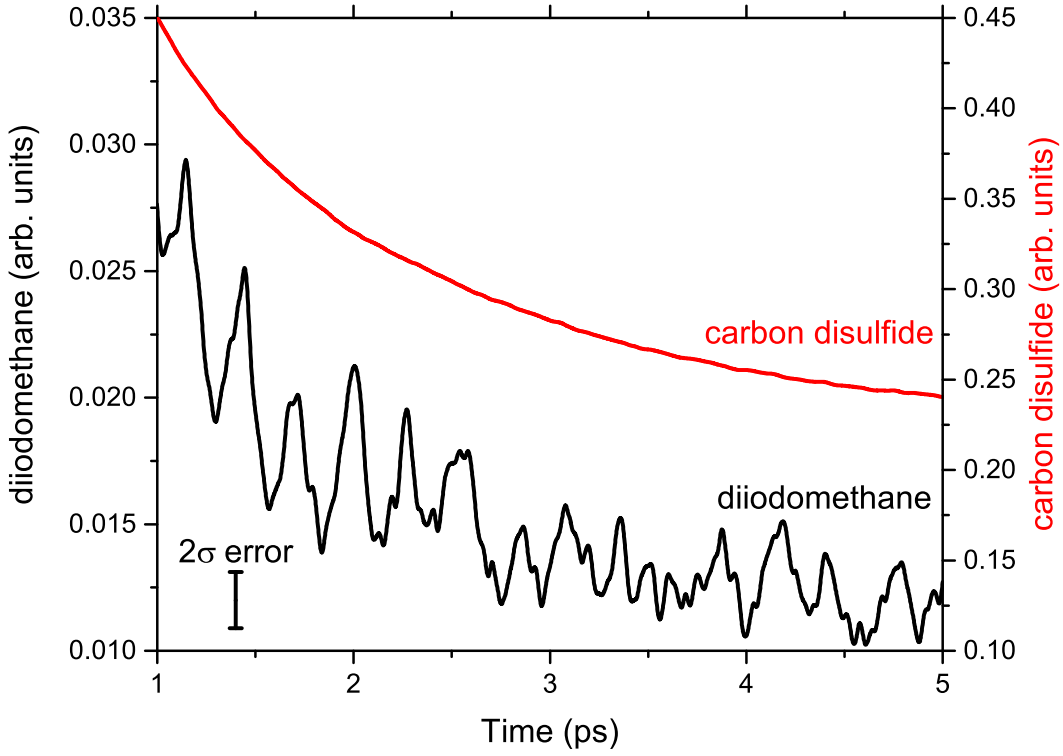

Figure 6.6: Vibrational quantum beats in diiodomethane. Carbon disulfide is plotted for reference. A two-sigma error bar is plotted for CH_2I_2, and the error bar for CS_2 would be contained within the plotted line on this scale. Reproduced from Allodi et al. "Vibrational Quantum Beats in Pure Liquids Measured with Ultrafast TeraHertz Kerr Effect Spectroscopy" *Physical Review Letters, submitted.*

The nuclear part of the HD-TKE signal remains zero until time zero and contains all of the potentially retrievable information about the molecular dynamics of the liquid under study. It is well established in the literature that rotational diffusion of individual molecules returning to an isotropic distribution of molecular orientations is the dominant contribution to the OKE and TKE signals starting several picoseconds after the peak, and that this response can be fit with a decaying exponential. Such behavior is clearly visible in the carbon disulfide (CS_2) HD-TKE data. While

the $D_{\infty h}$ point group molecular symmetry of CS_2 dictates that it does not have a net molecular dipole moment, its large molecular polarizability leads to a large electronic response followed by an orientational response that quickly dominates the signal.

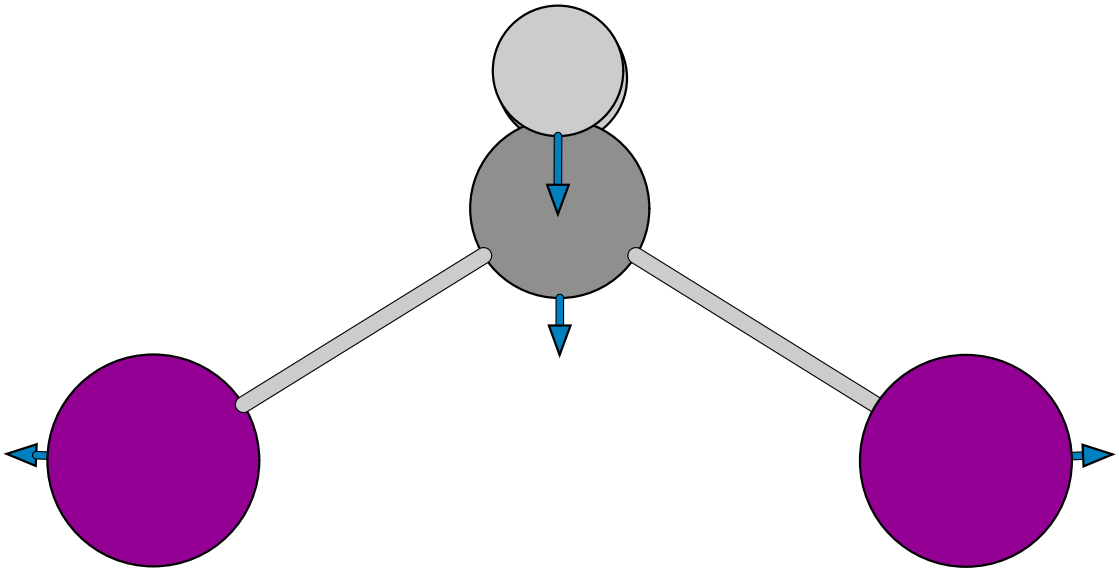

Figure 6.7: The ν_4 vibrational mode of diiodomethane centered at 3.66 THz (122 cm^{-1}). The mode was calculated using MP2/3-21G and the vectors on the atoms represent the displacement of the atoms during the vibration.

Diiodomethane (CH_2I_2) differs fundamentally from a molecule such as CS_2. As a part of the C_{2v} point group, the symmetry of CH_2I_2 results in a net molecular dipole. This dipole moment coupled with the large size of the iodine atoms relative to sulfur leads to a large moment of inertia, which produces a reorientational response that decays on a much longer timescale than that of CS_2. In addition, the nature of the chemical bonds in CH_2I_2 leads to a fundamental vibrational mode of the molecule, ν_4, at 3.66 THz (122 cm^{-1}) [111], which is within the frequency window covered by our DSTMS-generated THz pulse. The high-THz-field-strength and frequency content is able to excite a vibrational coherence in CH_2I_2 that lasts for several ps, clearly visible as quantum beats in Figure 6.6 that are read-out using the 800 nm probe. The motion of the atoms in this vibrational mode of CH_2I_2 can be seen in Fig. 6.7.

We confirm that the quantum beats correspond to the ν_4 mode of CH_2I_2 by taking a numerical Fourier transform of the data starting at time zero and using an asymmetric Hann window for

apodization [107; 32]. The imaginary component of the Fourier transform contains information only about the nuclear response of the liquid [28; 109], and the results are plotted in Figure 6.8.

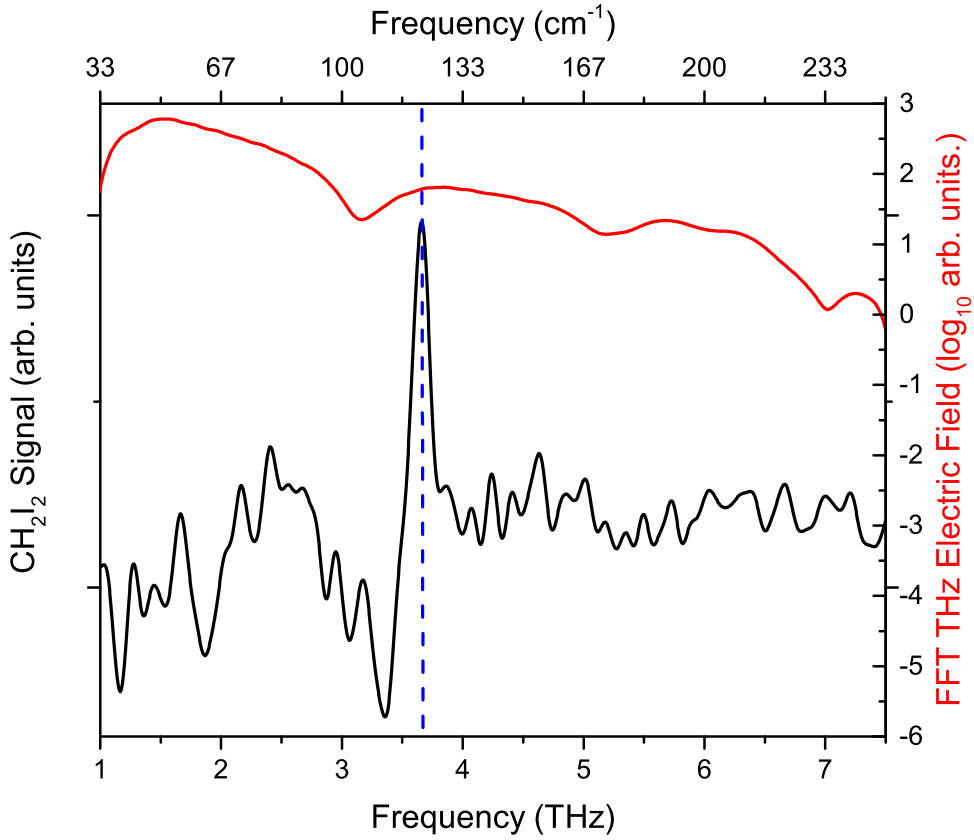

Figure 6.8: The imaginary component of the numerical Fourier transform of the diiodomethane data. The dashed, blue line is the experimentally-measured line center of the ν_4 vibrational mode of diiodomethane at 3.66 THz (122 cm^{-1}). The red trace at the top of the figure shows the frequency content of the THz pulse used in these experiments. Reproduced from Allodi et al. "Vibrational Quantum Beats in Pure Liquids Measured with Ultrafast TeraHertz Kerr Effect Spectroscopy" *Physical Review Letters, submitted.*

The quantum beats in diiodomethane are the first vibrational coherences measured that result from the nonlinear interaction of THz radiation (E^2_{THz}) in a condensed-phase molecular system. The implications of this result are manyfold. For nonlinear THz spectroscopy to mature into a field capable of robustly probing the dynamics of molecular systems on ultrafast timescales, it must be capable of manipulating and detecting vibrational coherences in a variety of systems. The results from CH_2I_2 are particularly encouraging because the ν_4 vibrational mode is a weak IR transition in the liquid [111]. Thus, weak intermolecular transitions in other liquids should be accessible, and

our measurement of quantum beats in CH_2I_2 establishes that TKE spectroscopy can be used as the cornerstone for the design of nonlinear THz measurements capable of gaining new insight into the ultrafast dynamics in molecular liquids.

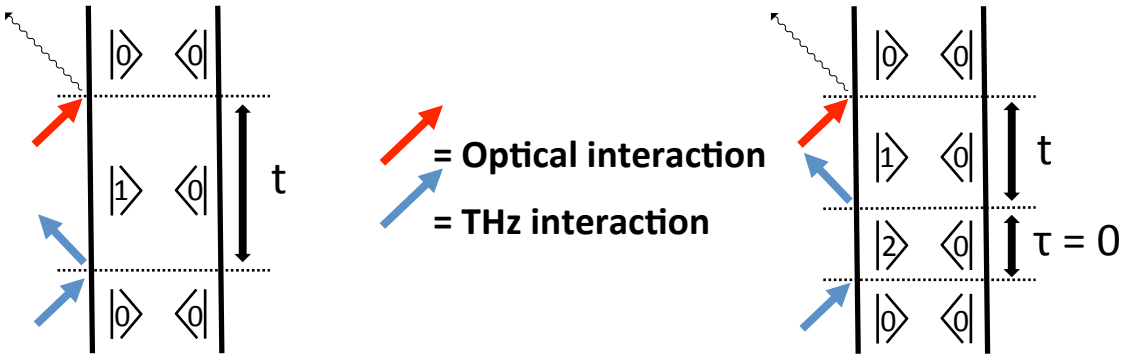

Figure 6.9: Feynman diagrams that contain a 3.66 THz vibrational beat in diiodomethane. The numbers in the bras and kets represent the number of vibrational quanta. Note that in this experiment the time spacing between the two THz field interactions, τ, is zero since they both come from the same THz pulse. Reproduced from Allodi et al. "Vibrational Quantum Beats in Pure Liquids Measured with Ultrafast TeraHertz Kerr Effect Spectroscopy" *Physical Review Letters, submitted.*

For example, these results may offer some insight into the dipolar and/or Raman selection rules of THz-active modes. The constraints imposed by the sample and apparatus ensure that the HD-TKE response is a $\chi^{(3)}$ process that measures a backgroundless transient birefringence. Two possible pathways on the intramolecular vibrational manifold that generate a coherence at 3.66 THz in CH_2I_2 are shown as Feynman diagrams in Figure 6.9. That at left depicts a Raman scattering process for the THz interaction. Such a transition, involving excitation of the soft bath modes of the liquid, could contribute to the 3.66 THz signal. The availability of numerous intermolecular and orientational degrees-of-freedom at THz frequencies provide states for the system to be excited into before a second THz interaction returns the system to a 1-0 coherence generated by the inelastic Raman process. Indeed, the fact that polarizability changes dominate the initial rise of the HD-TKE signal suggests that Raman processes could govern the interaction at THz frequencies.

The right diagram represents a path via a two-quantum transition to an overtone of the ν_4 mode. The constraint that results from the optical probe pulse demands that if we treat each

THz interaction as dipolar, as opposed to Raman, in nature, then a perturbative model of the third-order process must include a two-quantum transition to generate a 1-0 coherence. This is not without precedent in the literature. Two-quantum transitions form the basis of 2D-Raman-THz spectroscopy [99]. Hamm & Savolainen further argue that, at THz frequencies, both mode and dipolar anharmonicity cannot be treated as a small perturbation. Thus, the shape of the vibrational potential may make overtone transitions more allowed [10]. If these transitions are allowed, the >7 THz spectral coverage of pulses used in this experiment could drive a two-quantum transition.

In summary, we have measured long-lived quantum beats that result from vibrational coherences initiated by a nonlinear terahertz interaction with a molecular liquid. Heterodyne detection has greatly improved the sensitivity and dynamic range of TKE spectroscopy, as evidenced by our measurement of an HD-TKE signature from THF. The 3.66 THz quantum beats recorded from diiodomethane show both the importance of the heterodyne detection coupled with a broadband THz source, as well as the promise of this technique for understanding the room-temperature dynamics of the condensed phase.

In a liquid such as diiodomethane, THz frequency modes are thermally populated, and it is precisely these modes that determine the molecular dynamics. The anharmonicities of the modes may be so great that they can no longer be treated perturbatively, especially if interactions with the near-resonant intermolecular degrees of freedom are strong. As such, they are distinct from modes in the mid- or near-IR, and our results may help us understand Raman-active THz transitions, as well as the importance of two-quantum vibrational transitions in THz spectroscopy. Thus, these HD-TKE results offer the first glimpse into unexplored realms of condensed-phase dynamics provided by THz radiation.

Part V

Conclusions and Future Directions

Chapter 7

In Conclusion

The work discussed in the above chapters lays the groundwork for much exciting science. The development of the astrochemical ice spectrometer has produced robust instrumentation capable of tackling a variety of astrochemical challenges. The instrument has now been sufficiently refined such that high signal-to-noise data over almost a century of bandwidth can be collected in a few seconds with a $\sim$0.5 cm^{-1} resolution. This has unleashed the creativity of the group and several manuscripts are in preparation that contain studies made possible by the instrumentation developed in this thesis.

The use of THz Kerr effect spectroscopy to perform nonlinear THz measurements of molecular systems has great potential. The implementation of heterodyne detection improved the sensitivity of the technique and allowed for the detection of long-lived vibrational coherences. The coherences persist for several picoseconds and may be observable for even longer with further improvements to the signal-to-noise ratio of the measurement. Table-top sources of pulsed THz radiation will only continue to improve, thus providing higher-field-strength THz pulses and improving the signal-to-noise ratio of the data collected.

Even without the implementation of a yet-to-be-developed THz source, there are several directions that would be interesting to pursue. The fact that the vibrational coherences detected in diiodomethane last for at least 5 ps provides an ideal situation for a two-THz-pulse HD-TKE experiment, where a coherence is initiated with one THz pulse and subsequently perturbed with another THz pulse, resulting in a 2D TKE spectroscopy analogous to 2D IR or 2D Raman[112] spectroscopy.

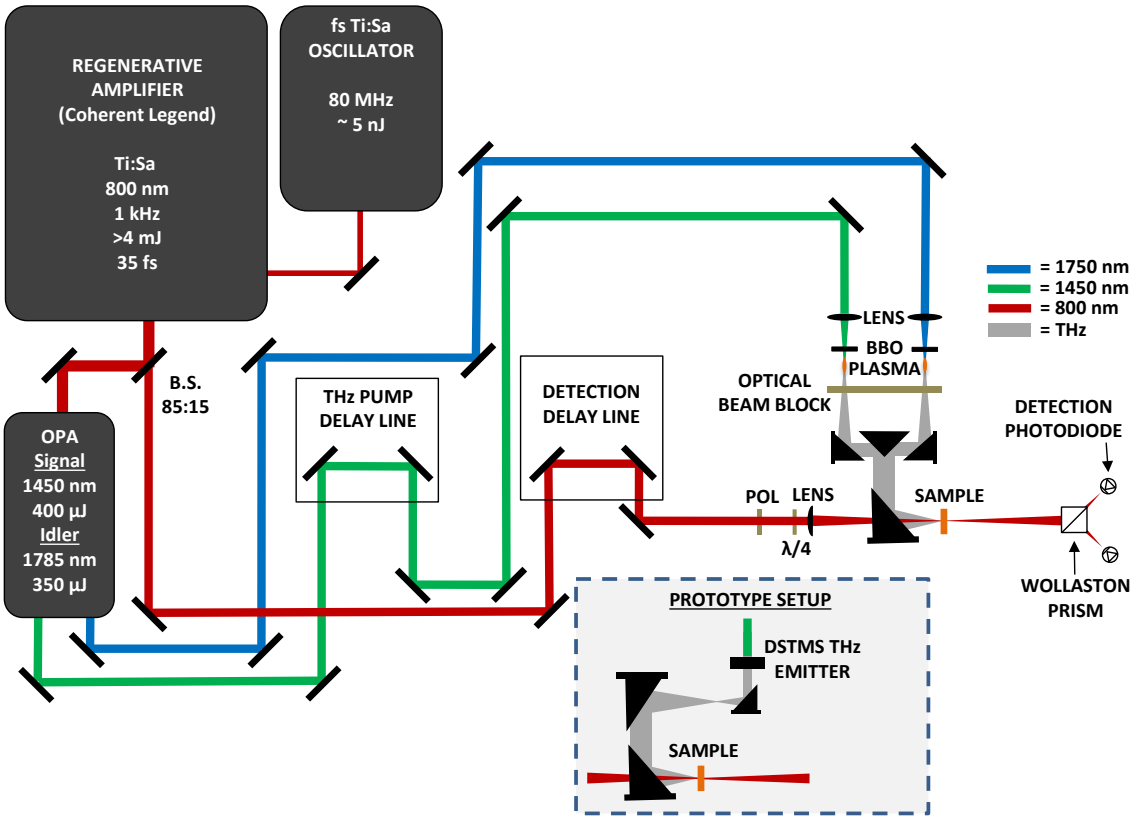

Figure 7.1: Schematic representation of a two-plasma-source HD-TKE spectrometer.

As discussed above, the introduction of a second THz pulse would allow for the measurement of a COSY spectrum. In the case of diiodomethane, where only one feature appears present in the THz region, the modulation of this feature might allow us to learn about its coupling to the bath. Also, it is possible that certain bath degrees of freedom might become more specifically populated and appear as cross peaks in the spectrum, especially if they correspond more directly to intermolecular modes. In any case, the implementation of a second source of THz pulses with a controllable arrival time at the sample would turn HD-TKE spectroscopy into 2D HD-TKE spectroscopy.

To develop a robust 2D TKE spectroscopy, temporal resolution may present a challenge. The multi-cycle nature of the pulses used in the current experimental setup would fundamentally limit the temporal resolution that could be achieved with 2D TKE spectroscopy to ∼1 ps. However, switching to a plasma-based gas photonic THz source would yield sub-cycle THz pulses, thus opening the possibility of <100 fs resolution in nonlinear THz measurements. [18; 17; 19] An example of how

this could be achieved with the tools available in the Blake group can be seen in Figure 7.1. Such temporal resolution is almost certainly required to understand the anharmonicity of low-frequency intra- and intermolecular vibrations and would provide novel data to investigate how the molecular dynamics on ultrafast timescales affects the physical properties of liquids.

The final hurdle remaining to achieve sub-100 fs resolution with HD-TKE spectroscopy will be controlling the shape of the THz electric field. The ideal pulse shape for maximum temporal resolution would be a delta function. However, given physical restrictions, ultrafast scientists generally compromise on something resembling a Gaussian or sech^2 pulse shape. The most important characteristics of these two shapes is that they go smoothly from their peak to zero without dipping below. As such, we can imagine the physical response of a material will only be pushed in one direction toward some maximum response sometime after the peak of the pulse. If the applied pulse has components both above and below zero, the material response will start to go one way and then have to switch directions. Starting in the mid-IR and above, the rotating-wave approximation ensures that response is dictated by the pulse envelope as opposed to the underlying electric field of the pulse. In the THz, this approximation breaks down, and the shape of the electric field determines the material response.

Both the promise and the challenge of plasma pulses can be seen in Figure 7.2. The black trace in Figure 7.2 was generated by a 1.45 μm plasma and has a $\sim$300 fs FWHM. The pulse is likely even shorter since phase matching in the detection crystal limits the detection bandwidth. However, it also has to lobes that dip below zero. Even for TKE spectroscopy, where the electric field squared determines the material response, those lobes will contribute to the signal along with the main pulse. We see this in the CCl_4 response to the multi-cycle DSTMS pulse shown in Figure 6.3.

The real promise of plasma pulses comes from the possibility of THz pulse shaping as seen in the difference between the two traces plotted in Figure 7.2. Both traces are generated by a plasma that contains both 1.45 μm and its second harmonic. However, in the black trace, the BBO crystal that generates the second harmonic is $\sim$1 inch from the plasma. In the red trace, the crystal is $>$3 inches from the plasma. Since the dispersion in both air and BBO is different at 1450 nm and

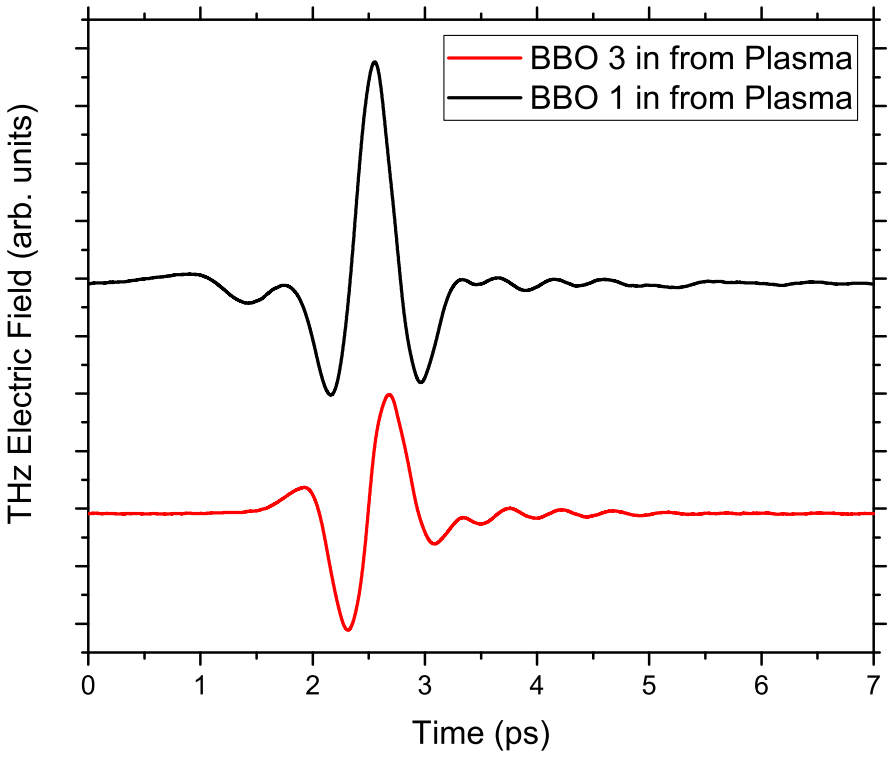

Figure 7.2: Two different THz electric fields generated with 1.45 μm plasmas. The BBO was 3" away in the bottom trace and 1" away in the top trace. The phase between the fundamental and the second harmonic can be controlled by adjusting the distance of the BBO from the emitting plasma, thus changing the shape of the THz electric field. This is a crude example of THz pulse shaping.

725 nm, moving the position of the BBO will change the relative phase of the electric field between the two beams. This phase, represented as θ in Equation 2.1, will certainly affect the nature of the symmetry-broken laser field that generates the THz pulses in the plasma.[16]

Thus, precise control of the phase θ may provide the necessary experimental handle to sufficiently shape the electric field of THz pulses to the required shape for nonlinear THz spectroscopy. As a first attempt at THz pulse shaping, one could imagine employing a setup similar to the one previously used in our group with an 800/400 nm plasma.[8] First, we could frequency double the beam with BBO before focusing. Next, we can pass both colors through a birefringent material to correct for the differences in dispersion between the two colors. Then, a dual-band waveplate could be used

to properly align the polarizations of the electric fields. This step will increase the efficiency of the plasma generation mechanism. The key step for pulse shaping will be to use a pair of thin wedges that will add a small amount of dispersion. By moving the wedges in and out of the beam, thus adding or removing relative dispersion, it will be possible to control the relative phase and shape the THz pulse.

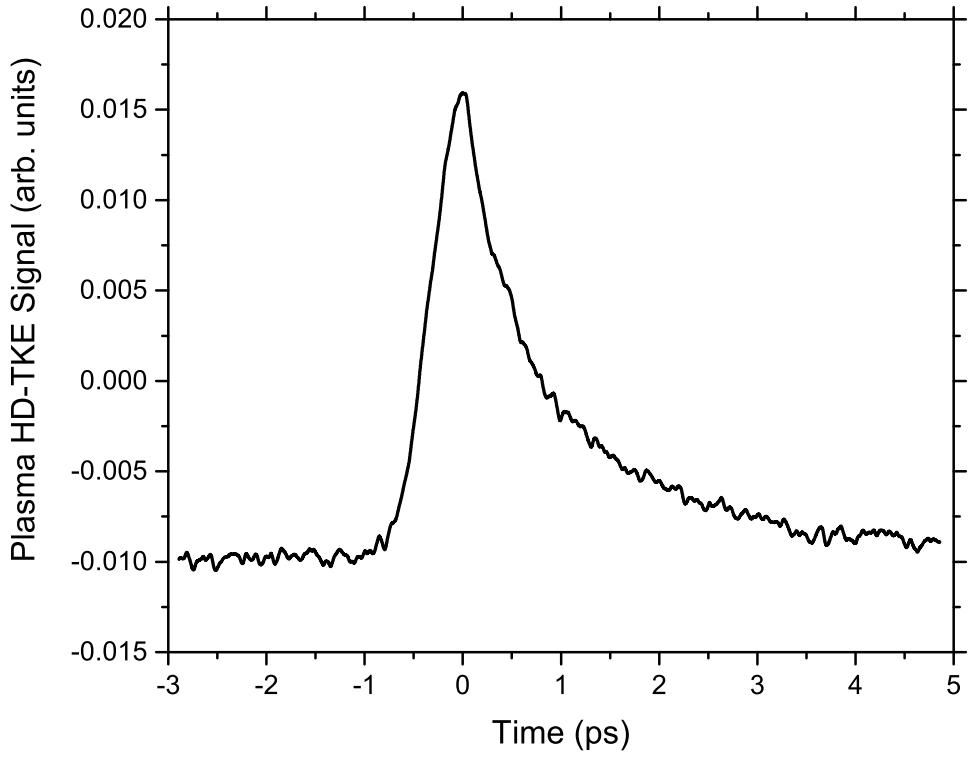

Figure 7.3: HD-TKE response of CS_2 using a plasma pulse as the THz source.

The results from the proof-of-concept experiment for a plasma based TKE spectrometer can be seen in Figure 7.3. This is the first experimental realization of plasma-based nonlinear THz spectroscopy. The experimental setup is similar to that proposed in Figure 7.1, albeit with only one plasma generated using the 1.4 μm beam. The data in Figure 7.3 were collected on CS_2, which has the strongest TKE signal of all the molecules we've measured. Note that the shape of the response looks similar to that of CS_2 shown in Figure 6.3. The signal is weaker than in DSTMS based TKE

spectroscopy; however, our plasma TKE spectrometer remains far from optimized. In addition, the signal was measured in the same quartz cuvette used in the TKE work discussed above. As a result, the high-frequency content above 7.5 THz was attenuated, resulting in a loss of THz power in the pulse. Thus, optimizing a sample holder, or making a gravity-driven liquid jet so that a sample holder is not necessary, will boost both signal and time resolution.

Another potentially significant improvement to the instrumentation for TKE measurements within the capabilities of the Blake group will be a single-shot detection scheme. It has been shown in the literature that a reflective echelon mirror can be used in combination with a CCD camera to measure the electric field of a THz waveform in a single laser shot.[113] The echelon is a precisely machined mirror with steps analogous to a staircase and replaces the delay line. When an 800 nm detection pulse bounces off the surface of the echelon, the stepped structure of the echelon means that different parts of the pulse are delayed by different amounts. This pulse can then be sent through a detector crystal and imaged on a CCD array. The change in polarization of the 800 nm beam that results from interaction of this 800 nm pulse with the THz pulse in the detector crystal can now be measured on the CCD array. The size of the machined steps on the echelon determines coarseness of the time-domain EO sampling measurement.

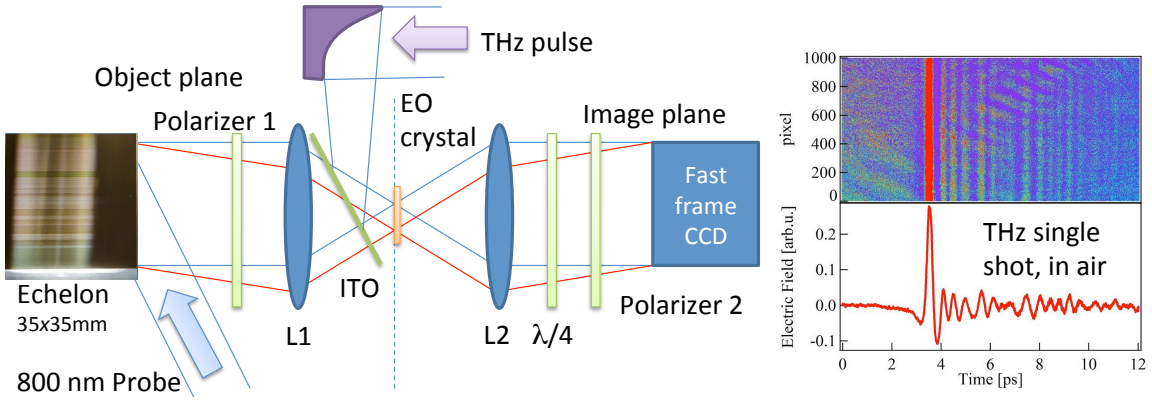

Figure 7.4: The proposed multi-channel THz electro-optic detection system. The Ni echelon pictured was generously donated by the Ikufumi group in Yokohama. Adapted, with permission, from figures and approaches described in reference [113]. The THz time-domain trace at right is from a single shot, in air; data provided by K. Ikufumi [priv. commun.].

A possible experimental implementation of this technique can be seen in Figure 7.4. The advantages of a single-shot detection scheme are numerous. The current THz instrumentation, both for linear and nonlinear measurements, suffers pulse-to-pulse fluctuations that can be quite large. Since we often need to collect data over several hours, this can lead to significant noise. It also presents a challenge to undertake quantitative spectroscopic measurements (e.g. absorption coefficients of a band) as opposed to relative absorption measurements. These issues could be corrected in post-processing of the data if we acquire a THz spectrum with every laser shot. More importantly, single-shot detection has been shown repeatedly to create opportunities for new experiments that were not possible without this new technique.[114; 115] Especially important for nonlinear THz spectroscopy, single-shot detection will ultimately be necessary to collect a 2D THz spectrum in several hours or a day, as opposed to weeks.

The group is prepared to attempt this experimental design. We have an echelon in hand (thanks to the extreme generosity of Profs. Takeda and Ikufumi of Yokohama National University, Japan) from the Japanese company Sodik-FT, that covers 36 ps of delay. As funds become available, we hope to acquire a sufficiently fast camera to image the 800 nm beam. Even before funds become available, it is possible to prototype an experimental setup since sufficiently fast cameras may be borrowed from another group on campus a camera loan could be secured from a vendor. Then all that is necessary is the determination of some young, bright student in the Blake group!

There are many, many experiments that would be exciting to pursue with the new instrumentation discussed above. The molecule closest to the heart of most chemists (and probably all physical chemists) is water. As discussed in Chapter 1, groups around the world continue to show that water still contains surprises for us. A 2D THz spectroscopy that was nonlinear in THz field would provide a complementary tool to the 2D Raman-THz work already in the literature [99] by perturbing the THz modes directly with THz radiation and observing the echoes that appear. In addition, the broadband nature of the plasma pulses might allow for the measurement of the dynamics of the 600 cm^{-1} feature that was too fast to be measured in the current implementation of 2D Raman-THz.

Given the potential of nonlinear THz spectroscopy, it would be interesting to investigate how the harmonic-oscillator approximation breaks down for THz active modes. The results in the previous chapter provide evidence that the selection rules that govern vibrational spectroscopy do not rigorously hold. If two-quantum transitions are necessary to observe the beating seen in the HD-TKE data for diiodomethane, it will be important to understand what selection rules *actually govern* THz-active modes. A set of experiments should be possible with a 2D HD-TKE spectrometer to better understand these selection rules. By using two separate THz field interactions from two pulses, it should be possible to move coherences around in such a way that we come to understand the nature of the allowed transitions at THz frequencies.

In addition, nonlinear THz spectroscopy could enable new insight into the chemistry of solvation and charge transfer. The Havenith group has shown the extent to which THz spectroscopy is sensitive to the biological water solvating a protein.[116; 117; 118; 119; 120] In general, the challenge of investigating water-based samples with THz spectroscopy stems from the large absorption coefficients ($>$100 cm^{-1}) for water at THz frequencies. This leads to an attenuation factor of $\sim$10^{-9} for a 1 mm pathlength of water. While THz photons must still reach a molecule to generate a TKE signal, our nonlinear HD-TKE spectroscopy can potentially lead to high signal-to-noise data by detecting 800 nm rather than THz photons. Since water is much more transmissive at 800 nm, we can still measure the effects of THz pulses on our samples. Finally, we have shown with our HD-TKE measurements of THF that we have the dynamic range to detect TKE signals from molecules that strongly absorb in the THz. Thus, it should now be possible to perform spectroscopy on water and subsequently on proteins dissolved in water.

The THz region of the electromagnetic spectrum is full of opportunities for chemists. As the last frontier in the spectrum, any intrepid explorer will find a multitude of challenges as well as surprises. This work endeavored to expand the frontier in both astrochemistry and solvation science. In both cases, we were required to develop new instrumentation to boldly go where our questions led us. These techniques will hopefully remain a part of the group's core competencies and serve as building blocks for the next generation of THz instrumentation.

With these tools in hand, we were able to explore some interesting scientific questions. Our investigations into astrochemical ice analogs have explored the relationship between the structure of an ice and its spectrum, thus providing a tool to understand the dynamics of these important chemical factories in the interstellar medium. Our development of heterodyne-detected THz Kerr effect spectroscopy allowed us to measure the first vibrational coherences, or quantum beats, initiated by nonlinear THz interactions with a sample. This result definitively shows that nonlinear THz spectroscopy will be able to provide insight into the dynamics of molecular systems. While seemingly disparate, these results were both motivated by a desire to understand the interactions of molecules in the condensed phase. The THz region provides an excellent window into these interactions and the group is now poised to create new knowledge that will advance both chemistry and the scientific enterprise as a whole.

Bibliography

[1] E. Herbst and E. F. van Dishoeck, "Complex Organic Interstellar Molecules," *Annu. Rev. Astron. Astrophys.*, **47**, 427–480 (2009).

[2] C. H. Langmuir and W. Broecker, *How to Build a Habitable Planet: The Story of Earth from the Big Bang to Humankind*, Princeton University Press (2012).

[3] R. Chang, *Chemistry, 8th ed.*, McGraw Hill (2005).

[4] J. Roberts, *ABCs of FT-NMR*, University Science Books (2000).

[5] O. H. Seeck and B. M. Murphy, *X-Ray Diffraction: Modern Experimental Techniques*, CRC Press (2014).

[6] X. Zhang and J. Xu, *Introduction to THz Wave Photonics*, Springer (2010).

[7] A. Tielens, *The Physics and Chemistry of the Interstellar Medium*, Cambridge University Press (2005).

[8] M. A. Allodi, S. Ioppolo, M. J. Kelley, B. A. McGuire, and G. A. Blake, "The structure and dynamics of carbon dioxide and water containing ices investigated via THz and mid-IR spectroscopy," *Phys. Chem. Chem. Phys.*, **16**, 3442–3455 (2014).

[9] K. Ramasesha, L. De Marco, A. Mandal, and A. Tokmakoff, "Water vibrations have strongly mixed intra- and intermolecular character," *Nat. Chem.*, **5**, 935–940 (2013).

[10] P. Hamm and J. Savolainen, "Two-dimensional-Raman-terahertz spectroscopy of water: Theory," *J. Chem. Phys.*, **136**, 094516 (2012).

[11] J. E. Elsila, D. P. Glavin, and J. P. Dworkin, "Cometary glycine detected in samples returned by Stardust," *Meteorit. Planet. Sci.*, **44**, 1323–1330 (2009).

[12] R. L. Pulliam, B. A. McGuire, and A. J. Remijan, "A Search for Hydroxylamine (NH2OH) toward Select Astronomical Sources," *Astrophys. J.*, **751**, 1 (2012).

[13] S. Ioppolo, H. M. Cuppen, C. Romanzin, E. F. van Dishoeck, and H. Linnartz, "Laboratory Evidence for Efficient Water Formation in Interstellar Ices," *Astrophys. J.*, **686**, 1474 (2008).

[14] G. W. Fuchs, H. M. Cuppen, S. Ioppolo, C. Romanzin, S. E. Bisschop et al., "Hydrogenation reactions in interstellar CO ice analogues A combined experimental/theoretical approach," *Astron. Astrophys.*, **505**, 629–639 (2009).

[15] D. Cook and R. Hochstrasser, "Intense terahertz pulses by four-wave rectification in air," *Opt. Lett.*, **25**, 1210–1212 (2000).

[16] X. Xie, J. Dai, and X.-C. Zhang, "Coherent Control of THz Wave Generation in Ambient Air," *Phys. Rev. Lett.*, **96**, 075005 (2006).

[17] K.-Y. Kim, J. H. Glownia, A. J. Taylor, and G. Rodriguez, "Terahertz emission from ultrafast ionizing air in symmetry-broken laser fields," *Opt. Express*, **15**, 4577–4584 (2007).

[18] K. Y. Kim, A. J. Taylor, J. H. Glownia, and G. Rodriguez, "Coherent control of terahertz supercontinuum generation in ultrafast laser-gas interactions," *Nature Photon.*, **2**, 605–609 (2008).

[19] M. Clerici, M. Peccianti, B. E. Schmidt, L. Caspani, M. Shalaby et al., "Wavelength Scaling of Terahertz Generation by Gas Ionization," *Phys. Rev. Lett.*, **110**, 253901 (2013).

[20] C. Vicario, C. Ruchert, and C. Hauri, "High field broadband THz generation in organic materials," *J. Mod. Opt.*, **1**, 1–6 (2013).

[21] D. Auston, A. Johnson, P. Smith, and J. Bean, "Picosecond optoelectronic detection, sampling, and correlation-measurements in amorphous-semiconductors," *Appl. Phys. Lett.*, **37**, 371–373 (1980).

[22] Q. Wu and X. Zhang, "Free-space electrooptic sampling of terahertz beams," *Appl. Phys. Lett.*, **67**, 3523–3525 (1995).

[23] Z. G. Lu, P. Campbll, and X.-C. Zhang, "Free-space electro-optic sampling with a high-repetition-rate regenerative amplified laser," *Appl. Phys. Lett.*, **71**, 593–595 (1997).

[24] F. D. J. Brunner, J. A. Johnson, S. Grübel, A. Ferrer, S. L. Johnson et al., "Distortion-free enhancement of terahertz signals measured by electro-optic sampling. I. Theory," *J. Opt. Soc. Am. B*, **31**, 904–910 (2014).

[25] J. A. Johnson, F. D. J. Brunner, S. Grübel, A. Ferrer, S. L. Johnson et al., "Distortion-free enhancement of terahertz signals measured by electro-optic sampling. II. Experiment," *J. Opt. Soc. Am. B*, **31**, 1035–1040 (2014).

[26] R. W. Boyd, *Nonlinear Optics, 3rd Ed.*, Academic Press (2008).

[27] M. Shalaby and C. P. Hauri, "Demonstration of a low-frequency three-dimensional terahertz bullet with extreme brightness," *Nat. Commun.*, **6**, 5976 (2015), doi:{10.1038/ncomms6976}.

[28] D. McMorrow and W. T. Lotshaw, "Intermolecular dynamics in acetonitrile probed with femtosecond Fourier-transform Raman spectroscopy," *J. Phys. Chem.*, **95**, 10395–10406 (1991).

[29] S. Mukamel, *Principles of Nonlinear Optical Spectroscopy*, Oxford University Press (1995).

[30] J. Dai, X. Xie, and X.-C. Zhang, "Detection of Broadband Terahertz Waves with a Laser-Induced Plasma in Gases," *Phys. Rev. Lett.*, **97**, 103903 (2006).

[31] P. R. Griffiths and J. A. de Haseth, *Fourier Transform Infrared Spectroscopy, 2^{nd} ed.*, Wiley (2007).

[32] R. K. H. Galvao, S. Hadjiloucas, A. Zafiropoulos, G. C. Walker, J. W. Bowen et al., "Optimization of apodization functions in terahertz transient spectrometry," *Opt. Lett.*, **32**, 3008–3010 (2007).

[33] R. B. Blackman and J. W. Tukey, *The Measurement of Power Spectra, From the Point of View of Communications Engineering*, Dover (1959).

[34] J. O. Smith, *Mathematics of the Discrete Fourier Transform (DFT), with Audio Applications, 2^{nd} ed.*, W3K Publishing (2007).

[35] R. Gould and E. Salpeter, "Interstellar abundance of hydrogen molecule .1. Basic processes," *Astrophys. J.*, **138**, 393–407 (1963).

[36] R. Gould, E. Salpeter, and T. Gold, "Interstellar abundance of hydrogen molecule .2. Galactic abundance and distribution," *Astrophys. J.*, **138**, 408 (1963).

[37] S. Cazaux and A. G. G. M. Tielens, "H_2 Formation on Grain Surfaces," *Astrophys. J.*, **604**, 222 (2004).

[38] H. B. Perets, O. Biham, G. Manic, V. Pirronello, J. Roser et al., "Molecular Hydrogen Formation on Ice Under Interstellar Conditions," *Astrophys. J.*, **627**, 850 (2005).

[39] L. Allamandola, M. Bernstein, S. Sandford, and R. Walker, "Evolution of interstellar ices," *Space Sci. Rev.*, **90**, 219–232 (1999).

[40] E. F. van Dishoeck, "Chemistry in low-mass protostellar and protoplanetary regions," *Proc. Natl. Acad. Sci.*, **103**, 12249–12256 (2006).

[41] L. Allamandola, S. Sanford, and G. Valero, "Photochemical and thermal evolution of interstellar precometary ice analogs," *Icarus*, **76**, 225–252 (1988).

[42] M. H. Moore and R. L. Hudson, "IR Detection of H_2O_2 at 80 K in Ion-Irradiated Laboratory Ices Relevant to Europa," *Icarus*, **145**, 282–288 (2000).

[43] R. Hudson and M. Moore, "IR Spectra of Irradiated Cometary Ice Analogues Containing Methanol: A New Assignment, a Reassignment, and a Nonassignment," *Icarus*, **145**, 661 – 663 (2000).

[44] G. Strazzulla, G. Baratta, and M. Palumbo, "Vibrational spectroscopy of ion-irradiated ices," *Spectrochim. Acta Mol. Biomol. Spectros.*, **57**, 825 – 842 (2001).

[45] S. Ioppolo, M. E. Palumbo, G. A. Baratta, and V. Mennella, "Formation of interstellar solid CO_2 after energetic processing of icy grain mantles," *Astron. Astrophys.*, **493**, 1017–1028 (2009).

[46] U. Raut, D. Fulvio, M. J. Loeffler, and R. A. Baragiola, "Radiation synthesis of carbon dioxide in ice-coated carbon: implications for interstellar grains and icy moons," *Astrophys. J.*, **752**, 159 (2012).

[47] J. A. Noble, F. Dulieu, E. Congiu, and H. J. Fraser, "CO_2 Formation in Quiescent Clouds: An Experimental Study of the CO + OH Pathway," *Astrophys. J.*, **735**, 121 (2011).

[48] Theule, P., Duvernay, F., Ilmane, A., Hasegawa, T., Morata, O. et al., "Kinetics of the OCN- and HOCN formation from the HNCO + H2O thermal reaction in interstellar ice analogs," *Astron. Astrophys.*, **530**, A96 (2011).

[49] J. A. Noble, P. Theule, F. Borget, G. Danger, M. Chomat et al., "The thermal reactivity of HCN and NH_3 in interstellar ice analogues," *Mon. Not. R. Astron. Soc.*, **428**, 3262–3273 (2013).

[50] N. Watanabe and A. Kouchi, "Efficient Formation of Formaldehyde and Methanol by the Addition of Hydrogen Atoms to CO in H2O-CO Ice at 10 K," *Astrophys. J. Lett.*, **571**, L173 (2002).

[51] N. Miyauchi, H. Hidaka, T. Chigai, A. Nagaoka, N. Watanabe et al., "Formation of hydrogen peroxide and water from the reaction of cold hydrogen atoms with solid oxygen at 10 K," *Chem. Phys. Lett.*, **456**, 27–30 (2008).

[52] E. Matar, E. Congiu, F. Dulieu, A. Momeni, and J. L. Lemaire, "Mobility of D atoms on porous amorphous water ice surfaces under interstellar conditions," *Astron. Astrophys.*, **492**, L17–L20 (2008).

[53] U. Raut and R. A. Baragiola, "Solid-state co oxidation by atomic o: a route to solid co2 synthesis in dense molecular clouds," *Astrophys. J. Lett.*, **737**, L14 (2011).

[54] J. Kalvāns and I. Shmeld, "Subsurface chemistry of mantles of interstellar dust grains in dark molecular cores," *Astron. Astrophys.*, **521**, A37 (2010).

[55] Q. Chang and E. Herbst, "A Unified Microscopic-Macroscopic Monte Carlo Simulation of Gas-grain Chemistry in Cold Dense Interstellar Clouds," *Astrophys. J.*, **759**, 147 (2012).

[56] R. T. Garrod, "A Three-phase Chemical Model of Hot Cores: The Formation of Glycine," *Astrophys. J.*, **765**, 60 (2013).

[57] W. Grundy, L. Young, and E. Young, "Discovery of CO2 ice and leading-trailing spectral asymmetry on the Uranian satellite Ariel," *Icarus*, **162**, 222–229 (2003).

[58] B. Buratti, D. Cruikshank, R. Brown, R. Clark, J. Bauer et al., "Cassini visual and infrared mapping spectrometer observations of Iapetus: Detection of CO2," *Astrophys. J.*, **622**, L149–L152 (2005).

[59] R. T. Garrod, S. L. W. Weaver, and E. Herbst, "Complex chemistry in star-forming regions: An expanded gas-grain warm-up chemical model," *Astrophys. J.*, **682**, 283–302 (2008).

[60] J. R. Brucato, G. A. Baratta, and G. Strazzulla, "An infrared study of pure and ion irradiated frozen formamide," *Astron. Astrophys.*, **455**, 395–399 (2006).

[61] S. E. Bisschop, G. W. Fuchs, A. C. A. Boogert, E. F. van Dishoeck, and H. Linnartz, "Infrared spectroscopy of HCOOH in interstellar ice analogues," *Astron. Astrophys.*, **470**, 749–759 (2007).

[62] K. I. Öberg, H. J. Fraser, A. C. A. Boogert, S. E. Bisschop, G. W. Fuchs et al., "Effects of CO2 on H2O band profiles and band strengths in mixed H2O : CO2 ices," *Astron. Astrophys.*, **462**, 1187–1198 (2007).

[63] K. I. Öberg, A. C. A. Boogert, K. M. Pontoppidan, S. van den Broek, E. F. van Dishoeck et al., "The Spitzer Ice Legacy: Ice Evolution from Cores to Protostars," *Astrophys. J.*, **740**, 109 (2011).

[64] M. Bernstein, D. Cruikshank, and S. Sandford, "Near-infrared laboratory spectra of solid H2O/CO2 and CH3OH/CO2 ice mixtures," *Icarus*, **179**, 527–534 (2005).

[65] O. Gálvez, I. K. Ortega, B. Maté, M. A. Moreno, B. Martín-Llorente et al., "A study of the interaction of CO{2} with water ice," *Astron. Astrophys.*, **472**, 691–698 (2007).

[66] B. Maté, O. Galvez, B. Martin-Llorente, M. A. Moreno, V. J. Herrero et al., "Ices of CO2/H2O mixtures. Reflection-absorption IR spectroscopy and theoretical calculations," *J. Phys. Chem. A*, **112**, 457–465 (2008).

[67] O. Galvez, B. Maté, V. J. Herrero, and R. Escribano, "Trapping and adsorption of CO2 in amorphous ice: A FTIR study," *Icarus*, **197**, 599–605 (2008).

[68] K. I. Öberg, E. C. Fayolle, H. M. Cuppen, E. F. van Dishoeck, and H. Linnartz, "Quantification of segregation dynamics in ice mixtures," *Astron. Astrophys.*, **505**, 183–194 (2009).

[69] G. Profeta and S. Scandolo, "Far-infrared spectrum of ice Ih: A first-principles study," *Phys. Rev. B*, **84**, 024103 (2011).

[70] J. E. Bertie, "Far-infrared Spectroscopy of the Ices," *Appl. Spec.*, **22**, 634–640 (1968).

[71] J. E. Bertie and S. M. Jacobs, "Far-infrared absorption by ices Ih and Ic at 4.3 [degree]K and the powder diffraction pattern of ice Ic," *J. Chem. Phys.*, **67**, 2445–2448 (1977).

[72] M. Moore and R. Hudson, "Far-infrared spectra of cosmic-type pure and mixed ices," *Astron. Astrophys. Supp. Ser.*, **103**, 45–56 (1994).

[73] M. Moore and R. Hudson, "Far-infrared spectral studies of phase-changes in water ice induced by proton irradiation," *Astrophys. J.*, **401**, 353–360 (1992).

[74] M. Moore and R. Hudson, "Far-ir spectral changes accompanying proton irradiation of solids of astrochemical interest," *Rad. Phys. Chem*, **45**, 779–789 (1995).

[75] N. Plattner, M. W. Lee, and M. Meuwly, "Structural and spectroscopic characterization of mixed planetary ices," *Faraday Discuss.*, **147**, 217–230 (2010).

[76] M. W. Lee, N. Plattner, and M. Meuwly, "Structure, spectroscopy and dynamics of layered H2O and CO2 ices," *Phys. Chem. Chem. Phys.*, **14**, 15464–15474 (2012).

[77] J. D. Green, I. Neal J. Evans, J. K. Jrgensen, G. J. Herczeg, L. E. Kristensen et al., "Embedded Protostars in the Dust, Ice, and Gas In Time (DIGIT) Herschel Key Program: Continuum SEDs, and an Inventory of Characteristic Far-infrared Lines from PACS Spectroscopy," *Astrophys. J.*, **770**, 123 (2013).

[78] R. Simon, N. Schneider, J. Stutzki, R. Guesten, U. U. Graf et al., "SOFIA observations of S106: dynamics of the warm gas," *Astron. Astrophys.*, **542**, L12 (2012).

[79] C. Qi, K. I. Öberg, D. J. Wilner, P. DAlessio, E. Bergin et al., "Imaging of the CO Snow Line in a Solar Nebula Analog," *Science*, **341**, 630–632 (2013).

[80] P. A. Gerakines, W. A. Schutte, J. M. Greenberg, and E. F. van Dishoeck, "The infrared band strengths of H_2_O, CO and CO_2_ in laboratory simulations of astrophysical ice mixtures." *Astron. Astrophys.*, **296**, 810 (1995).

[81] M. S. Westley, G. A. Baratta, and R. A. Baragiola, "Density and index of refraction of water ice films vapor deposited at low temperatures," *J. Chem. Phys.*, **108**, 3321–3326 (1998).

[82] M. Satorre, M. Domingo, C. Millan, R. Luna, R. Vilaplana et al., "Density of CH4, N2 and CO2 ices at different temperatures of deposition," *Planet. and Space Sci.*, **56**, 1748 – 1752 (2008).

[83] L. J. Karssemeijer, S. Ioppolo, M. C. van Hemert, A. van der Avoird, M. A. Allodi et al., "Dynamics of CO in Amorphous Water-ice Environments," *Astrophys. J.*, **781**, 16 (2014).

[84] Bossa, J. B., Isokoski, K., de Valois, M. S., and Linnartz, H., "Thermal collapse of porous interstellar ice," *Astron. Astrophys.*, **545**, A82 (2012).

[85] S. Krishnamurthy, R. Bansil, and J. Wiafe-Akenten, "Low-frequency Raman spectrum of supercooled water," *J. Chem. Phys*, **79**, 5863–5870 (1983).

[86] J. E. Bertie and E. Whalley, "Optical Spectra of Orientationally Disordered Crystals. II. Infrared Spectrum of Ice Ih and Ice Ic from 360 to 50 cm^{-1}," *J. Chem. Phys*, **46**, 1271–1284 (1967).

[87] D. D. Klug, J. S. Tse, and E. Whalley, "The longitudinal-optic–tranverse-optic mode splitting in ice Ih," *J. Chem. Phys*, **95**, 7011–7012 (1991).

[88] D. M. Hudgins, S. A. Sandford, L. J. Allamandola, and A. G. G. M. Tielens, "Mid- and far-infrared spectroscopy of ices - Optical constants and integrated absorbances," *Astrophys. J. Supp. Ser.*, **86**, 713–870 (1993).

[89] P. Jenniskens and D. F. Blake, "Crystallization of Amorphous Water Ice in the Solar System," *Astrophys. J.*, **473**, 1104 (1996).

[90] S. Ioppolo, G. Fedoseev, T. Lamberts, C. Romanzin, and H. Linnartz, "SURFRESIDE^2: An ultrahigh vacuum system for the investigation of surface reaction routes of interstellar interest," *Rev. of Sci. Inst.*, **84**, 073112 (2013).

[91] E. C. Fayolle, K. I. Öberg, H. M. Cuppen, R. Visser, and H. Linnartz, "Laboratory H_2O:CO_2 ice desorption data: entrapment dependencies and its parameterization with an extended three-phase model," *Astron. Astrophys.*, **529**, A74 (2011).

[92] W. Demtröder, *Laser Spectroscopy, 4th Ed.*, Springer (2008).

[93] T. S. Rose, M. J. Rosker, and A. H. Zewail, "Femtosecond realtime observation of wave packet oscillations (resonance) in dissociation reactions," *J. Chem. Phys.*, **88**, 6672–6673 (1988).

[94] P. Hamm and M. Zanni, *Concepts and Methods of 2D Infrared Spectroscopy*, Cambridge University Press (2011).

[95] I. R. Kleckner and M. P. Foster, "An introduction to NMR-based approaches for measuring protein dynamics," *Biochimica et Biophysica Acta (BBA) - Proteins and Proteomics*, **1814**, 942 – 968 (2011).

[96] W. D. Rice, J. Kono, S. Zybell, S. Winnerl, J. Bhattacharyya et al., "Observation of Forbidden Exciton Transitions Mediated by Coulomb Interactions in Photoexcited Semiconductor Quantum Wells," *Phys. Rev. Lett.*, **110**, 137404 (2013), doi:10.1103/PhysRevLett.110.137404.

[97] B. Zaks, R. B. Liu, and M. S. Sherwin, "Experimental observation of electron-hole recollisions," *Nature*, **483**, 580–583 (2012).

[98] G. I. Groma, J. Hebling, I. Z. Kozma, G. Vr, J. Hauer et al., "Terahertz radiation from bacteriorhodopsin reveals correlated primary electron and proton transfer processes," *Proc. Nat. Acad. Sci. USA*, **105**, 6888–6893 (2008), doi:10.1073/pnas.0706336105.

[99] J. Savolainen, S. Ahmed, and P. Hamm, "Two-dimensional Raman-terahertz spectroscopy of water," *Proc. Nat. Acad. Sci. USA*, **110**, 20402–20407 (2013), doi:10.1073/pnas.1317459110.

[100] W. Kuehn, K. Reimann, M. Woerner, and T. Elsaesser, "Phase-resolved two-dimensional spectroscopy based on collinear n-wave mixing in the ultrafast time domain," *J. Chem. Phys.*, **130**, 164503 (2009).

[101] W. Kuehn, K. Reimann, M. Woerner, T. Elsaesser, and R. Hey, "Two-Dimensional Terahertz Correlation Spectra of Electronic Excitations in Semiconductor Quantum Wells," *J. Phys. Chem. B*, **115**, 5448–5455 (2011).

[102] M. Woerner, W. Kuehn, P. Bowlan, K. Reimann, and T. Elsaesser, "Ultrafast two-dimensional terahertz spectroscopy of elementary excitations in solids," *New J. Phys.*, **15**, 025039 (2013).

[103] M. Cho, M. Du, N. F. Scherer, G. R. Fleming, and S. Mukamel, "Off resonant transient birefringence in liquids," *J. Chem. Phys.*, **99**, 2410–2428 (1993).

[104] R. Righini, "Ultrafast Optical Kerr Effect in Liquids and Solids," *Science*, **262**, 1386–1390 (1993).

[105] N. T. Hunt, A. A. Jaye, and S. R. Meech, "Ultrafast dynamics in complex fluids observed through the ultrafast optically-heterodyne-detected optical-Kerr-effect (OHD-OKE)," *Phys. Chem. Chem. Phys.*, **9**, 2167–2180 (2007).

[106] M. C. Hoffmann, N. C. Brandt, H. Y. Hwang, K.-L. Yeh, and K. A. Nelson, "Terahertz Kerr effect," *App. Phys. Lett.*, **95**, 231105 (2009).

[107] S. Ioppolo, B. A. McGuire, M. A. Allodi, and G. A. Blake, "THz and mid-IR spectroscopy of interstellar ice analogs: methyl and carboxylic acid groups," *Faraday Discuss.*, **168**, 461–484 (2014).

[108] Q. Wu and X.-C. Zhang, "Free-space electro-optic sampling of terahertz beams," *Appl. Phys. Lett.*, **67**, 3523–3525 (1995).

[109] Q. Zhong and J. T. Fourkas, "Optical Kerr Effect Spectroscopy of Simple Liquids," *J. Phys. Chem. B*, **112**, 15529–15539 (2008).

[110] B. J. Berne and R. Pectora, *Dynamic Light Scattering*, John Wiley & Sons (1976).

[111] T. Johnson, T. Masiello, and S. Sharpe, "The quantitative infrared and NIR spectrum of CH2I2 vapor: vibrational assignments and potential for atmospheric monitoring," *Atmos. Chem. Phys*, **6**, 2581–2591 (2006).

[112] A. Tokmakoff, M. J. Lang, D. S. Larsen, G. R. Fleming, V. Chernyak et al., "Two-Dimensional Raman Spectroscopy of Vibrational Interactions in Liquids," *Phys. Rev. Lett.*, **79**, 2702–2705 (1997).

[113] Y. Minami, Y. Hayashi, J. Takeda, and I. Katayama, "Single-shot measurement of a terahertz electric-field waveform using a reflective echelon mirror," *App. Phys. Lett.*, **103**, 051103 (2013).

[114] E. Harel, A. F. Fidler, and G. S. Engel, "Real-time mapping of electronic structure with single-shot two-dimensional electronic spectroscopy," *Proc. Nat. Acad. Sci. USA*, **107**, 16444–16447 (2010).

[115] P. D. Dahlberg, A. F. Fidler, J. R. Caram, P. D. Long, and G. S. Engel, "Energy Transfer Observed in Live Cells Using Two-Dimensional Electronic Spectroscopy," *J. Phys. Chem. Lett.*, **4**, 3636–3640 (2013).

[116] S. Ebbinghaus, S. J. Kim, M. Heyden, X. Yu, U. Heugen et al., "An extended dynamical hydration shell around proteins," *Proc. Natl. Acad. Sci. USA*, **104**, 20749–20752 (2007).

[117] S. Ebbinghaus, S. J. Kim, M. Heyden, X. Yu, M. Gruebele et al., "Protein Sequence- and pH-Dependent Hydration Probed by Terahertz Spectroscopy," *J. Am. Chem. Soc.*, **130**, 2374–2375 (2008).

[118] M. Heyden, J. Sun, S. Funkner, G. Mathias, H. Forbert et al., "Dissecting the THz spectrum of liquid water from first principles via correlations in time and space," *Proc. Natl. Acad. Sci. USA*, **107**, 12068–12073 (2010).

[119] M. Heyden and M. Havenith, "Combining THz spectroscopy and MD simulations to study protein-hydration coupling," *Methods*, **52**, 74 – 83 (2010).

[120] K. Meister, S. Ebbinghaus, Y. Xu, J. G. Duman, A. DeVries et al., "Long-range protein-water dynamics in hyperactive insect antifreeze proteins," *Proc. Natl. Acad. Sci. USA*, **110**, 1617–1622 (2013).

Appendix A

Computer Code Used for Data Analysis

The following chapter contains a sample of the various code used to process the linear THz and HD-TKE data. Presented here are the most recent versions, and older versions archived on the Blake group servers Calvin & Hobbes might be necessary to process older linear THz data. All code is written in MATLAB.

The most generally applicable code is the custom asymmetric Hann (or cosine) window function. This will be useful for most THz data processing in the lab and even, potentially (according to Brandon Carroll) for processing CP-FTMW data.

```
function output = ArbitraryCosineWindowTHz(filedata,dt,position)
%%Edit Histroy
%20 Apr 2015 - MAA - Set arbitrary position. Position input is in ps.
data=filedata;
%time=filedata(:,2);
peak=round(position/dt);

l=length(data);
%maxdata=max(abs(data));
%position=find(abs(data)==maxdata,1,'first');

%%Defining an asymetric Hann window

for i=0:peak-1
    output(i+1)=0.5*(1-cos(2*pi*i/(2*(peak-1))));
end

for i=peak:l-1
    output(i+1)=0.5*(1-cos((2*pi*i/(2*(l-peak)))-((2*pi*(l-1))/(2*(l-peak)))));
    %output(i+1)=0.5*(1-cos((2*pi*i/(2*(l-position)))-((2*pi*(l-2))/(2*(l-position)))));

    %Note:Getting the phase shift right was the tricky part of getting the asymetric window to wo
end
%output(l)=output(l-1); %not sure why this code was here but it was
%stopping my windowing funct from going to zero. MAA 4/2/14

output=output';
end
```

Next, we have the code that processes the linear THz data. The code reads in a scan into a matrix, cuts the data to fix the delay-line-start timing jitter, and finally outputs an average of the scans read in.

```
function output=Average_Data_v5(stringbase,numavg_begin,numavg_end)
%% Function written by Marco A. Allodi
%  Latest Version updated 7 Mar 2015
%% Function inputs%%%%%%%%%
%  stringbase is the file name as a matlab string without the number attached,
%   ie. 'sample_scan_'
%
%  numavg_begin is the file number where the function should start,
%  and numavg_end is the file where it should stop.
%
%   when numavg_begin is set to 0, the function will average every spectrum of
%   that name in the folder.
%% Update Log
%24 Feb 2015 - Changes allow someone to specify a start and stop file number
% 4 Mar 2015 - Saves output as a two-column ascii file
% 6 Mar 2015 - ***MAJOR UPDATE***
%                 Code now computes the standard deviation at each point.
%                 and saves that outupt to the .txt file output
% 7 Mar 2015 - Computes average from dataset matrix at end of program
%                 instead of during each loop interation
%%%
%% Begin Code

%% Parse the file header to get the points per ps and the time window.
headerfile=strcat(stringbase,num2str(1));
fid=fopen(headerfile,'r');
parse=textscan(fid,'%11s %8f %10s %3f');%set the numbers like %11s based on the size of the strin


if fid > 0
    exist=1; %set while-loop condition variable
end
```

```
%parse is a cell with four columns of data. the first value in the
%ptsperps column and time_window column are the numbers we need.
%I'm not sure what else textscan gives us, but we can just grab the first value.
ptsperps=parse{1,2};ptsperps=ptsperps(1);
time_window=parse{1,4};time_window=time_window(1);
fclose(fid);
time_window=time_window-0.25;

%number of data points in a scan in our time window
points=round(time_window*ptsperps);

%number of scans to be averaged
scans=numavg_end-numavg_begin+1;

%initilizing matricies
%avg=zeros([1,points]);
cut_data=zeros([1,points]);
dataset=zeros([scans,points]);

%initialize inputs for the first iteration of the while loop
k=1;
stringend=num2str(k);
filetoload=strcat(stringbase,stringend);

%% Begin loops which will bring in the data.

%This condition will average all the files in a folder without specifying
%a number of averages.
if numavg_begin==0
    while exist ~=0;
    %This loop takes runs until there are no longer any scans in a folder to average.
```

```
    file=dlmread(filetoload,'\t',1,0); %pulls in a scan
    data=file(:,1); %THz data
    position=file(:,2); %delay position data
        %The number for steps by which we overshoot the start position
        %varies based on delayline speed and can be found by
        %looking at a plot of the data in the position column

     %Find the point that corresponds to the start of the THz scan.
     [~, index]=min(abs(position-18));

    %cut the data set to only align the start positions. This also ensures
    %that we only include the data in the time window we desire in the
    %scans.
    cut_data(1:points)=data(index:(index+points-1));
    avg=avg+cut_data;

    k=k+1
    stringend=num2str(k);
    filetoload=strcat(stringbase,stringend);
    filecheck=fopen(filetoload,'r');
        if filecheck > 0
            exist=1;
        else
            exist=0;
        end
    end
%this loop pulls all the individual scans into memory.
else
    for i=numavg_begin:numavg_end

    stringend=num2str(i);
    filetoload=strcat(stringbase,stringend);
```

```
    file=dlmread(filetoload,'\t',1,0); %pulls in a scan
    data=file(:,1); %THz data
    position=file(:,2); %delay position data

    %The number for steps by which we overshoot the start position
    %varies based on delayline speed and can be found by looking
    %at a plot of the data in the position column
    %Find the point that corresponds to the start of the THz scan.
    [~, index]=min(abs(position-18));

    %code added by Xander to replace the for loop. Somehow this is faster
    %in Matlab than building a matrix with a for loop.
    cut_data(1:points)=data(index:(index+points-1));
    dataset(k,:)=cut_data;
    k=((i+1)-numavg_begin)+1
    end
end
%% Finish Processing Data and Output Data.
l=length(cut_data);
time=linspace(0,1,l)*time_window;

%Calculating Average and Standard Deviation
avg=mean(dataset);
avg=fliplr(avg);%flips the timing axis to the standard
% avg=moving_average(avg,1);%boxcars the data, 1 pt on either side
S=std(dataset);%Takes the standard deviation of each point in the dataset

%Defining output variable
output(:,1)=time;
output(:,2)=avg;
output(:,3)=S;
```

```
%% Saving double column ascii x-y file
strsuffix2='.txt';
savename=strcat(stringbase,strsuffix2);
save (savename,'output', '-ascii', '-double', '-tabs')

fclose all;
end
```

After processing both a background and sample scan, the following code can be used to Fourier transform and background subtract the data by taking the ratio of sample and reference.

```
function output = FreqRatioPlot(data,background)
%% Function by Marco A. Allodi
%Updated 16 Feb 2015
%Data should be in two-column format. Column 1 = x; Column 2 = y.

%% Setting the length of the FFT
datatofft=data(:,2); %the data to be ffted
l=length(datatofft); %length of the data
nfft=2^nextpow2(l*10);%appropriate length of the fft, with zero-padding
%nfft=2^nextpow2(l);%appropriate length of the fft, no extra zero-padding

%%%%%%%%%%%%%%%%%%
%% Setting the windowing function
%%%%%%%%%%%%%%%%%%
%Winfunct=TriangleWindowTHz(datatofft);
Winfunct_1=CosineWindowTHz(datatofft);

%% Data processing with windowing functions
datatofft=detrend(datatofft);
datatofft=Winfunct_1.*datatofft;

%% Taking the FFT of the data
fftdata=fft(datatofft,nfft)/l; %ffts the data filling the extra points with 0s
timedata=data(:,1); %we'll use the time data to generate the frequency axis
timedifference=timedata(4)-timedata(3); %the time spacing is in picoseconds
Fs=round(1/timedifference); %the number of points per ps effectively a sampling frequency
f= Fs/2*linspace(0,1,nfft/2); %creates the frequncy axis data

%% Setting up background FFT
bkgtofft=background(:,2); %background data to FFT
bkgtofft=detrend(bkgtofft);
Winfunct_2=CosineWindowTHz(bkgtofft);
```

```
bkgtofft=Winfunct_2.*bkgtofft;



fft_bkg=fft(bkgtofft,nfft)/l; %taking background FFT with zeropadding

%This was for transmission
%RatioSpec=fftdata./fft_bkg;

fft_bkg

RatioSpec=fft_bkg./fftdata;
%Absorbance=log10(RatioSpec); % Calculating absorbance

figure(1); plot(f, abs(RatioSpec(1:nfft/2))) %Plots absorbance 1 sided data
     % axis([0 5 -1.5 2.5])
     xlabel('Frequency (THz)')
     ylabel('Absorbance')
     drawnow;

%can enable to show plot with windowing function
figure(2);plot(timedata,datatofft);hold on;plot(timedata,Winfunct_1,'k')
   drawnow;

%% Output
output(:,1)=f;
output(:,2)=abs(RatioSpec(1:nfft/2));

end
```

If one desires to only look at the FFT of the data then the following code can be used.

```
function output = Log3FFT(data)
%data input should be in two column format
%the first column is the time axis
%the second column is the THz data

timedata=data(:,1); %we'll use the time data to generate the frequency axis
timedifference=timedata(4)-timedata(3); %the time spacing is in picoseconds
Fs=round(1/timedifference); %the number of points per ps effectively a sampling frequency

datatofft=data(:,2); %the data to be ffted
l=length(datatofft); %length of the data
exponent=nextpow2(10*l); %zero-padding
nfft=2^exponent;%appropriate length of the fft

%Apodizing the data
%Winfunct=window(@tukeywin,l,0.5);
%Winfunct=TriangleWindowTHz(datatofft);
Winfunct=CosineWindowTHz(datatofft);
datatofft=detrend(datatofft);
datatofft=Winfunct.*datatofft;

%fftdata=fft(datatofft,nfft);
fftdata=fft(datatofft,nfft)/l; %ffts the data filling the extra points with 0s

f= Fs/2*linspace(0,1,nfft/2); %creates the frequncy axis data
difference=f(4)-f(3)

figure(1); plot(f, log10(2*abs(fftdata(1:nfft/2)))) %Plots log of 1 sided data
     % axis([0 5 -1.5 2.5])
     xlabel('Frequency (THz)')
     ylabel('Log Normalized FFT Intensity')
```

```
     drawnow;


figure(2);plot(data(:,1),datatofft);hold on;plot(data(:,1),Winfunct,'k')
   drawnow;


output(:,1)=f;
output(:,2)=log10(2*abs(fftdata(1:nfft/2)));


end
```

The requirements for processing TKE data are slightly different. We use the following code to read in and average the data.

```
function output=Average_Data_v6(stringbase,numavg_begin,numavg_end,normalization)
%% Function written by Marco A. Allodi
%  Latest Version updated 13 Mar 2015
%% Function inputs %%%%%%%%%
%  -stringbase is the file name as a matlab string without the number attached,
%   ie. 'sample_scan_'
%
%  -numavg_begin is the file number where the function should start.
%  -numavg_end is the file where it should stop.
%    when numavg_begin is set to 0, the function will average every spectrum of
%    that name in the folder.
%  -normalization = 1 scales data so that the peak = 1 arbitrary unit,
%    adjust for negative DC offset, and places the peak at time = 0 ps.
%  -normalization = 0 leaves the data unchanged
%% Update Log %%%%%%%%%%%%
% 24 Feb 2015 - Changes allow someone to specify a start and stop file number
%  4 Mar 2015 - Saves output as a two-column ascii file
%  6 Mar 2015 - ***MAJOR UPDATE***
%                 Code now computes the standard deviation at each point.
%                 and saves that outupt to the .txt file output
%  7 Mar 2015 - Computes average from dataset matrix at end of program
%                 instead of during each loop interation
% 13 Mar 2015 - Updated to include the option to normalize data to 1 and set
%                 the signal peak = 0 ps in time.
% 13 Mar 2015 - Output in third column is now standar deviation of the mean
% 30 Mar 2015 - Shifted the time axis so that the peak appears at t=0
%%%%%%%%%%%%%%%%%%%%%%%%%%
%% Begin Code
%
%% Parse the file header to get the points per ps and the time window.
headerfile=strcat(stringbase,num2str(1));
fid=fopen(headerfile,'r');
```

```
parse=textscan(fid,'%11s %8f %10s %3f');%set the numbers like %11s based on the size of the strin

if fid > 0
    exist=1; %set while-loop condition variable
end

%parse is a cell with four columns of data. the first value in the ptsperps column and time_windo
%I'm not sure what else textscan gives us, but we can just grab the first value.
ptsperps=parse{1,2};ptsperps=ptsperps(1);
time_window=parse{1,4};time_window=time_window(1);
fclose(fid);
time_window=time_window-0.25;

%number of data points in a scan in our time window
points=round(time_window*ptsperps);

%number of scans to be averaged
scans=numavg_end-numavg_begin+1;

%initilizing matricies
%avg=zeros([1,points]);
cut_data=zeros([1,points]);
dataset=zeros([scans,points]);

%initialize inputs for the first iteration of the while loop
k=1;
stringend=num2str(k);
filetoload=strcat(stringbase,stringend);

%% Begin loops which will bring in the data.

%This condition will average all the files in a folder without specifying
```

```
%a number of averages.
if numavg_begin==0
    while exist ~=0; %This loop takes runs until there are no longer any scans in a folder to ave

    file=dlmread(filetoload,'\t',1,0); %pulls in a scan
    data=file(:,1); %THz data
    position=file(:,2); %delay position data
        %The number for steps by which we overshoot the start position
        %varies based on delayline speed and can be found by looking at a plot of the data in the

     [~, index]=min(abs(position-18));  %Find the point that corresponds to the start of the THz

    %cut the data set to only align the start positions. This also ensures
    %that we only include the data in the time window we desire in the
    %scans.
    cut_data(1:points)=data(index:(index+points-1));
    avg=avg+cut_data;

    k=k+1
    stringend=num2str(k);
    filetoload=strcat(stringbase,stringend);
    filecheck=fopen(filetoload,'r');
        if filecheck > 0
            exist=1;
        else
            exist=0;
        end
    end
%this loop pulls all the individual scans into memory.
else
    for i=numavg_begin:numavg_end
```

```
        stringend=num2str(i);
        filetoload=strcat(stringbase,stringend);
        file=dlmread(filetoload,'\t',1,0); %pulls in a scan
        data=file(:,1); %THz data
        position=file(:,2); %delay position data

        %The number for steps by which we overshoot the start position
        %varies based on delayline speed and can be found by looking at a plot of the data in the
        [~, index]=min(abs(position-18)); %Find the point that corresponds to the start of the TH
        cut_data(1:points)=data(index:(index+points-1)); %Define new data after cutting initial a
        dataset(k,:)=cut_data; %each average becomes a row in a matrix
        k=((i+1)-numavg_begin)+1 % increment count
    end
end
%% Finish Processing Data and Output Data.
l=length(cut_data);
time=linspace(0,1,l)*time_window;

%Calculating Average and Standard Deviation
avg=mean(dataset);
avg=fliplr(avg);%flips the timing axis to the standard
% avg=moving_average(avg,1);%boxcars the data, 1 pt on either side
S=std(dataset);%Takes the standard deviation of each point in the dataset
Sm=S/sqrt(scans);%Standard Deviation of the mean.

if normalization == 1
    %Defining output variable
    i1 = find(time<1.0);
    i1 = i1(end);
    offset = mean(avg(1:i1));
    avg1 = avg-offset;
    avg1=-1*avg1;
```

```
    [m,i] = max(avg1);
    output(:,1)=time-time(i);
    output(:,2)=avg1/m;
    output(:,3)=Sm;
else
    %Defining output variable
    [~,i] = max(avg);
    output(:,1)=time-time(i);
    output(:,2)=avg;
    output(:,3)=Sm;
end
%% Saving double column ascii x-y file
strsuffix2='.txt';
savename=strcat(stringbase,strsuffix2);
save (savename,'output', '-ascii', '-double', '-tabs')

fclose all;
end
```

Finally, the TKE can be Fourier Transformed with this code.

```
function output = TKE_FFT(data)
%% Function written by Marco A. Allodi
%  Update History
%  updated 2 Apr 2015
%  20 Apr 2015 - Added arbitrarly defined asymmetric Hann window to provide
%                adequate windowing for the FFT analysys
%
%  This function calculates the complex FFT of the TKE data after the peak.
%  The output is the imagninary component of the complex FFT
%% Function inputs %%%%%%%%%
%data input should be in two column format
%the first column is the time axis
%the second column is the THz data

timedata=data(:,1); %we'll use the time data to generate the frequency axis
timedifference=timedata(4)-timedata(3); %the time spacing is in picoseconds
Fs=round(1/timedifference); %the number of points per ps effectively a sampling frequency

%% Cutting the data
datatofft1=data(:,2); %the data to be ffted
l=length(datatofft1); %length of the data
[~,m]=max(datatofft1);
n=l-m;
datatofft(1:n)=datatofft1(m:l-1);
time2(1:n)=timedata(m:l-1);
exponent=nextpow2(10*n); %zero-padding
% exponent=nextpow2(10*n); %zero-padding
nfft=2^(exponent);%appropriate length of the fft

%% Apodizing the data
Winfunct=ArbitraryCosineWindowTHz(datatofft,timedifference,1);
Winfunct=Winfunct';
```

```
datatofft=Winfunct.*datatofft;

%% Taking the FFT
%fftdata=fft(datatofft,nfft);
fftdata=fft(datatofft,nfft)/n; %ffts the data filling the extra points with 0s

f= Fs/2*linspace(0,1,nfft/2); %creates the frequncy axis data
difference=f(4)-f(3)

% pt=80;
pt=1;
datareal=real(fftdata(1:nfft/2));
datareal=moving_average(datareal,pt);

dataimag=imag(fftdata(1:nfft/2));
dataimag=moving_average(dataimag,pt);%boxcars the data, 1 pt on either side

figure(1); plot(f, -1*dataimag) %Plots imaginary component of data
     % axis([0 5 -1.5 2.5])
     xlabel('Frequency (THz)')
     ylabel('Imaginary FFT Intensity')
     drawnow;

figure(2); plot(f, datareal) %Plots imaginary component of data
     % axis([0 5 -1.5 2.5])
     xlabel('Frequency (THz)')
     ylabel('Real FFT Intensity')
     drawnow;

figure(3);plot(f, 2*abs(fftdata(1:nfft/2))) %Plots imaginary component of data
     % axis([0 5 -1.5 2.5])
     xlabel('Frequency (THz)')
```

```
     ylabel('Absolute Value FFT Intensity')
     drawnow;

 figure(4);plot(datatofft(1:n));hold on; plot(Winfunct);
      drawnow;

output(:,1)=f;
%output(:,2)=abs(fftdata(1:nfft/2));
output(:,2)=-1*dataimag;

% output(:,1)=time2;
% output(:,2)=datatofft;



end
```